

Научном већу Института за физику Београд

Београд, 21. новембар 2019. године

Предмет:

Молба за покретање поступка за реизбор у звање научни сарадник

Обзиром да испуњавам критеријуме прописане од стране Министарства просвете, науке и технолошког развоја за стицање звања научни сарадник, молим Научно веће Института за физику Београд да покрене поступак за мој реизбор у наведено звање.

У прилогу достављам:

1. Мишљење руководиоца пројекта са предлогом чланова комисије за избор у звање
2. Стручну биографију
3. Преглед научне активности
4. Елементе за квалитативну и квантитативну оцену научног доприноса са доказима
5. Списак објављених научних радова и њихове копије
6. Податке о цитираности
7. Уверење о претходном избору

Са поштовањем,
др Јулија Шћепановић

ИНСТИТУТ ЗА ФИЗИКУ

ПРИМЉЕНО: 21. 11. 2019			
Рад.јед.	б р о ј	Арх.шифра	Прилог
0901	1790/1		

Научном већу Института за физику у Београду

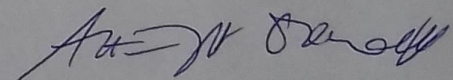
Предмет: Мишљење руководиоца пројекта о reizбору др Јулије Шћепановић у звање научни сарадник

Др Јулија Шћепановић је запослена у Лабораторији за статистичку физику комплексних система, у оквиру Националног центра изузетних вредности за изучавање комплексних система Института за физику у Београду и ангажована је на пројекту основних истраживања Министарства просвете, науке и технолошког развоја Републике Србије ОН171017, под називом "Моделирање и нумеричке симулације сложених вишечестичних физичких система". На поменутом пројекту се бави нумеричким и експерименталним проучавањем процеса у разним неравнотежним системима, као што су порозни материјали, стакласти системи и грануларни материјали. С обзиром да испуњава све предвиђене услове у складу са Правилником о поступку, начину вредновања и квантитативном исказивању научноистраживачких резултата истраживача МПНТР, сагласан сам са покретањем поступка за reizбор др Јулије Шћепановић у звање научни сарадник.

За састав комисије за reizбор др Јулије Шћепановић у звање научни сарадник предлажем:

- (1) др Слободан Врховац, научни саветник, Институт за физику у Београду,
- (2) др Душан Арсенић, научни саветник, Институт за физику у Београду,
- (3) проф. др Сунчица Елезовић-Хацић, редовни професор Физичког факултета Универзитета у Београду.

Руководилац пројекта



др Антун Балаж
научни саветник

Биографија др Јулије Шћепановић

Јулија Шћепановић (1980) рођена је у Београду где завршава основну и средњу школу (Трећу београдску гимназију). Основне академске студије на Математичком факултету Универзитета у Београду, смер Астрофизика завршава 2008. године са просечном оценом 8.27.

Академске 2009/2010. године уписује докторске студије на Физичком факултету Универзитета у Београду, смер Примењена и компјутерска физика које завршава 2014. године. Докторску дисертацију под називом *Релаксациона својства модела субдифузивног гаса на троуганој решетки* радила је у Лабораторији за примену рачунара у науци Института за физику под руководством др Слободана Врховца, научног саветника Института за физику у Београду.

У Институту за физику запослена је од 2011. године. Ангажована је на пројекту Министарства за просвету и науку “Моделирање и нумеричке симулације сложених вишечестичних система” ON171017. На поменутом пројекту бави се нумеричким и експерименталним проучавањем процеса у разним неравнотежним системима, као што су порозни материјали, стакласти системи и грануларни материјали. До избора у звање научног сарадника објавила је 2 рада категорије M21 и један рад категорије M22. Учесник је неколико међународних школа и конференција на којима је представила своја истраживања.

У звање научни сарадник изабрана је 25.3.2015. године. Од тог тренутка објавила је 4 рада категорије M21 и један рад категорије M23. На два рада је први аутор.

Преглед научне активности др Јулије Шћепановић

Јулија Шћепановић започела је свој истраживачки рад у Лабораторији за примену рачунара у науци Института за физику Београд 2008. године, где је запослена од 2011. године. Од 2015. године члан је Лабораторије за статистичку физику комплексних система.

Научне области којима се бавила обухватају проучавање транспортних својстава разуређених система, као што су порозни материјали, стакласти системи и грануларни материјали. Основни циљеви њеног рада били су боље разумевање феномена аномалне дифузије у системима као што су микро-порозни материјали и супер-охлађене течности. Осим тога, направила је искорак ка новој проблематици која је бави проучавањима неких комплексних система применом agent-based модела.

Преглед основних резултата научних истраживања Јулије Шћепановић биће презентован у виду резимеа радова које је објавила у међународним часописима.

- D. Stojiljković, J. R. Šćepanović, S. B. Vrhovac and N. M. Švrakić, "Structural properties of particle deposits at heterogeneous surfaces", *J. Stat. Mech.: Theory and Experiment*, **P06032**, (2015). (M21a)

Изучавани су процеси депозиције честица на хетерогеним супстратима. Метод случајне секвенцијалне адсорпције је коришћен за анализу депозиције сферних нано-честица на неуниформном планарном супстрату. Неуниформност површине је моделована њеним

препокривањем квадратним ћелијама фиксне оријентације. При томе се ћелије распоређују у чворовима квадратне решетке. У моделу се претпоставља да се адсорпција сферне честице врши само уколико се њен центар налази унутар неке квадратне ћелије. Својства система у стању прекривености загушења је анализирана за квадратне ћелије различитих величина и иницијалних густина препокривања. Нумеричким симулацијама анализирана је кинетика процеса адсорпције и структура депозита у стању загушења. Структурна својства покривача су анализирана коришћењем радијалне дистрибуције $g(r)$ и дистрибуције Delaunay-ве слободне запремине $P(v)$. Променом величине ћелија и растојања између њих могуће је изучавати динамику процеса адсорпције на граници између депозиције на континуалном супстрату и депозиције на дискретном супстрату (решетки). Резултати показују да за ћелије чија је страница мања од $(\frac{1}{2})^{0.5}$ и које се налазе на довољно малом растојању, асимптотски прилаз система густини загушења је алгебарски, као у случају када је супстрат хомоген. Са повећањем растојања између ћелија пораст густине система ка густини загушења у току времена постаје све ближи експоненцијалној зависности. Другим речима, предложени модел дозвољава интерполацију кинетике депозиције између континуалног и дискретног супстрата, а тиме и изучавање механизма који доводе до промене асимптотског понашања покривености субстрата. Резултати сугеришу да порозност депозита може бити контролисана величином и обликом адсорбујућих (предепонованих) ћелија и анизотропијом њихове депозиције. Јулија Шћепановић учествовала је у анализи и интерпретацији добијених резултата.

- J. R. Šćepanović, D. Stojiljković, Z. M. Jakšić, Lj. Budinski-Petković and S. B. Vrhovac, "Response properties in the generalized random sequential adsorption model on a triangular lattice", *Physica A: Statistical Mechanics and its Applications*, **451**, 213 - 226, (2016). (M21)

На моделу реверзибилне секвенцијалне адсорпције анализирани су могућности оптимизације процеса компактификације грануларних материјала променама интензитета екстерне побуде. Циљ истраживања је био истражити како промене вероватноће десорпције убрзавају, или успоравају пораст густине током процеса реверзибилне депозиције. Анализиран је утицај геометријских својстава депонованих објеката на одговор система на тренутну пертурбацију вероватноће десорпције (тј. на тренутно смањење интензитета побуде). Посебна пажња је посвећена симетријским својствима објеката у моделу, јер се она могу довести у везу са материјалним својствима грануларног материјала (нееластичност, дисипативност судара и коефицијент трења гранула). Показано је да се процес реверзибилне депозиције високо симетричних објеката знатно лошије оптимизује од депозиције објеката ниже симетрије уколико се вероватноћа десорпције скоковито мења. Разлог за то су меморијски ефекти који битно зависе од ротационе симетрије објеката. Анализом дво-временске корелационе функције густине показано је да су меморијски ефекти знатно више изражени код процеса депозиције објеката више симетрије. Овај резултат указује на то да је процес компактификације грубих и изразито нееластичних гранула знатно теже ефикасно оптимизовати временски

зависном побудом. Осим тога, анализом процеса реверзибилне депозиције бинарних смеша објеката разних ротационих симетрија показано је да динамички одговор система на наглу промену интензитета побуде контролише објекат ниже симетрије. Јулија Шћепановић је изградила модел, учествовала у прикупљању података, њиховој анализи, интерпретацији и писању рада.

- Z. M. Jakšić, M. Cvetković, J. R. Šćepanović, I. Lončarević, Lj. Budinski-Petković and S. B. Vrhovac, "The electrical resistance decay of a metallic granular packing", *Eur. Phys. J. B*, **90**, 108, (2017). (M23)

Развијен је експеримент којим је изучавана електрична проводност грануларног материјала у условима малих струја (10^{-3} А). Мерења су показала да је у описаном струјном режиму, отпорност грануларног материјала величина која се мења у току времена. Предмет истраживања је била ова веома спора релаксација проводности. Анализирани су узроци њеног настанка. Мерења су извршена на грануларним паковањима формираним у једној и две димензије. Мерења на планарним грануларним паковањима омогућавају успостављање везе између проводности и микроструктуралних својстава система. Такође је анализиран утицај ефективне гравитације на електричну проводност грануларног система. Мерења су показала да за пораст проводности статичког грануларног паковања нису одговорне структурне промене система. Постоје јаке експерименталне индикације да до пораста проводности долази искључиво због процеса који се локално дешавају на појединачним контактима између гранула.

Један од основних циљева била је изградња електро-механичког модела контакта који може репродуковати веома спору временску релаксацију проводности. Предложени модел контакта почива на субординацији стохастичких процеса. Претпоставља се да микроконтакти који постоје у области додира две грануле настају и нестају услед термално-механичких ефеката. Овај стохастички процес се спреже са другим процесом који дефинише трајање временских интервала измађу узастопних промена стања неког микроконтакта. Претпостављајући да се ови случајни временски интервали генеришу из функција расподеле које немају коначне моменте, субординацијом се добија резултатујући процес који је описан фракционим кинетичком једначином. Добијена једначина се може аналитички решити чиме се добија детаљан квантитативни опис временске релаксације проводности. Експериментално је показано је да се временска еволуција проводности може описати Mittag-Leffler функцијом, што је у сагласности са предложеним моделом. Јулија Шћепановић је учествовала у изградњи и реализацији експеримента, анализи резултата, као и у њиховој интерпретацији.

- Lj. Budinski-Petković, I. Lončarević, D. Dujak, A. Karač, J. R. Šćepanović, Z. M. Jakšić and S. B. Vrhovac, "Particles morphology effects in random sequential adsorption", *Phys. Rev. E*, **95**, 022114, (2017). (M21)

Анализирана је динамика процеса депозиције “нарастајућих” објеката разних облика на планарној триангуларној решетки. Објекти су генерисани као самонепресечајуће шетње на триангуларној решетки. При томе величина објеката је поступно увећавана “намотавањем” шетње на неколико различитих начина. На тај начин се добијају велике колекције објеката разних величина и симетрија (твз. “нарастајући” троуглови, ромбови и шестоуглови). Резултати показују да одлучујући утицај на динамику касне фазе депозиције има ред осе симетрије објекта. Нађено је да је прилазак граници загушења експоненцијалан за све облике и да се кинетика тог процеса успорава са опадањем реда симетрије објеката. Време релаксације σ је искључиво одређено редом симетрије објекта n_s и важи $\sigma \sim 6/n_s$ за троугаону решетку. За мале објекте густина загушења брзо опада са порастом величине објеката без обзира на облик. Али за довољно велике објекте промена облика далеко више утиче на величину границе загушења него промена величине. Вероватноћа за уметање новог објекта на решетку $P(n)$ се може описати производом степене и субекспоненцијалне функције у широком опсегу густина испод густине загушења. При томе, доведени су у везу параметара фита вероватноће $P(n)$ са дескрипторима облика којима су окарактерисани депоновани објекти. Јулија Шћепановић учествовала је у изградњи модела и реализацији веома захтевних нумеричких симулација, као и у анализи и интерпретацији добијених резултата.

- J. R. Šćepanović, A. Karač, Z. M. Jakšić, Lj. Budinski-Petković, and S. B. Vrhovac, "Group chase and escape in the presence of obstacles", *Physica A: Statistical Mechanics and its Applications*, **525**, 450 - 465, (2019). (M21)

Развијен је модел групног лова и бегства којим је анализирана динамика еволуције две врсте (ловаца и жртви) у окружењу које садржи препреке. Обе врсте могу утицати на своје кретање на основу "визуелне" перцепције унутар коначног опсега посматрања. У моделу су анализирана два алгоритма трагања за жртвама и избегавања ловаца. Monte Carlo симулације су извршене на квадратној решетки, при чему су препреке представљене објектима разних облика и величина. Показано је да временска еволуција броја жртви може бити описана субекспоненцијалном функцијом без обзира да ли су препреке присутне или не. Карактеристично време живота жртви је степена функција њихове почетне густине. Поређене су временске зависности броја жртви за разне опсеге перцепције којом располажу обе врсте. Јулија Шћепановић је иницирала ова истраживања, изградила нумеричке моделе и учествовала у писању рада.

Током септембра 2017. године била је учесник конференције YUCOMAT у Херцег Новом, Црна Гора, где је одржала предавање под називом *Particle morphology effects in random sequential adsorption*.

Током 2019. поново је учествовала на истој конференцији где је представила рад под називом *Group chase and escape in the presence of obstacles*.

Елементи за квалитативну оцену научног доприноса

1. Квалитет научних резултата

1.1 Значај научних резултата

Испитивање грануларних материјала је веома актуелна област физике током последње две и по деценије. Особине грануларних система могу се схватити анализом њихових микроструктуралних својстава, које се веома тешко могу добити у експериментима. Веома захтевне нумеричке симулације молекуларно-динамичког типа су један од путева ка остварењу истог циља. Међутим, често се прибегава изградњи нумеричких модела који имитирају овакве системе и могу дати значајан увид у њихово понашање. Кандидаткиња је на релативно једноставном моделу реверзибилне секвенцијалне адсорпције анализирали могућности оптимизације процеса компактификације грануларних материјала променама интензитета екстерне побуде. При томе је посебна пажња посвећена симетријским својствима објеката у моделу, јер се она могу довести у везу са материјалним својствима грануларног материјала (нееластичност, дисипативност судара и коефицијент трења гранула). Добијени резултати указују на то да је процес компактификације грубих и изразито нееластичних гранула знатно теже ефикасно оптимизовати временски зависном побудом од процеса у системима са слабо дисипативним гранулама.

Јулија Шћепановић је самостално направила искорак ка изучавању комплексних система који се могу описати agent-based моделима. Модели ловац-жртва су поново постали актуелни у последњих 20 година захваљујући развоју комјутерских техника. Развојем оригиналног модела она је указала на разне утицаје које хетерогености окружења (присуство препрека) могу да имају на временску еволуцију агената у случајевима групног лова.

1.2. Параметри квалитета часописа

- 1 рад у међународном часопису изузетних вредности Journal of Statistical Mechanics (IF = 2.404, SNIP = 0.728)
- 1 врхунски међународни часопис Physica A (IF = 2.500, SNIP = 1.214)
- 1 истакнути међународни часопис European Physical Journal B (IF = 1.368, SNIP = 0.635)
- 1 врхунски међународни часопис Physical Review E (IF = 2.380, SNIP = 1.005)
- 1 врхунски међународни часопис Physica A (IF = 2.500, SNIP = 0.214)

Укупан импак фактор износи 11.152.

1.3 Подаци о цитираност

Према званичној Scopus бази радови Јулије Шћепановић су укупно цитирани 10 пута без аутоцитата. Према овој бази Хиршов индекс кандидаткиње износи $H=2$.

1.4 Додатни библиометријски показатељи

Додатни библиометријски параметри су приказани у следећој табели:

	ИФ	М	СНИП
Укупно	11.152	37	4.796
Усредњено по чланку	2.231	7.4	0.959
Усредњено по аутору	2.064	6.852	0.888

2. Нормирање броја коауторских радова, патената и техничких решења

Два рада кандидаткиње имају више од 5 аутора, односно један М21 има 6, други М23 7 аутора, тако да они не иду са пуном тежином, па укупно М бодова кандидаткиње са нормирањем износи 34.81 бодова.

3. Учешће у пројектима, потпројектима и пројектним задацима

Кандидаткиња је учествовала на следећим пројектима:

- пројекат Министарства просвете, науке и технолошког развоја Републике Србије ON171017: Моделирање и нумеричке симулације сложених вишечестичних система.

4. Утицај научних резултата

Утицај научних резултата кандидаткиње се огледа у броју цитата који су наведени у тачки 1. овог прилога, као и у прилогу о цитираности и Елементима за квалитативну и квантитативну оцену научног доприноса. У тачки 1. је такође описан значај научних резултата.

5. Конкретан допринос кандидата у реализацији радова у научним центрима у земљи и иностранству

Кандидаткиња је све своје истраживачке активности реализовала у Институту за физику Београд. Кандидаткиња је дала битан допринос објављеним радовима. Њен допринос се огледа у овладавању нумеричком процедуром и изградњом модела, добијању, интерпретацији и презентацији нумеричких резултата, теоријском побољшању модела, писању радова и учествовању у експериментима.

Елементи за квантитативну оцену научног доприноса

Остварени М-бодови по категоријама публикација

Категорија	М-бодова по публикацији	Број публикација	Укупно М-бодова
M21a	10	1	10
M21	8	3	24
M23	3	1	3
M33	0.5	2	1

Поређење оствареног броја М-бодова са минималним условима потребним за реизбор у звање научног сарадника

	Потребно	Остварено
Укупно	16	38
M10+M20+M31+M32+M33+M41+M42	10	38
M11+M12+M21+M22+M23	6	37

Списак радова др Јулије Шћепановић

Радови међународном часопису изузетних вредности (M21a):

1. D. Stojiljković, J. R. Šćepanović, S. B. Vrhovac and N. M. Švrakić, "Structural properties of particle deposits at heterogeneous surfaces", *J. Stat. Mech.: Theory and Experiment*, **P06032**, (2015), (DOI: 10.1088/1742-5468/2015/06/P06032)

Радови у врхунским међународним часописима (M21):

1. J. R. Šćepanović, D. Stojiljković, Z. M. Jakšić, Lj. Budinski-Petković and S. B. Vrhovac, "Response properties in the generalized random sequential adsorption model on a triangular lattice", *Physica A: Statistical Mechanics and its Applications*, **451**, 213 - 226, (2016). (DOI: 10.1016/j.physa.2016.01.055)
2. Lj. Budinski-Petković, I. Lončarević, D. Dujak, A. Karač, J. R. Šćepanović, Z. M. Jakšić and S. B. Vrhovac, "Particles morphology effects in random sequential adsorption", *Phys. Rev. E*, **95**, 022114, (2017), (DOI: 10.1103/PhysRevE.95.022114)
3. J. R. Šćepanović, A. Karač, Z. M. Jakšić, Lj. Budinski-Petković, and S. B. Vrhovac, "Group chase and escape in the presence of obstacles", *Physica A: Statistical Mechanics and its Applications*, **525**, 450 - 465, (2019), (DOI: 10.1016/j.physa.2019.03.017)

Радови у истакнутим међународним часописима (M23):

1. Z. M. Jakšić, M. Cvetković, J. R. Šćepanović, I. Lončarević, Lj. Budinski-Petković and S. B. Vrhovac, "The electrical conductance growth of a metallic granular packing", *Eur. Phys. J. B*, **90**, 108, (2017). (<https://doi.org/10.1140/epjb/e2017-70597-6>)

Саопштења са међународних скупова штампана у изводу (M34):

1. Particle morphology effects in random sequential adsorption

Ljupka Budinski Petković, Ivana Lončarević, Dijana Dujak, Aleksandar Karac, Julija R Šćepanović, Zorica M Jakšić, Slobodan B Vrhovac, Faculty of Engineering, Trg D. Obradovica 6, Novi Sad, 21000 Serbia, Faculty of Metallurgy and Materials, University of Zenica, Zenica, Bosnia and Herzegovina, Polytechnic Faculty, University of Zenica, Zenica, Bosnia and Herzegovina, Scientific Computing Laboratory, Center for the Study of Complex Systems, Institute of Physics Belgrade, University of Belgrade, Pregrevica 118, Zemun 11080, Belgrade, Serbia

2. Group chase and escape in the presence of obstacle

Julija R. Šćepanović, Aleksandar Karač, Zorica M. Jakšić, Ljuba Budinski-Petković, Slobodan B. Vrhovac, Scientific Computing Laboratory, Center for the Study

of Complex Systems, Institute of Physics Belgrade, University of Belgrade, Belgrade,
Serbia

Web of Science



Search Tools Searches and alerts Search History Marked List

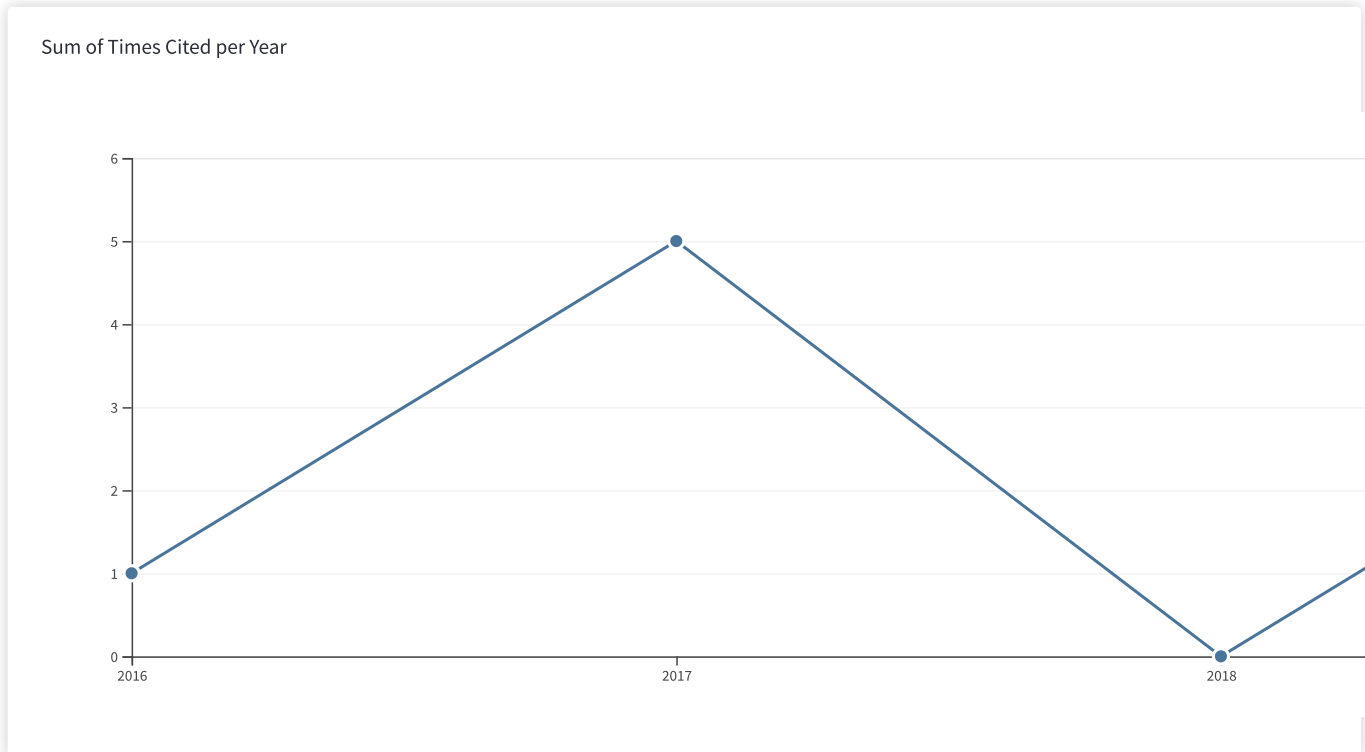
Citation report for 4 results from Web of Science Core Collection between 2015 and 2020 Go

You searched for: AUTHOR: (Scepanovic, J. R.) ...More

This report reflects citations to source items indexed within Web of Science Core Collection. Perform a Cited Reference Search to include citations to items not indexed within Web of Science Core Collection.

Export Data: Save to Excel File

<p>Total Publications </p> <p>4 Analyze</p> <p>2000 2019</p>	<p><i>h</i>-index </p> <p>2</p> <p>Average citations per item</p> <p>2.5</p>	<p>Sum of Times Cited </p> <p>10</p> <p>Without self citations</p> <p>9</p>	<p>Citing articles </p> <p>10 Analyze</p> <p>Without self citations</p> <p>9 Analyze</p>
---	--	---	--



Sort by: Times Cited Date More

1 of 1

How are these totals calculated?

2016	2017	2018	2019	2020	Total	Average Citations
------	------	------	------	------	-------	-------------------

Use the checkboxes to remove individual items from this Citation Report

	1	5	0	4	0	10	2.50
<input type="checkbox"/> or restrict to items published between <input type="text" value="2015"/> and <input type="text" value="2020"/> <input type="button" value="Go"/>							
<input type="checkbox"/> 1. Structural properties of particle deposits at heterogeneous surfaces By: Stojiljkovic, D.; Scepanovic, J. R.; Vrhovac, S. B.; et al. JOURNAL OF STATISTICAL MECHANICS-THEORY AND EXPERIMENT Article Number: P06032 Published: JUN 2015	1	3	0	1	0	5	1.00
<input type="checkbox"/> 2. Particle morphology effects in random sequential adsorption By: Budinski-Petkovic, Lj.; Loncarevic, I.; Dujak, D.; et al. PHYSICAL REVIEW E Volume: 95 Issue: 2 Article Number: 022114 Published: FEB 13 2017	0	1	0	2	0	3	1.00
<input type="checkbox"/> 3. Response properties in the adsorption-desorption model on a triangular lattice By: Scepanovic, J. R.; Stojiljkovic, D.; Jaksic, Z. M.; et al. PHYSICA A-STATISTICAL MECHANICS AND ITS APPLICATIONS Volume: 451 Pages: 213-226 Published: JUN 1 2016	0	1	0	1	0	2	0.50
<input type="checkbox"/> 4. Group chase and escape in the presence of obstacles By: Scepanovic, J. R.; Karac, A.; Jaksic, Z. M.; et al. PHYSICA A-STATISTICAL MECHANICS AND ITS APPLICATIONS Volume: 525 Pages: 450-465 Published: JUL 1 2019	0	0	0	0	0	0	0.00

 Select Page


Sort by: Times Cited Date More

◀ 1 of 1 ▶

4 records matched your query of the 14,160,350 in the data limits you selected.

Clarivate

Accelerating innovation

© 2019 Clarivate

[Copyright notice](#)

[Terms of use](#)

[Privacy statement](#)

[Cookie policy](#)

[Sign up for the Web of Science newsletter](#)

Follow us



Structural properties of particle deposits at heterogeneous surfaces

This content has been downloaded from IOPscience. Please scroll down to see the full text.

J. Stat. Mech. (2015) P06032

(<http://iopscience.iop.org/1742-5468/2015/6/P06032>)

View [the table of contents for this issue](#), or go to the [journal homepage](#) for more

Download details:

IP Address: 147.91.1.45

This content was downloaded on 10/08/2015 at 13:24

Please note that [terms and conditions apply](#).

Structural properties of particle deposits at heterogeneous surfaces

D Stojiljković¹, J R Šćepanović¹, S B Vrhovac¹
and N M Švrakić^{1,2}

¹ Institute of Physics Belgrade, University of Belgrade, Pregrevica 118, Zemun 11080, Belgrade, Serbia

² Texas A&M University at Qatar, Doha, Qatar
E-mail: vrhovac@ipb.ac.rs

Received 17 March 2015

Accepted for publication 23 May 2015

Published 23 June 2015



Online at stacks.iop.org/JSTAT/2015/P06032
[doi:10.1088/1742-5468/2015/06/P06032](https://doi.org/10.1088/1742-5468/2015/06/P06032)

Abstract. The random sequential adsorption (RSA) approach is used to analyze adsorption of spherical particles of a fixed radius on nonuniform flat surfaces covered by rectangular cells. The configuration of the cells (heterogeneities) was produced by performing RSA simulations to a prescribed coverage fraction $\theta_0^{(\text{cell})}$. Adsorption was assumed to occur if the particle (projected) center lies within a rectangular cell area, i.e. if sphere touches the cells. The jammed-state properties of the model were studied for different values of cell size α (comparable with the adsorbing particle size) and density $\theta_0^{(\text{cell})}$. Numerical simulations were carried out to investigate adsorption kinetics, jamming coverage, and structure of coverings. Structural properties of the jammed-state coverings were analyzed in terms of the radial distribution function $g(r)$ and distribution of the Delaunay ‘free’ volumes $P(v)$. It was demonstrated that adsorption kinetics and the jamming coverage decreased significantly, at a fixed density $\theta_0^{(\text{cell})}$, when the cell size α increased. The predictions following from our calculation suggest that the porosity (pore volumes) of deposited monolayer can be controlled by the size and shape of landing cells, and by anisotropy of the cell deposition procedure.

Keywords: adsorbates and surfactants (theory), stochastic processes (theory)

Contents

1. Introduction	2
2. Model and numerical simulation	4
3. Results and discussion	5
3.1. Circles on squares	5
3.1.1. Densification kinetics.	6
3.1.2. Radial distribution function.	12
3.1.3. Volume distribution of the pores.	14
3.2. Circles on rectangles	18
4. Concluding remarks	20
Acknowledgments	22
References	22

1. Introduction

Recent developments in new and emerging technologies have generated increased demand for nano and micro-sized particles with carefully tailored properties for use in applications such as photonics, micro-electronics, plasmonics, biosensors, bio-medical devices, etc. In many applications, such nanoparticles are often integrated onto surfaces in the form of deposits in order to achieve improved performance and/or new functionalities of the final product. Thus, in addition to specific requirements for particles of definite shape, size, internal structure, surface properties or chemical composition, it is also important to be able to manipulate collective arrangements of such particles with firm control over the morphology and structure of their surface layers. To achieve this goal, the supporting surfaces are frequently prepatterned to form the templates favoring particle attachments at specific locations [1,2], or dimples, or along specified shapes, regular or otherwise [3,4]. With the use of photolithographic techniques, high-power lasers [1], chemical treatments, etc, such surface modifications are routinely realized on the microscale, but the trend is towards the nanosize patterning [1–4].

In contrast with homogeneous surfaces, the prepatterned *heterogeneous* substrates are designed with preferential attachment sites, or regions [4]. Thus, it is of theoretical and experimental interest to understand and analyze how specific surface modifications affect the morphology of deposited layers, late-stage kinetics of attachment, etc. Our analysis, described below, focuses on structural properties of particle deposits and is applicable to the presence of *randomness* in surface patterning on the scales comparable to particle size.

Specifically, in the present work, we report a study of the irreversible deposition of spherical particles on flat nonuniform substrates covered by rectangular cells onto which the particles can adhere. The adsorption sites (landing cells) have finite size, comparable with the adsorbing particle size. We consider the process of the irreversible random sequential adsorption (RSA) of fixed size disks (projection of spherical particles). RSA is a process in which the objects of specified shape are randomly and sequentially deposited onto a substrate [5–10]. The particle-particle interaction is incorporated by rejection of deposition overlap (the hard sphere model), while the particle-substrate interaction is modeled by the irreversibility of deposition. Adsorption attempt of a particle at a randomly chosen cell is abandoned if there is an overlap with a previously adsorbed one, at the same or at a neighboring cell. Since the dominant effect in RSA is the blocking of the available surface area, after sufficiently long time a jammed state is reached when there is no more possibility for a deposition event on any landing cell. In this work we focus on the jammed-state properties.

There is a well-developed literature on irreversible adsorption on heterogeneous surfaces where particles are represented as hard spheres that bind to adsorption sites [10–15]. Our present model represents a generalized version of deposition on a random site surface (RSS), where the sites are represented by randomly distributed points [11, 13]. Adamczyk *et al* [14] has extended the RSS model to the situation where the size of the landing sites, in the shape of circular disks, is finite and comparable with the size of adsorbing spheres. The available surface function, adsorption kinetics, jamming coverage, and the structure of the particle monolayer were determined as a function of the site density and the particle/site size ratio.

The motivation of our present work comes from Margues *et al* [16] and Araújo *et al* [17], who investigated the adsorption of disk-shaped particles on a patterned substrate. The pattern consisted of equal square cells centered at the vertices of a square lattice. They studied the effect of the presence of a regular substrate pattern and particle polydispersity on the deposit morphology and density, as well as on the in-cell particle population. A specific distribution function was used to describe the degree to which the cell pattern affects the overall structure of the adsorbed layer for various values of cell size and cell-cell separation parameters. It was found that the structural organization of the deposit could be latticelike, locally homogeneous, and locally oriented.

The present work is focused on the effect of the presence of randomness in substrate pattern on the structural properties of the disordered jammed state. Our aim is to quantify structural changes of the jamming covering associated with different cell size and density. Analysis at the ‘microscopic’ scale is based on the Voronoï tessellation [18]. Voronoï tessellation divides a two-dimensional region occupied by disks into space filling, nonoverlapping convex polygons. Further, the Delaunay triangulation is used to quantify the volume distribution of pores $P(v)$ for disk monolayers deposited on a heterogeneous substrate. This quantity has been widely used to characterize the structure of disordered granular packings and to quantify the structural changes during compaction process [19–23]. We choose as our additional tool of exploration the shape of radial correlation function $g(r)$ [24]. This is because this function provides a simple yet powerful encoding of the distribution of interparticle gaps. We also study the effect of the presence of a regular substrate pattern on the temporal evolution of the coverage fraction $\theta(t)$ and the pore distribution $P(v)$. The pattern consists of an array of cells centered on the vertices of a square lattice [16, 17].

The following section 2 describes the details of our numerical simulations. We present simulation results and discussions in section 3. Finally, section 4 contains some additional comments and concluding remarks.

2. Model and numerical simulation

We study irreversible monolayer deposition of identical disks (sphere projections) with hard-core exclusion on a prepared flat nonuniform substrate. The substrate heterogeneities are represented by non-overlapping rectangular cells that are randomly placed and fixed on the substrate surface. The basic assumption of our model is that a particle can only be adsorbed if it is in contact with one of the cells, i.e. if the center of its disk-shaped projection lies within one of the rectangles. The substrates can be prepared in a number of ways by arranging the rectangles to form different patterns, e.g. by placing the midpoint of rectangles at the vertices of a square or triangular lattice (regular pattern), or by performing random deposition (random pattern), the procedure adopted in our work. We consider particles of fixed radius, comparable with the typical geometrical cell length. Moreover, we assume that the size of the particles is much larger than the length scale between binding sites, so that adsorption over the length scales of cell linear dimensions can be regarded as an off-lattice process. We impose the condition that deposited particles can neither diffuse along, nor desorb from the substrate on the time scales of the dense coverage formation. These assumptions are typical of the RSA model.

The simplest RSA model is defined by the following three rules: (i) objects are placed one after another at a random position on the substrate; (ii) adsorbed objects do not overlap; and (iii) adsorbed objects are permanently fixed to their spatial positions. The kinetic properties of a deposition process are described by the time evolution of the coverage $\theta(t)$, which is the fraction of the substrate area covered by the adsorbed particles. Within a monolayer deposit, each adsorbed particle affects the geometry of all later placements. Due to the blocking of the substrate area by the previously adsorbed particles, at large times the coverage approaches the jammed-state value θ_J , where only gaps too small to accommodate new particles (provided their centers fall within landing cells) are left in the monolayer.

The entire simulation procedure consisted of two main stages:

1. The simulation area was covered with identical rectangles (or squares) to a prescribed coverage fraction $\theta_0^{(\text{cell})} < \theta_J^{(\text{cell})}$, where $\theta_J^{(\text{cell})}$ is the jamming coverage for landing cells. During this stage the usual RSA simulation algorithm was used. In this way we are able to prepare the randomly patterned heterogeneous substrate with a statistically reproducible density $\theta_0^{(\text{cell})}$.
2. Then, for each initially prepared configuration, we switch the cell deposition events off and initiate a random deposition of disks, with diameter d_0 , by choosing at random their position within the simulation area. The overlapping test between disks was carried out by considering the distances between the disk centers. A disk deposition attempt fails if disk's center falls outside the deposited landing cells, or if the arriving disk overlaps at least one of previously adsorbed ones.

The Monte-Carlo simulations are performed on a planar continuous substrate of size $L \times L = (256d_0)^2$ with periodic boundary conditions. In calculations, the time t is gradually increased by an increment δt , given by $\delta t = \pi r_0^2 / L^2$, each time an attempt is made to deposit a disk of radius $r_0 = d_0/2$. Consequently, we define dimensionless parameter $t = N_{\text{att}} \pi r_0^2 / L^2$, where N_{att} is the overall number of attempts to place disk particles. The dimensionless adsorption time t was set to zero at the beginning of the second stage. By plotting $\theta(t)$ versus the adsorption time t , defined above, one can simulate the kinetics of particle adsorption.

For purposes of our modeling, each landing cell is a rectangle with sides a and b ($b \leq a$) whose midpoint is located on a continuous substrate. The cells can take arbitrary orientations, but in some numerical simulations we have introduced anisotropy in the deposition procedure for landing cells. This simple modification introduces a preferential direction in the deposition process and, depending on the aspect ratio of deposited rectangles, imposes specific ‘patterning’ on the deposited layer. We rescale the lengths relative to the diameter of the disks d_0 , and define three dimensionless parameters:

$$\alpha = \frac{a}{2r_0}, \quad \beta = \frac{b}{2r_0} \quad (1)$$

$$\gamma = \frac{\alpha}{\sqrt{\theta_0^{(\text{cell})}}} \quad (2)$$

The parameter γ (an average distance between cell centers) is a meaningful measure only if the landing cells are squares ($a = b$).

For a fixed values of parameters α and β , simulations were carried out for various values of $\theta_0^{(\text{cell})}$, ranging from 0.10 to 0.50. For each case, the simulations are carried out up to 10^{10} deposition attempts, or up until $L^2 \times 10^4$ consecutive deposition attempts are rejected. The results are obtained by averaging over 100 simulation runs.

3. Results and discussion

In the first part of this section simulation results are presented and discussed for random deposition of identical disks on nonuniform substrates covered by squares of arbitrary orientation. We characterize the jammed state in terms of radial distribution function of distances between the particle centers and distribution of the Delaunay ‘free’ volumes. After that, further analysis is extended to adsorption of disks on rectangular cells deposited with arbitrary or fixed orientation.

3.1. Circles on squares

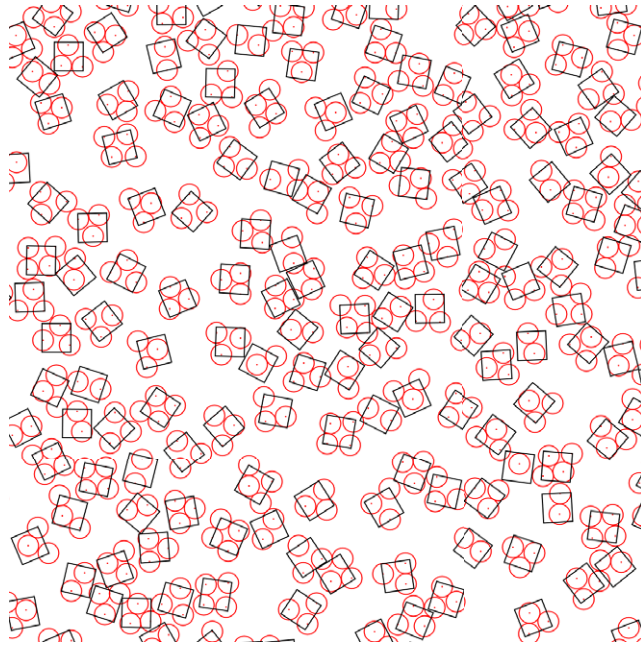
First, we consider the irreversible deposition of disks of fixed diameter $d_0 = 1$ whose centers are inside the square cells arranged randomly at the surface. Depending on the cell size α , one can place one or more disk centers inside each cell. We are interested in the range of α where the number of disks adsorbed per cell is a small number (less than five). For $\alpha < 1/\sqrt{2}$, at most a single disk can be adsorbed at any given square cell. We denote this case as single particle per-cell adsorption (SPCA). For

squares with $\alpha \geq 1/\sqrt{2}$, more than a single disk can be placed in the square cell, and we denote this as multiparticle per-cell adsorption (MPCA). The cases of up-to-two, -three and -four disks per square cell are obtained, respectively, for α in the ranges $1/\sqrt{2} \leq \alpha < (1 + \sqrt{3})/(2\sqrt{2})$, $(1 + \sqrt{3})/(2\sqrt{2}) \leq \alpha < 1$, and $1 \leq \alpha < \sqrt{2}$. In other words, the numbers $\{\alpha_k : k = 1, 2, 3, 4\} = \{1/\sqrt{2}, (1 + \sqrt{3})/(2\sqrt{2}), 1, \sqrt{2}\}$ determine the size of the largest cell in which at most $k = 1, 2, 3, 4$ disks can be deposited, respectively.

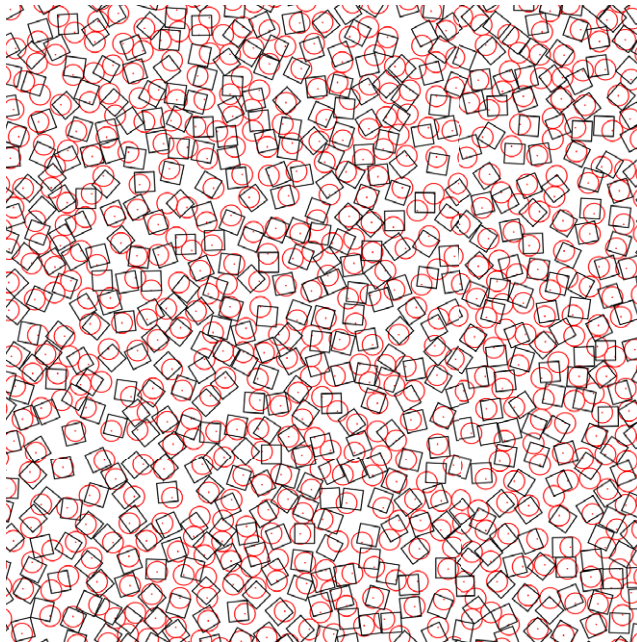
The effect of density of landing cells $\theta_0^{(\text{cell})}$ on the adsorption process is illustrated in figure 1 by snapshots of the jammed-state coverings for (a) $\theta_0^{(\text{cell})} = 0.3$ and (b) $\theta_0^{(\text{cell})} = 0.5$, for two values of the cell size α , namely, $\alpha_4 = \sqrt{2} \approx 1.41$ (figure 1(a)) and $\alpha_2 = (1 + \sqrt{3})/(2\sqrt{2}) \approx 0.966$ (figure 1(b)). For low values of $\theta_0^{(\text{cell})}$, adsorption on a given cell is weakly affected by disks previously adsorbed on neighboring cells. Therefore, most of the cells shown in figure 1(a) contain at least three discs. However, in the case shown in figure 1(b) one can see a significant impact of the cell-cell excluded volume interaction on the cell population. Although each cell has enough area to accommodate up to two disks, only one disk is deposited on most of the cells.

3.1.1. Densification kinetics. Kinetics of the irreversible deposition of disks is illustrated in figures 2(a)–(e) where the plots of time coverage behavior $\theta(t)$ are given for the five values of coverage fraction of landing cells, $\theta_0^{(\text{cell})} = 0.1, 0.2, 0.3, 0.4, 0.5$. Here the plots of such time-dependence are shown for various values of the cell size, α_k ($k = 1, 2, 3, 4$). It can be seen that for a fixed density of landing cells $\theta_0^{(\text{cell})}$, jamming coverage $\theta_J = \lim_{t \rightarrow \infty} \theta(t)$ decreases with increasing the cell size α_k . This effect is clearly visible in the case of the lowest density of the landing cells $\theta_0^{(\text{cell})} = 0.1$ (figure 2(a)), when the average distance between the squares γ (equation (2)) is several times larger than the diameter of the disks. Then, the cell-cell separation is large enough so that adsorption on a given cell is negligibly affected by disks previously adsorbed on neighboring cells. Therefore, for sufficiently low densities $\theta_0^{(\text{cell})} \lesssim 0.2$, the global kinetics of deposition is determined by the kinetics of independent adsorption processes on finite-size substrates (landing cells) with specific boundary conditions (disks can be adsorbed on finite $\alpha \times \alpha$ square as long as their centers are within the square). Consequently, for this range of $\theta_0^{(\text{cell})}$ values, formula $\theta_J = (\pi/4\alpha^2)\langle n \rangle \theta_0^{(\text{cell})}$ gives very close estimation of the jamming density θ_J , where $\langle n \rangle$ is the mean number of disks per cell. The dashed (black) line in figure 3 shows the simulation results for the mean number of particles per cell $\langle n \rangle$ as a function of the cell size α in the noninteracting cell-cell adsorption regime (i.e. in the case of single cell on a substrate).

Consider now the case of up-to-two disks per square cell ($\alpha_2 = (1 + \sqrt{3})/(2\sqrt{2}) \approx 0.966$), when $\langle n \rangle \lesssim 1.6$ (see, figure 3). Then, during the deposition process, disk can be adsorbed at the position inside the cell that blocks the chance for other disks to be adsorbed on the same cell at later times. Consequently, the probability of having a second adsorbed particle in any given cell is smaller than the probability of having at least one particle adsorbed on it. Similar reasoning applies as α crosses $\alpha_3, \alpha_4, \dots$. In addition, in figure 3 we show simulation results for the probability that the configurations with only one disk, or $n = 2, \dots, 5$ disks, occur on square cell of size α in the noninteracting cell-cell adsorption regime. If $\alpha = \alpha_1 \approx 0.707$, each landing cell (square) can contain no more than one disk. If $\alpha = \alpha_2 \approx 0.966$, the number of cells with one and two disks is



(a)



(b)

Figure 1. Typical jammed-state configuration of a region of size 30×30 in units of the disk diameter d_0 , for (a) $\theta_0^{(\text{cell})} = 0.3$, $\alpha_4 = \sqrt{2} \approx 1.41$, and (b) $\theta_0^{(\text{cell})} = 0.5$, $\alpha_2 = (1 + \sqrt{3})/(2\sqrt{2}) \approx 0.966$.

approximately equal (figure 3). However, if density $\theta_0^{(\text{cell})}$ is unchanged, then the increasing of the cell size $\alpha_1 \rightarrow \alpha_2$ reduces the total number of landing cells on the substrate by a factor ≈ 2 . Reduction in number of adsorbed disks is a consequence of these two effects.

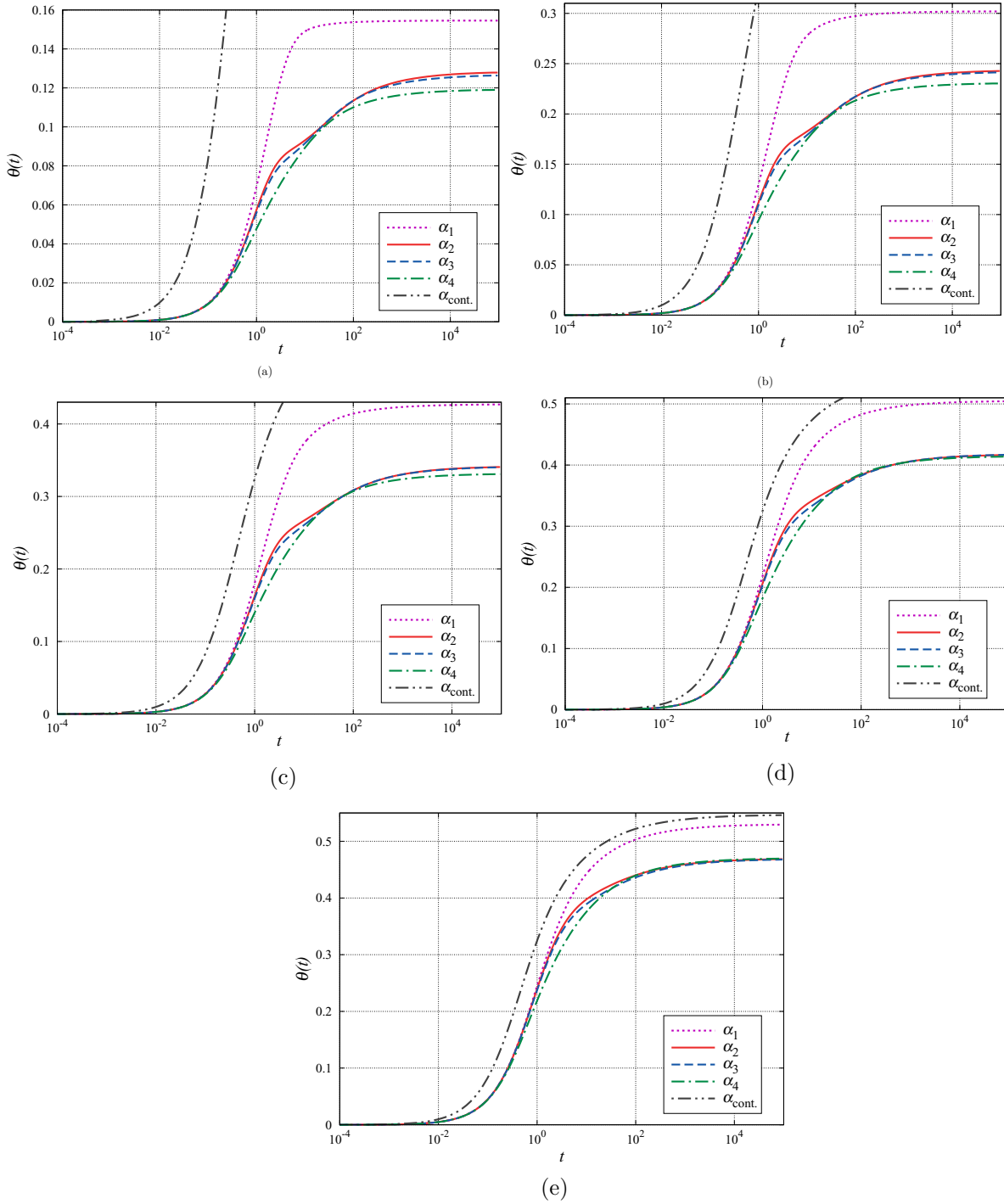


Figure 2. Shown here is the time evolution of the coverage fraction $\theta(t)$ for the five values of density of landing cells, $\theta_0^{(\text{cell})} = 0.1$ (a), 0.2 (b), 0.3 (c), 0.4 (d), 0.5 (e). The curves in each graph correspond to various values of the cell size, α_k ($k = 1, 2, 3, 4$), as indicated in the legend. The α_{cont} line shows the time dependence of the coverage $\theta(t)$ for RSA of disks on a continuous substrate. The entire α_{cont} curve can be seen in plot (e).

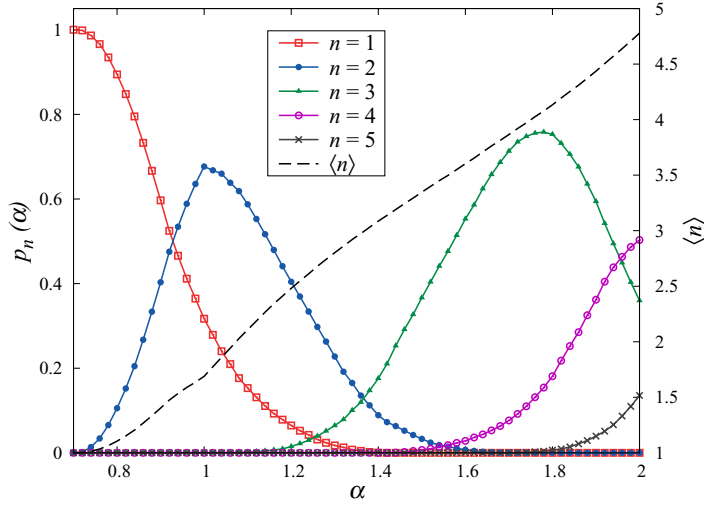


Figure 3. Simulation results for the probability that the configurations with $n = 1, 2, \dots, 5$ disks occur on square cell of size α in the noninteracting cell–cell adsorption regime (left-hand axis). The dashed line is plotted against the right-hand axis and gives the simulation results for the average number of particles per cell $\langle n \rangle$ as a function of the cell size α in the noninteracting cell–cell adsorption regime.

This discussion indicates that the jamming density θ_J decreases with cell size α at fixed density $\theta_0^{(\text{cell})}$.

As can be seen from figure 2, the time coverage behavior $\theta(t)$ is markedly slowed down with the increase of the cell size α for the fixed density of landing cells $\theta_0^{(\text{cell})}$. Indeed, in MPCA case the large times are needed for filling of small isolated vacant targets on landing cells, remaining in the late stages of deposition. Furthermore, in this regime, density curves $\theta(t)$ show a noticeable slowing down of deposition process at coverages that are significantly smaller than jamming densities. Coverage growth starts to slow down at the moment when the number of adsorbed disks reaches the number of landing cells. After this initial filling of the landing cells, adsorption events take place on isolated islands of partially occupied cells. This extends the time interval between successful consecutive adsorption events and causes a slowing down of the densification.

The results for the time evolution of the coverage $\theta(t)$ in the case of up-to-two disks per square cell ($\alpha = \alpha_2$) are shown in figure 4 for various values of $\theta_0^{(\text{cell})}$. Qualitatively similar results are obtained with landing cells of other sizes α . As expected, the jamming density θ_J increases with higher coverage fraction of landing cells $\theta_0^{(\text{cell})}$. At high values of $\theta_0^{(\text{cell})} \lesssim 0.5$ when $\gamma \sim 1$, a disk attempting adsorption can overlap with a previously adsorbed one belonging to a different cell, resulting in a failed adsorption attempt. This excluded volume interaction between particles during adsorption at *different* cells causes even slower asymptotic approach of the coverage fraction $\theta(t)$ to its jamming limit. In addition, the analysis of the time evolution of the coverage $\theta(t)$ was carried out for deposition on square cells centered at the vertices of a square lattice. Consequently, the temporal evolution of the coverage $\theta(t)$ obtained for regular substrate pattern are included in figure 4. Here, the size α and density $\theta_0^{(\text{cell})}$ of landing cells are the same as those used in

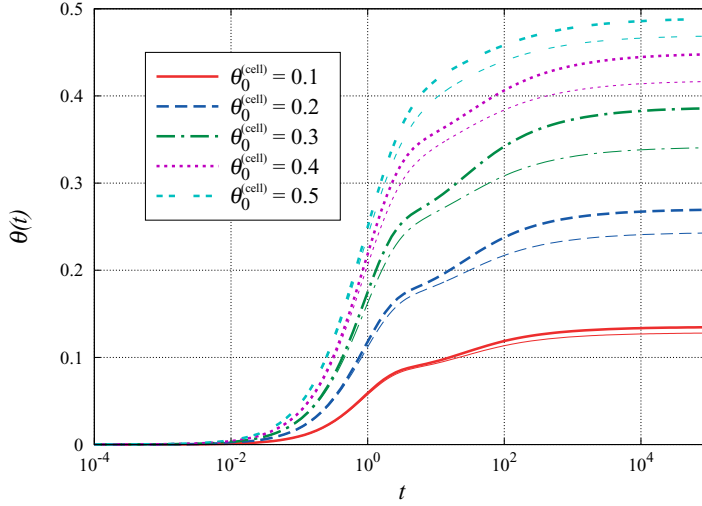


Figure 4. Temporal behavior of the coverage $\theta(t)$ for various values of $\theta_0^{(\text{cell})}$ in the case of up-to-two disks per square cell (cell size: $\alpha_2 = (1 + \sqrt{3})/(2\sqrt{2}) \approx 0.966$). The curves correspond to various values of density $\theta_0^{(\text{cell})} = 0.1-0.5$, as indicated in the legend. Thick lines represent results obtained for regular substrate pattern while thin lines are results for random pattern case.

our previous calculations for random pattern case. It can be seen that lower values of the jamming coverage fraction are reached by the deposition process involving randomness in the pattern compared to a deposition process in the presence of a regular substrate pattern, regardless of the value of the density $\theta_0^{(\text{cell})}$.

Below we try to characterize quantitatively the time dependence of the approach to the jammed state at large times. Depending on the system of interest modeled by RSA, the substrate can be continuous (off lattice) or discrete. Asymptotic approach of the coverage fraction $\theta(t)$ to its jamming limit, $\theta_J = \theta(t \rightarrow \infty)$, is known to be given by an algebraic time dependence for continuous substrates [25–29]:

$$\theta(t) \sim \theta_J - At^{-1/d}, \quad (3)$$

where A is a constant coefficient and d is interpreted as substrate dimension [26] in case of spherical particles adsorption or, more generally, as a number of degrees of freedom [30]. For lattice RSA models, the approach to the jamming coverage is exponential [31–36]:

$$\theta(t) \sim \theta_J - \Delta\theta \exp(-t/\sigma), \quad (4)$$

where parameters θ_J , $\Delta\theta$, and σ depend on the shape and orientational freedom of depositing objects [34, 36].

Representative examples of the double logarithmic plots of the first derivative of coverage $\theta(t)$ with respect to time t are shown in Figure 5(a), for various values of the cell size, α_k ($k = 1, 2, 3, 4$), and for high density of landing cells, $\theta_0^{(\text{cell})} = 0.5$. The time derivatives of $\theta(t)$ are calculated numerically from the simulation data. In the case of the algebraic behavior of the coverage fraction $\theta(t)$ (equation (3)), a double logarithmic plot of the first time derivative $\frac{d\theta}{dt} \propto t^{-\frac{1+d}{d}}$ is a straight line. One can see that curves shown in figure 5(a) are straight lines in the late stage of deposition process. However, the same is not valid for all values of densities of landing cells $\theta_0^{(\text{cell})}$. The double logarithmic plots

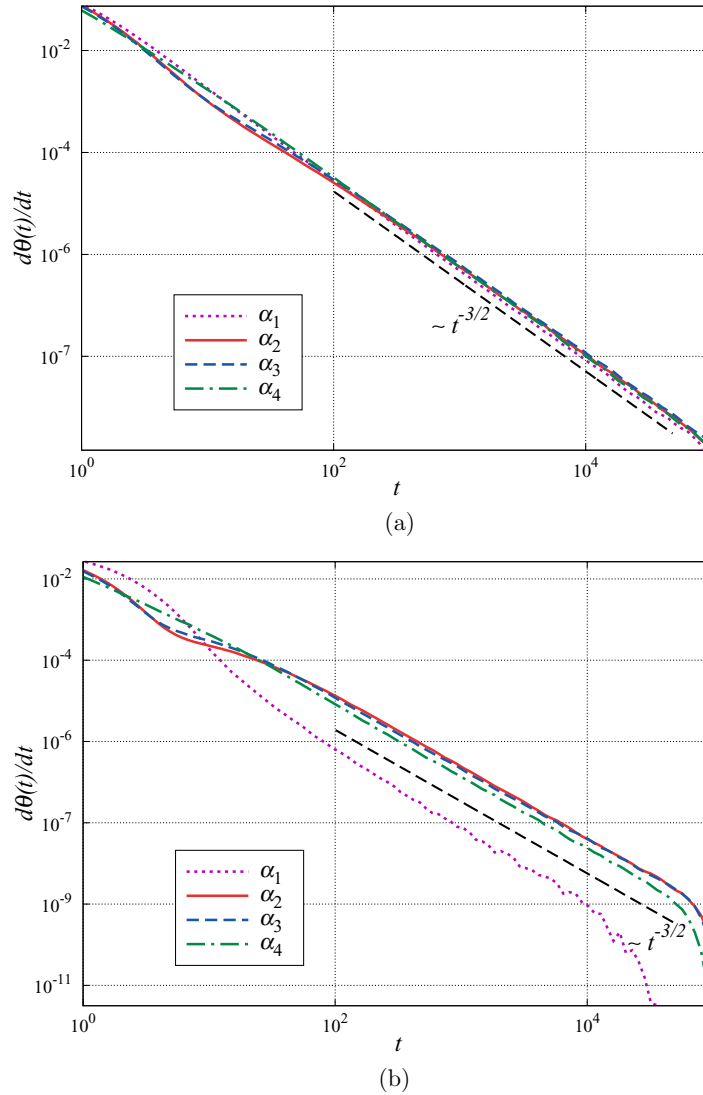


Figure 5. Test for the presence of the algebraic law (3) in the approach of the coverage $\theta(t)$ to the jamming limit for different densities of landing cells: (a) $\theta_0^{(\text{cell})} = 0.5$, and (b) $\theta_0^{(\text{cell})} = 0.1$. The curves in each graph correspond to various values of the cell size, α_k ($k = 1, 2, 3, 4$), as indicated in the legend. Straight line sections of the curves show where the law holds. The dashed black line has slope $-3/2$ and is a guide for the eye.

of the numerically calculated derivatives of $\theta(t)$ for the data obtained in the case of low density of landing cell $\theta_0^{(\text{cell})} = 0.1$ are shown in figure 5(b). As it can be seen, at the very late times of the deposition process the plot of the first derivative of coverage fraction $\theta(t)$ with respect to time t is not linear on a double logarithmic scale, indicating that the approach to the jamming limit is not consistent with the power law behavior given by equation (3). The deviation from the power law is particularly pronounced in the case of single particle per-cell adsorption (SPCA).

Kinetics of the irreversible deposition under SPCA conditions is illustrated in figure 6 where a logarithmic plots of $\theta_J - \theta(t)$ versus t are shown for various densities of landing

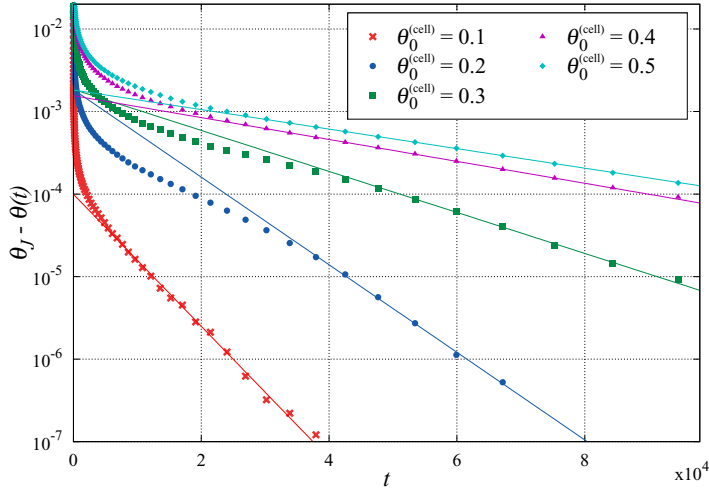


Figure 6. Plots of $\theta_J - \theta(t)$ versus t in the single particle per-cell adsorption case for various densities of landing cells $\theta_0^{(\text{cell})} = 0.1$ – 0.5 . The solid lines are the exponential fit of equation (4).

cells $\theta_0^{(\text{cell})}$. These plots are straight lines for the late times of deposition, suggesting that in the case of SPCA the approach to the jamming limit is indeed exponential, as in lattice RSA models. Indeed, the kinetics of deposition in SPCA case is determined by the kinetics of adsorption processes on finite-size landing cells. The difference relative to the lattice RSA is in the particle positions, which here are uncertain within the order of the size of the cell.

3.1.2. Radial distribution function. Here we compare quantitatively the structural characteristics of jamming coverings corresponding to different values of the cell size α for various densities $\theta_0^{(\text{cell})}$. In order to gain basic insight into the ‘microstructure’ of the jammed state, we first consider the radial distribution function $g(r)$ (or pair-correlation function) which gives information about the long-range interparticle correlations and their organization [24]. In absence of external forces, the pair correlation function can be calculated from expression

$$g(r) = \frac{S \overline{N}_a(r)}{N 2\pi r \Delta r}, \quad (5)$$

where r is the radial coordinate, S is the surface area, N is total number of particles adsorbed over this area, and \overline{N}_a is the averaged number of particles within the annulus of the radius r and the thickness Δr . In figure 7(a) we compare the radial distribution function $g(r)$ at various densities $\theta_0^{(\text{cell})} = 0.1$ – 0.5 in the SPCA case. As expected, the random deposition process never leads to correlation distances between the deposited particles exceeding two or three particle diameters. The position of the first peak measures typical distances between the closest disks. Decreasing the value of $\theta_0^{(\text{cell})}$ in the SPCA case increases the uncertainty in the position of the particles which leads to peak broadening. The shape of radial distribution $g(r)$ is more structured at higher densities, showing higher first and second peaks, because, when the system gets denser, particles will be deposited closer to one another. As can be seen from figure 7(a), the minima of $g(r)$ curves shift to

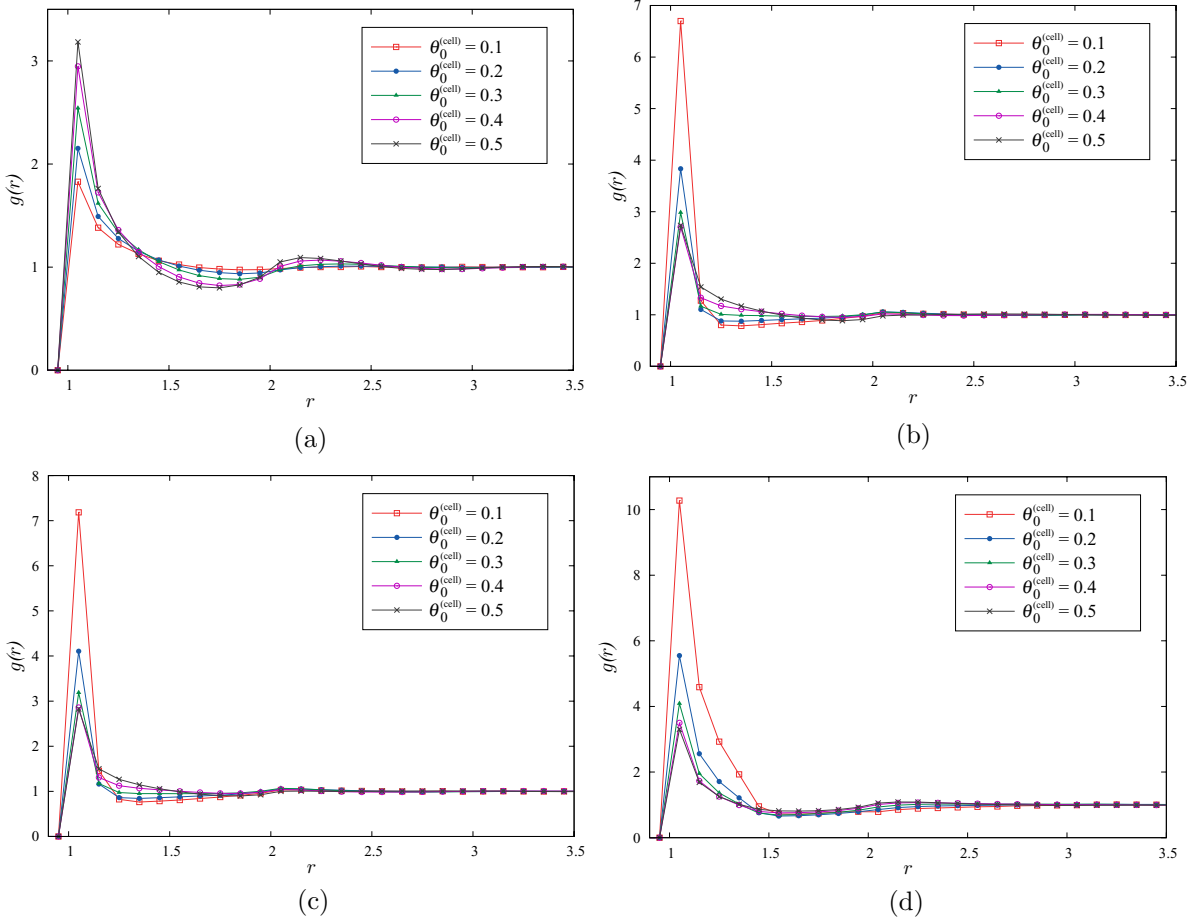


Figure 7. Radial distribution function $g(r)$ for jamming coverings as a function of separation r (in units of the disk diameter d_0) for various values of the cell size α : (a) $\alpha_1 = 1/\sqrt{2}$, (b) $\alpha_2 = (1 + \sqrt{3})/(2\sqrt{2})$, (c) $\alpha_3 = 1$, (d) $\alpha_4 = \sqrt{2}$. The curves in each graph correspond to various values of density $\theta_0^{(\text{cell})} = 0.1, 0.2, 0.3, 0.4, 0.5$, as indicated in the legend.

shorter distances ($\sim \sqrt{3}$) when the density $\theta_0^{(\text{cell})}$ increases. At a very low densities, the broad minima are located near the distance $\sim 2d_0$. Indeed, since the particles are added at random, the probability that disks are connected as a three-bead chain is negligible.

The results for $g(r)$ in the MPCA case are shown in figures 7(b)–(d). The shape of the radial distribution function $g(r)$ is significantly affected by the values of the cell size α . In the case of up-to-two disks per square cell (figure 7(b)) the peak which appears at unit distance is the most pronounced for low densities of landing cells $\theta_0^{(\text{cell})}$. For low values of $\theta_0^{(\text{cell})}$, one expects a lower impact of the cell–cell excluded volume interaction on the cell population. However, as $\theta_0^{(\text{cell})}$ increases, the first peak of $g(r)$ becomes broader because excluded volume interaction with disks belonging to neighboring cells reduces the average number of adsorbed disks per cell. This is opposite to what is observed under SPCA conditions (figure 7(a)), where the distance to the closest disk, on average, is determined by the distance of the nearest-neighbor landing cells.

The comparison of figures 7(b) and (c) shows that the results for $g(r)$ in the case of up-to-two and up-to-three disks per square cell are very similar. This arises as a direct consequence of the fact that cells with sizes $\alpha_2 \approx 0.966$ and $\alpha_3 = 1$ have very similar population of particles (see figure 3). Figure 7(d) shows the radial distribution function $g(r)$ of jamming coverings at several densities $\theta_0^{(\text{cell})}$ obtained in simulations carried out with the cell size of $\alpha_4 = \sqrt{2}$. For this value of the parameter α , each cell is of sufficient size to accommodate up to four particles. As can be seen in figures 7(b)–(d), increasing the value of parameter α in the MPCA case increases the uncertainty in the position of the disk within the cell, i.e. it leads to peak broadening.

3.1.3. Volume distribution of the pores. Further analysis is based on the Voronoï tessellation, which allows us to unambiguously decompose any arbitrary arrangement of disks into space-filling set of cells. Given a set \mathcal{A} of discrete points in the plane π (centers of disks), for almost any point $x \in \pi$ in the plane π there is one specific point $a_i \in \mathcal{A}$ which is closest to x . The set of all points of the plane which are closer to a given point $a_i \in \mathcal{A}$ than to any other point $a_j \neq a_i$, $a_j \in \mathcal{A}$, is the interior of a convex polygon \mathcal{P}_i usually called the Voronoï cell of a_i . The set of the polygons $\{\mathcal{P}_i\}$, each corresponding to (and containing) one point $a_i \in \mathcal{A}$, is the Voronoï tessellation corresponding to \mathcal{A} , and provides a partitioning of the plane π . Voronoï cells are convex and their edges join at trivalent vertices, i.e. each vertex is equidistant to three neighboring disks. Two disks sharing a common cell edge are neighbors. In this work, the Quickhull algorithm [37] is used to compute the Voronoï diagrams in MATLAB[®] for a given set of disks on a plane.

The jammed-state coverings are analyzed in terms of volume distributions of the pores. The convenient definition of a pore is based on the Delaunay triangulation (DT), which is a natural way to subdivide a 2D structure of disks into a system of triangles with vertices at the centers of neighboring disks. Consequently, the circle circumscribing a Delaunay triangle has its center at the vertex of a Voronoï polygon. In this work we define the pore as a part of the Delaunay triangle not occupied by the disks (Delaunay ‘free’ volume) [21, 22]. The pore volume v is normalized by the ‘volume’ of the disks, $v_0 = d_0^2\pi/4$. In figure 8 we show Delaunay triangulation of typical jammed-state covering obtained for the same conditions as in figure 1(a) ($\theta_0^{(\text{cell})} = 0.3$, $\alpha_4 = \sqrt{2} \approx 1.41$). Looking at the diagram of figure 8, one can observe variations in the area of Delaunay triangles, which indicates the presence of pores of various sizes in the deposit.

Here we consider the probability distribution $P(v)$ of the Delaunay ‘free’ volume v . The distribution function $P(v)$ represents the probability of finding a pore with volume v . Fluctuations in the measurements of $P(v)$ are reduced by averaging over 100 different simulations, performed under the same conditions. We compare volume distribution of the pores $P(v)$ for jamming coverings corresponding to different values of the cell size α and various densities of landing cells $\theta_0^{(\text{cell})}$, as illustrated in figures 9(a)–(e). Here, the pore distributions $P(v)$ obtained for densities $\theta_0^{(\text{cell})} = 0.1, 0.2, 0.3, 0.4, 0.5$ have been plotted. At very low value of $\theta_0^{(\text{cell})} = 0.1$ (figure 9(a)), the curves of volume distribution $P(v)$ are asymmetric with a quite long tail on the right-hand side, which progressively reduces while the cell size α increases at the fixed density. At the same time, the distribution $P(v)$ becomes narrower and more localized around the low values of the pore volume v .

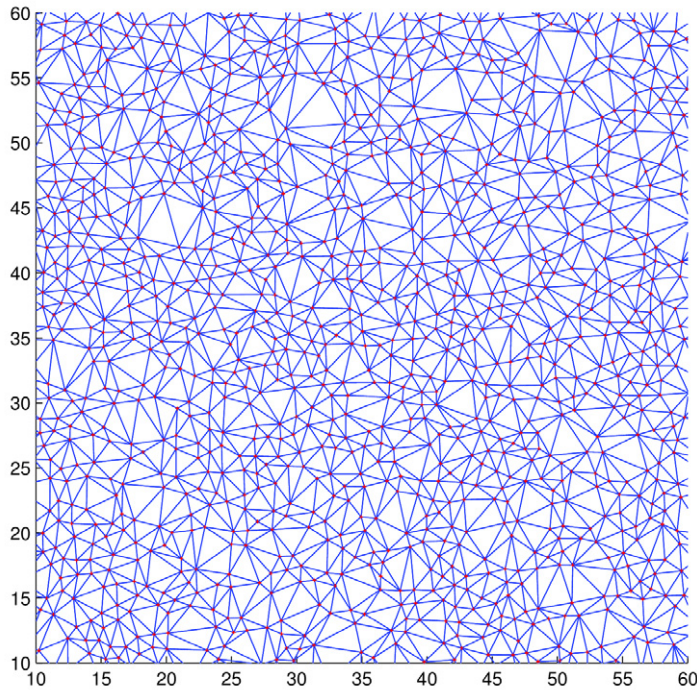


Figure 8. Delaunay triangulation of a set of points (centers of disks). Diagram corresponds to jammed-state covering obtained for density of landing cells $\theta_0^{(\text{cell})} = 0.3$ and cell size $\alpha_4 = \sqrt{2}$; see figure 1(a) for a typical configuration. The red dots are centers of the adsorbed disks. Length is measured in units of the disk diameter d_0 .

This behavior of the distribution $P(v)$ was not observed for all densities of landing cells $\theta_0^{(\text{cell})} = 0.1$ – 0.5 (see figures 9(a)–(e)). For densities $\theta_0^{(\text{cell})} \geq 0.2$, the pore distributions $P(v)$ obtained for deposition on square cells of size α_2 and α_3 are broader and shifted to higher values of volumes v compared to the pore distribution $P(v)$ corresponding to SPCA case (α_1). Qualitative interpretation of this result is given below.

In the case of up-to-four disks per square cell ($\alpha_4 = \sqrt{2}$), we observe the appearance of pronounced peak of $P(v)$ at low values of v , approximately at $v = 0.15$ – 0.20 . It is easy to understand which kind of local configuration contributes mostly to this peak of the $P(v)$. The Delaunay cells with free dimensionless volume $v_{\text{hex}} = \sqrt{3}/\pi - 1/2 \approx 0.051$ correspond to the local arrangements of hexagonal symmetry, when three disks are all in touch with each other with centers on the vertices of a unilateral triangle. The cells with free volume $v_{\text{quad}} = 2/\pi - 1/2 \approx 0.13$ correspond to the local configurations of quadratic symmetry, when centers of four touching disks are positioned on the vertices of a square. These are minimal values of pore volumes that can be formed with three and four disks deposited on a single landing cell of size $\alpha_4 = \sqrt{2}$. However, the probability that the previously described structures of quadratic and hexagonal symmetry arise during the process of random deposition is negligibly small. Therefore, the ‘free’ volumes formed with random deposition of disks into a single cell are larger than the minimal values $v_{\text{hex}} \approx 0.051$ and $v_{\text{quad}} \approx 0.13$, so that observed peak of $P(v)$ is around $v \lesssim 0.20$.

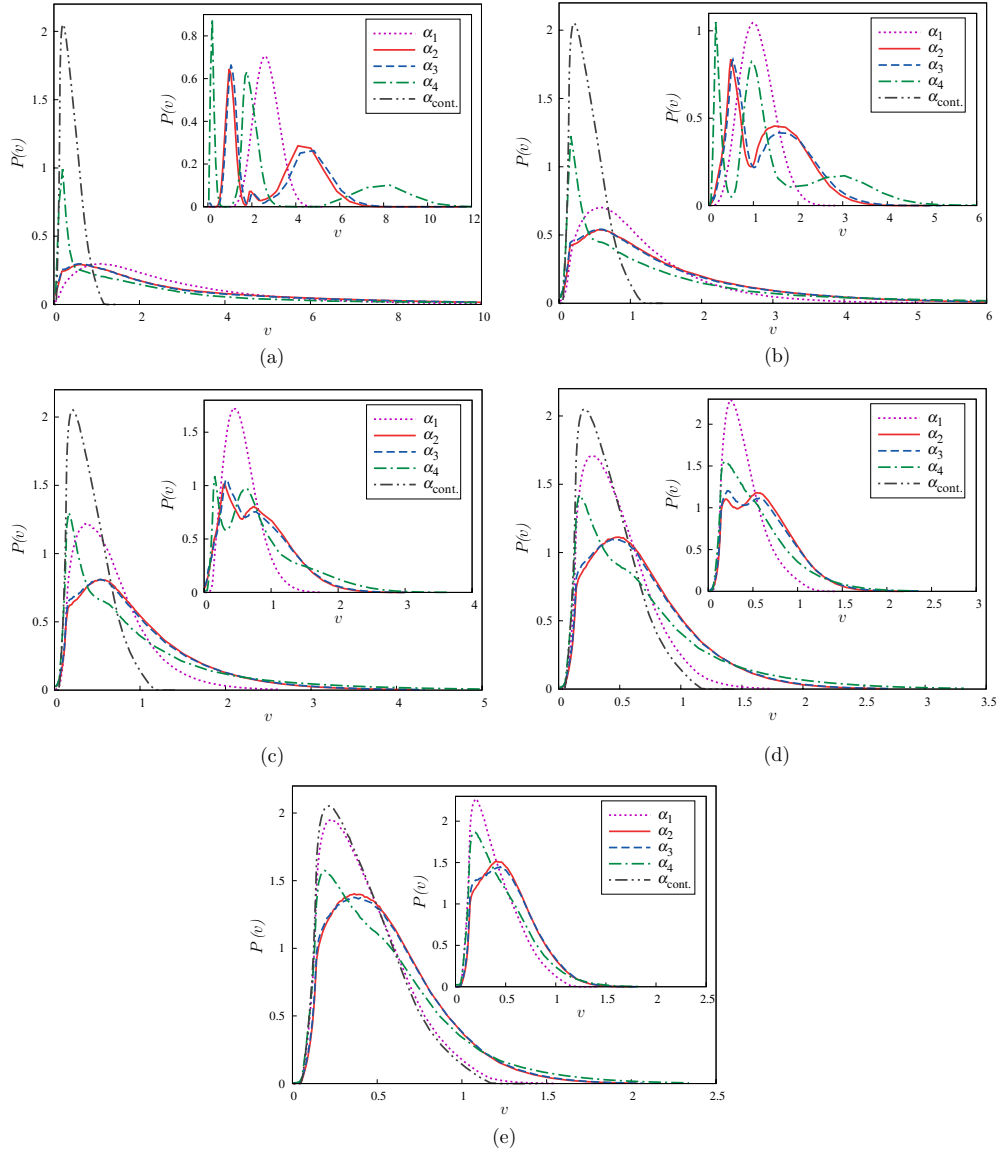


Figure 9. Main panel: Volume distribution of the pores $P(v)$ for jamming coverings at different values of density of the landing cells corresponding to $\theta_0^{(\text{cell})} = 0.1$ (a), 0.2 (b), 0.3 (c), 0.4 (d), 0.5 (e) are shown in the case of random pattern. The curves in each graph correspond to various values of the cell size, α_k ($k = 1, 2, 3, 4$), as indicated in the legend. The α_{cont} line shows distribution $P(v)$ for jamming covering in the case of the irreversible disks deposition on a continuous substrate. Insets: Volume distribution of the pores $P(v)$ for jamming coverings obtained from simulations carried out using the heterogeneous surface covered by square cells centered at the vertices of a square lattice. The size α and density $\theta_0^{(\text{cell})}$ of landing cells are the same as those used in the main panel.

At high values of density of landing cells $\theta_0^{(\text{cell})} = 0.5$ (figure 9(e)), distribution $P(v)$ obtained under SPCA conditions becomes very similar to pore volume distribution for RSA of disks on a continuous substrate, as expected. The results for the volume distribution of the pores $P(v)$ obtained in the cases of up-to-two and up-to-three disks

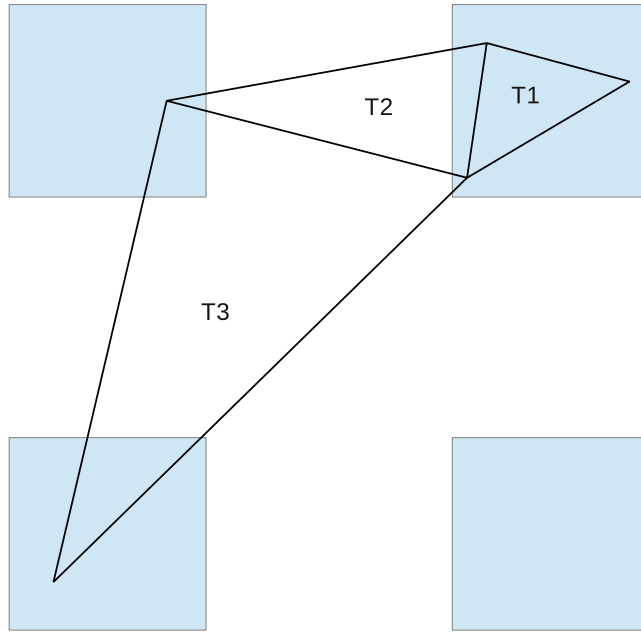


Figure 10. Various types of Delaunay triangles (T1–T3) depending on the position of vertices.

per square cell are almost identical at all densities $\theta_0^{(\text{cell})}$ (see figure 9). The similarity of these distributions at small values of pore volumes can be explained by the results shown in figure 3. Small pores appear due to the presence of configurations with three or more disks on a single landing cell. But, in the case of up-to-three disks per square cell, the number of in-cell configurations with three disk is considerably smaller than the number of configurations with one or two disks. Consequently, broad maximum in $P(v)$, centered at $v = 0.4\text{--}0.6$ is caused by contribution of large pores formed mostly in the space between the landing cells.

Further, we study the effect of the presence of a regular substrate pattern of squares on volume distribution of the pores $P(v)$. Distributions $P(v)$ for jamming coverings corresponding to $\theta_0^{(\text{cell})} = 0.1\text{--}0.5$ and different values of the cell size α_k ($k = 1, 2, 3, 4$) are shown in insets of figure 9. At low density of landing cells $\theta_0^{(\text{cell})} = 0.1$ and for large cell size $\alpha \geq \alpha_4 = \sqrt{2}$ (see inset of figure 9(a)) we observe the appearance of three peaks of $P(v)$. The first peak at $v \approx 0.2$ is due to Delaunay triangles with their vertices inside a single landing cell (see T1 triangle in figure 10). The third peak at $v \approx 8$ corresponds to Delaunay triangles with vertices located in different landing cells (see T3 triangle in figure 10). Central peak at $v \approx 2$ arises due to Delaunay triangles with two vertices belonging to single cell, while the third one is located in a neighboring cell (see T2 triangle in figure 10). The first peak at very low values of pore volumes v does not appear for the smaller landing cells, $\alpha = \alpha_1, \alpha_2, \alpha_3$. Indeed, if $\alpha \leq \alpha_3$, the Delaunay triangles that lie within a single landing cell are very rare ($\alpha = \alpha_3$) or they can not exist ($\alpha \leq \alpha_2$). In the case of single particle per-cell adsorption ($\alpha = \alpha_1$) vertices of each Delaunay triangle are located in three different cells, so that distribution $P(v)$ has only one broad maximum. As can be seen from insets of figure 9, the difference between distribution $P(v)$ for regular

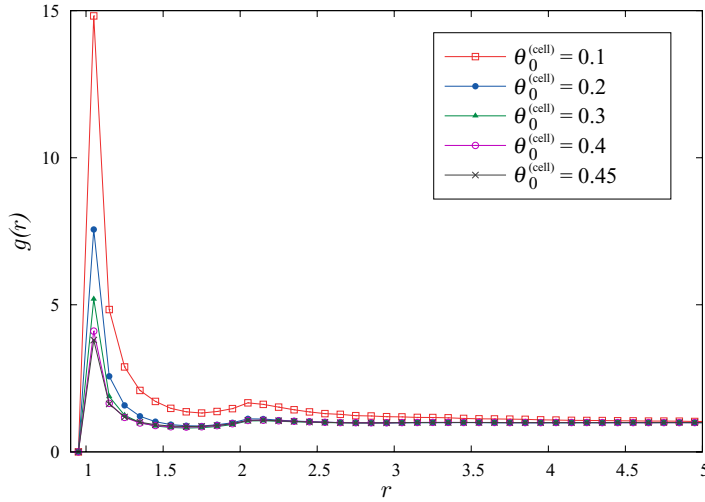


Figure 11. Radial distribution function $g(r)$ for jamming coverings as a function of separation r (in units of the disk diameter d_0) obtained from simulations carried out using the heterogeneous surface covered by rectangles of arbitrary orientation. The curves correspond to various values of density $\theta_0^{(\text{cell})} = 0.1, 0.2, 0.3, 0.4, 0.45$, as indicated in the legend.

substrate pattern of squares and for random pattern case decreases with the increase of the cell density $\theta_0^{(\text{cell})}$.

3.2. Circles on rectangles

We have also performed numerical simulations of random deposition of identical disks on heterogeneous surfaces covered by rectangles of arbitrary orientation. In these simulations, each landing cell is a rectangle with sides $\alpha = 8$ and $\beta = 1$ (in units of the disk diameter d_0). The choice of the value of aspect ratio α/β plays important role in our model. Increasing of the aspect ratio of the landing cells (rectangles) leads to the formation of domains of increased regularity. The chosen value of $\alpha/\beta = 8$ is large enough to provide patterned substrate that is significantly different from the surfaces in the case with the square cells. We have verified that usage of a different, but large, values of aspect ratio α/β gives quantitatively very similar results leading to qualitatively same phenomenology.

To characterize the jammed state we studied radial distribution function $g(r)$ and probability distribution $P(v)$ of pore volume v for different values of density of landing cells: $\theta_0^{(\text{cell})} = 0.1, 0.2, 0.3, 0.4, 0.45$. Figure 11 shows the corresponding results for radial distribution function $g(r)$. Comparing the results from figures 7(b)–(d) and 11, one can see that the first peak near $r/d_0 = 1$ and local maximum at $r/d_0 \gtrsim 2$ of $g(r)$ are more pronounced in the case of elongated rectangular cells than in the case of multi-particle adsorption (MPCA) at squares. This emergence of a better local order is a correlation effect that develops during the deposition stage, due to the formation of arrays of disks along a single elongated rectangular cells.

Figure 12 compares volume distribution of the pores $P(v)$ for jamming coverings corresponding to different densities $\theta_0^{(\text{cell})}$. Similar to the case of MPCA on square cells,

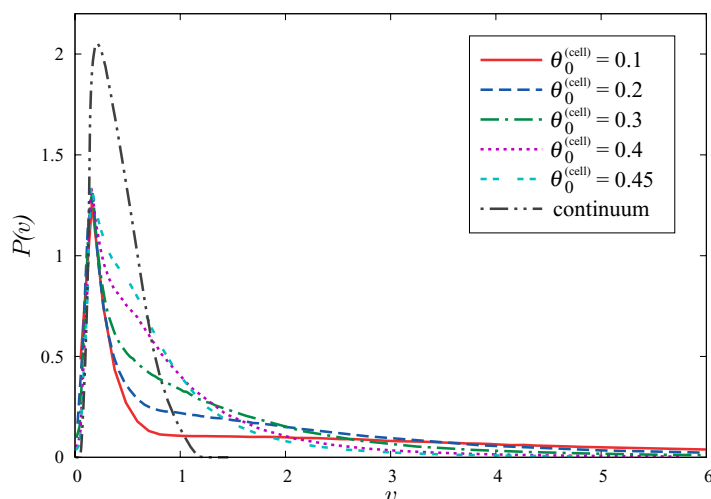


Figure 12. Volume distribution of the pores $P(v)$ obtained from simulations carried out using the heterogeneous surface covered by rectangles of arbitrary orientation. The curves correspond to various values of density $\theta_0^{(\text{cell})} = 0.1, 0.2, 0.3, 0.4, 0.45$, as indicated in the legend. Distribution $P(v)$ for jamming covering in the case of the irreversible disks deposition on a continuous substrate is shown for comparison.

here we observe the peak of $P(v)$ at small values of $v \approx 0.2$. As previously mentioned, such small pores are feature of coverings which occurs when three or more particles can be adsorbed on a single cell. The observed peak of the distribution $P(v)$ broadens when density $\theta_0^{(\text{cell})}$ increases. Deposition of elongated objects at high densities is characterized with compact domains of parallel objects and large islands of unoccupied substrate area. Figure 13 shows typical snapshot of the jammed-state covering obtained for rectangular cells of arbitrary orientation and density $\theta_0^{(\text{cell})} = 0.45$. Relatively high local packing of nearly parallel adsorbed rectangles reduces the number of disks effectively adsorbed at a cell. This process is associated with the appearance of larger interstitial voids, which causes the peak broadening.

It is now useful to explore the interplay between the anisotropy in deposition procedure for landing cells and structural characteristics of jamming coverings. In this case the orientation of rectangular cells is fixed to the one preferential direction. The configuration formed in the long time regime is made up of a large number of domains; see figure 14 for typical configuration. As expected, any such domain contains parallel cells all close to each other. This produces better packing of landing cells and higher impact of the cell-cell excluded volume interaction on the average cell population. Hence, anisotropic deposition of landing cells lowers the average cell population, which enhances the appearance of larger pores, resulting in a peak broadening. Volume distributions of pores $P(v)$ for jamming coverings of disks corresponding to anisotropic deposition of cells are shown in figure 15 with thick lines, while the case of arbitrarily oriented cells from figure 12 is drawn with thin lines for comparison. Figure 15 clearly shows enhanced peak broadening of $P(v)$ in the case of anisotropic deposition of landing cells, which is consistent with previous discussion.

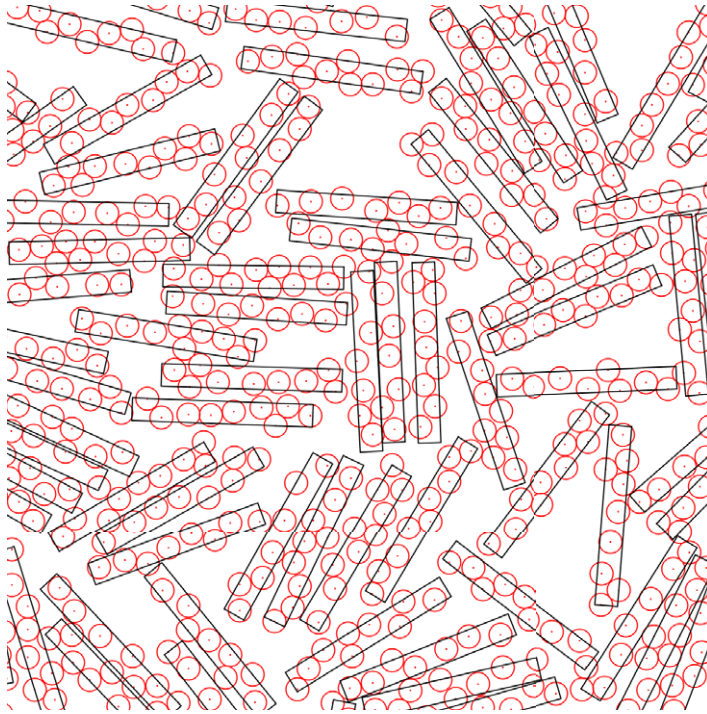


Figure 13. Typical jammed-state configuration of a region of size 30×30 (in units of the disk diameter d_0), for $\theta_0^{(\text{cell})} = 0.45$. Orientation of rectangular cells with sides $\alpha = 8$ and $\beta = 1$ is arbitrary. Deposition of elongated objects (cells) is characterized with domains of nearly parallel objects and large islands of unoccupied space.

4. Concluding remarks

We investigated numerically RSA of disk-shaped particles on a nonuniform substrates, with focus on the jammed-state properties. A surface heterogeneities consisting of square cells and elongated rectangles were considered. The influence of the cell size and density of landing cells on kinetics of deposition process, and on morphological characteristics of the coverings were studied.

We found that for a given density of landing cells, the highest jamming coverage and the fastest kinetics of the deposition process can be achieved in the SPCA case. Due to the fact that the densification kinetics is dictated by geometric exclusion effects, the coverage kinetics is severely slowed down in the MPCA case.

To examine the short scale structure in the jammed-state coverings, we evaluated the radial correlation function $g(r)$ which measures the particle density-density correlation at distance r for various shapes and sizes of the landing cells. The oscillation of $g(r)$ quickly decays for all densities of landing cells $\theta_0^{(\text{cell})}$, which means that long-range order does not exist in the system. In the MPCA case, the peak of $g(r)$ which appears at unit distance is the most pronounced for low densities of landing cells $\theta_0^{(\text{cell})}$. This is opposite to what is observed under SPCA conditions when the shape of radial distribution $g(r)$ is more structured at higher densities $\theta_0^{(\text{cell})}$.



Figure 14. Typical jammed-state configuration of a region of size 30×30 (in units of the disk diameter d_0 ,) for $\theta_0^{(\text{cell})} = 0.45$. Orientation of rectangular cells with sides $\alpha = 8$ and $\beta = 1$ is fixed to the horizontal direction.

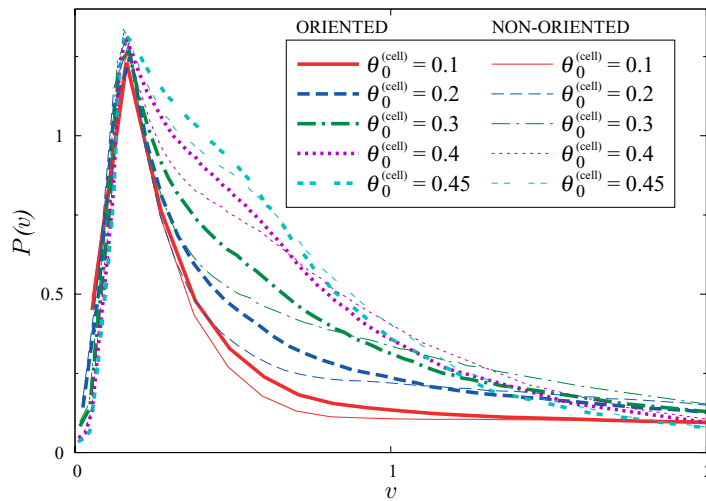


Figure 15. Volume distribution of the pores $P(v)$ obtained from simulations carried out using the heterogeneous surface covered by rectangles of fixed orientation (thick lines) and arbitrary orientations (thin lines). The curves correspond to various values of density $\theta_0^{(\text{cell})} = 0.1, 0.2, 0.3, 0.4, 0.45$, as indicated in the legend.

Morphology of deposited disks has also been analyzed through the distribution of pore volumes. This distribution is sensitive to small structural changes of the covering and therefore describes the degree to which the cell size and cell density affects the deposit

morphology. Delaunay ‘free’ volumes have a distribution with a long tail, particularly at low densities $\theta_0^{(\text{cell})}$. We have found that the distribution $P(v)$ becomes narrower and more localized around the low values of v with increasing of $\theta_0^{(\text{cell})}$. In the case of the largest cells ($\alpha \geq \alpha_4 = \sqrt{2}$), we have observed the pronounced peak of $P(v)$ at low values of $v = 0.15$ – 0.20 , which appears due to presence of configurations with three or more disks on a single landing cell. We have also studied the influence of a regular substrate pattern on volume distribution of the pores $P(v)$. At low densities $\theta_0^{(\text{cell})}$, distribution function $P(v)$ shows a well developed peaks which correspond to the various types of Delaunay triangles, as shown in figure 10. Cell–cell excluded volume interaction increases with the cell density $\theta_0^{(\text{cell})}$, so that distribution $P(v)$ for regular substrate pattern of squares becomes similar to $P(v)$ for random pattern case at densities near jamming limit for RSA of square cells.

Numerical simulations of random deposition on heterogeneous substrates covered by elongated rectangles have shown that the shape of the pore distribution function $P(v)$ is affected by the anisotropy in deposition procedure for landing cells. It is shown that anisotropic deposition of landing cells lowers the average cell population and reduces the number of small pores. Our results suggest that the porosity of deposit (pore volumes) can be controlled by the size and shape of landing cells, and by anisotropy of cell deposition procedure. It must be emphasized that radial correlation function $g(r)$ for jamming coverings of disks corresponding to anisotropic deposition of rectangles is quite similar to $g(r)$ for the case of isotropic landing-cell pattern and is not detailed here.

Acknowledgments

This work was supported by the Ministry of Education, Science and Technological Development of the Republic of Serbia, under Grant No. ON171017. Work at TAMUQ was supported by NPRP grant #6-021-1-005 and from the Qatar National Research Fund (a member of Qatar Foundation).

References

- [1] Parisse P, Luciani D, D’Angelo A, Santucci S, Zuppella P, Tucceri P, Reale A and Ottaviano L 2009 Patterning at the nanoscale: atomic force microscopy and extreme ultraviolet interference lithography *Mater. Sci. Eng. B* **165** 227–30
- [2] Kraus T, Malaquin L, Schmid H, Riess W, Spencer N D and Wolf H 2007 Nanoparticle printing with single-particle resolution *Nat. Nanotechnol.* **2** 570–6
- [3] Kershner R J *et al* 2009 Placement and orientation of individual dna shapes on lithographically patterned surfaces *Nat. Nanotechnol.* **4** 557–61
- [4] delCampo A, Greiner C, Àlvarez I and Arzt E 2007 Patterned surfaces with pillars with controlled 3d tip geometry mimicking bioattachment devices *Adv. Mater.* **19** 1973–7
- [5] Flory P J 1939 Intramolecular reaction between neighboring substituents of vinyl polymers *J. Am. Chem. Soc.* **61** 1518
- [6] Evans J W 1993 Random and cooperative sequential adsorption *Rev. Mod. Phys.* **65** 1281–329
- [7] Privman V 2000 Dynamics of nonequilibrium deposition *Colloids Surf. A* **165** 231–40
- [8] Talbot J, Tarjus G, Van Tassel P R and Viot P 2000 From car parking to protein adsorption: an overview of sequential adsorption processes *Colloids Surf. A* **165** 287–324

- [9] Senger B, Voegel J C and Schaaf P 2000 Irreversible adsorption of colloidal particles on solid substrates *Colloids Surf. A* **165** 255–85
- [10] Cadilhe A, Araújo N A M and Privman V 2007 Random sequential adsorption: from continuum to lattice and pre-patterned substrates *J. Phys.: Condens. Matter* **19** 065124
- [11] Jin X, Wang N H L, Tarjus G and Talbot J 1993 Irreversible adsorption on non-uniform surfaces: the random site model *J. Chem. Phys.* **97** 4256
- [12] Jin X, Talbot J and Wang N H L 1994 Analysis of steric hindrance effects on adsorption kinetics and equilibria *AIChE J.* **40** 1685
- [13] Oleyar C and Talbot J 2007 Reversible adsorption on random site surface *Physica A* **376** 27–37
- [14] Adamczyk Z, Weronki P and Musial E 2002 Irreversible adsorption of hard spheres at random site (heterogeneous) surfaces *J. Chem. Phys.* **116** 4665
- [15] Adamczyk Z, Siwek B, Weronki P and Musial E 2002 Irreversible adsorption of colloid particles at heterogeneous surfaces *Appl. Surf. Sci.* **196** 250
- [16] Marques J F, Lima A B, Araújo N A M and Cadilhe A 2012 Effect of particle polydispersity on the irreversible adsorption of fine particles on patterned substrates *Phys. Rev. E* **85** 061122
- [17] Araújo N A M, Cadilhe A and Privman V 2008 Morphology of fine-particle monolayers deposited on nanopatterned substrates *Phys. Rev. E* **77** 031603
- [18] Aurenhammer F 1991 Voronoi diagrams: a survey of a fundamental geometric data structure *ACM Comput. Surv.* **23** 345
- [19] Philippe P and Bideau D 2001 Numerical model for granular compaction under vertical tapping *Phys. Rev. E* **63** 051304
- [20] Richard P, Philippe P, Barbe F, Bourles S, Thibault X and Bideau D 2003 Analysis by x-ray microtomography of a granular packing undergoing compaction *Phys. Rev. E* **68** 020301
- [21] Aste T 2005 Variations around disordered close packing *J. Phys.: Condens. Matter* **17** S2361–90
- [22] Aste T 2006 Volume fluctuations and geometrical constraints in granular packs *Phys. Rev. Lett.* **96** 018002
- [23] Arsenović D, Vrhovac S B, Jakšić Z M, Budinski-Petković Lj and Belić A 2006 Simulation study of granular compaction dynamics under vertical tapping *Phys. Rev. E* **74** 061302
- [24] Truskett T M, Torquato S, Sastry S, Debenedetti P G and Stillinger F H 1998 Structural precursor to freezing in the hard-disk and hard-sphere systems *Phys. Rev. E* **58** 3083–8
- [25] Feder J 1980 Random sequential adsorption *J. Theor. Biol.* **87** 237
- [26] Swendsen R 1981 Dynamics of random sequential adsorption *Phys. Rev. A* **24** 504
- [27] Pomeau Y 1980 Some asymptotic estimates in the random parking problem *J. Phys. A: Math. Gen.* **13** L193
- [28] Bonnier B 2001 Random sequential adsorption of binary mixtures on a line *Phys. Rev. E* **64** 066111
- [29] Burrige D J and Mao Y 2004 Recursive approach to random sequential adsorption *Phys. Rev. E* **69** 037102
- [30] Hinrichsen E L, Feder J and Jøssang T 1986 Geometry of random sequential adsorption *J. Stat. Phys.* **44** 793–827
- [31] Bartelt M C and Privman V 1990 Kinetics of irreversible multilayer adsorption: one-dimensional models *J. Chem. Phys.* **93** 6820
- [32] Nielaba P, Privman V and Wang J S 1990 *J. Phys. A: Math. Gen.* **23** L1187
- [33] Manna S S and Švrakić N M 1991 Random sequential adsorption: line segments on the square lattice *J. Phys. A: Math. Gen.* **24** L671–6
- [34] Budinski-Petković Lj and Kozmidis-Luburić U 1997 Random sequential adsorption on a triangular lattice *Phys. Rev. E* **56** 6904
- [35] Budinski-Petković Lj and Kozmidis-Luburić U 1997 Jamming configurations for irreversible deposition on a square lattice *Physica A* **236** 211–9
- [36] Budinski-Petković Lj, Vrhovac S B and Lončarević I 2008 Random sequential adsorption of polydisperse mixtures on discrete substrates *Phys. Rev. E* **78** 061603
- [37] Barber C B, Dobkin D P and Huhdanpaa H 1996 The quickhull algorithm for convex hulls *ACM Trans. Math. Softw.* **22** 469



Response properties in the adsorption–desorption model on a triangular lattice



J.R. Šćepanović^a, D. Stojiljković^a, Z.M. Jakšić^a, Lj. Budinski-Petković^b,
S.B. Vrhovac^{a,*}

^a Scientific Computing Laboratory, Institute of Physics Belgrade, University of Belgrade, Pregrevice 118, Zemun 11080, Belgrade, Serbia

^b Faculty of Engineering, University of Novi Sad, Trg D. Obradovića 6, Novi Sad 21000, Serbia

HIGHLIGHTS

- Reversible RSA of objects of various shapes on a 2D triangular lattice is studied.
- We study the response of the model to an abrupt change in desorption probability.
- Short-time response strongly depends on the symmetry properties of the shapes.
- Density correlations decay slower for more symmetrical shapes.
- We observe the weakening of correlation features in multicomponent systems.

ARTICLE INFO

Article history:

Received 23 August 2015

Received in revised form 18 December 2015

Available online 2 February 2016

Keywords:

Random sequential adsorption

Desorption

Short-term memory effects

Triangular lattice

ABSTRACT

The out-of-equilibrium dynamical processes during the reversible random sequential adsorption (RSA) of objects of various shapes on a two-dimensional triangular lattice are studied numerically by means of Monte Carlo simulations. We focused on the influence of the order of symmetry axis of the shape on the response of the reversible RSA model to sudden perturbations of the desorption probability P_d . We provide a detailed discussion of the significance of collective events for governing the time coverage behavior of shapes with different rotational symmetries. We calculate the two-time density–density correlation function $C(t, t_w)$ for various waiting times t_w and show that longer memory of the initial state persists for the more symmetrical shapes. Our model displays nonequilibrium dynamical effects such as aging. We find that the correlation function $C(t, t_w)$ for all objects scales as a function of single variable $\ln(t_w)/\ln(t)$. We also study the short-term memory effects in two-component mixtures of extended objects and give a detailed analysis of the contribution to the densification kinetics coming from each mixture component. We observe the weakening of correlation features for the deposition processes in multicomponent systems.

© 2016 Elsevier B.V. All rights reserved.

1. Introduction

The understanding of random sequential adsorption (RSA) model has attracted large attention as a paradigmatic approach towards irreversibility, as well as due to the strong departure of the process from equilibrium behavior. In the RSA model [1], particles are added randomly and sequentially onto a substrate without overlapping each other. RSA model assumes that

* Corresponding author.

E-mail address: vrhovac@ipb.ac.rs (S.B. Vrhovac).

URL: <http://www.ipb.ac.rs/~vrhovac/> (S.B. Vrhovac).

deposited particles can neither diffuse along, nor desorb from the surface. The kinetic properties of a deposition process are described by the time evolution of the coverage $\theta(t)$, which is the fraction of the substrate area covered by the adsorbed particles. Within a monolayer deposit, each adsorbed particle affects the geometry of all later placements. Due to the blocking of the substrate area, at large times the coverage approaches the jammed-state value θ_j , where only gaps too small to fit new particles are left in the monolayer.

In pursuit of understanding the various aspects of the adsorption phenomenon large number of studies have taken place. A comprehensive survey on RSA and cooperative sequential adsorptions is given by Evans [2]. Other surveys include Privman [3–5], Cadihne et al. [4], Senger et al. [6], and Talbot et al. [7].

In many real physical situations it is necessary to consider the possibility of desorption of deposited particles [8–10]. Adsorption–desorption processes are important in the binding of ions to a Langmuir monolayer [11], and in many catalytic reactions. Binding and unbinding of kinesin motors to microtubules [12], of myosin to actin filaments, and of proteins to DNA are commonly studied biological examples. Possibility of desorption makes the process reversible and the system ultimately reaches an equilibrium state when the rate of desorption events balances the rate of adsorption events. The kinetics of the reversible RSA is governed by the ratio of adsorption to desorption rate, $K = k_+/k_-$. For large values of K , there is a rapid approach to density $\theta \simeq \theta_j$, followed by a slow relaxation to a higher steady-state value θ_∞ [13–16].

The reversible RSA model is frequently used by many authors to reproduce qualitatively the densification kinetics and other features of weakly vibrated granular materials [9,17,10]. The phenomenon of granular compaction involves the increase of the density of a granular medium subjected to shaking or tapping [18–23]. The relaxation dynamics is extremely slow, taking many thousands of taps to approach the steady state, and it slows down for lower vibration intensities. The final steady-state density is a decreasing function of the vibration intensity [23]. Dynamics of the reversible RSA model depends on the excluded volume and geometrical frustration, just as in the case of granular compaction. This model can be regarded as a simple picture of a horizontal layer of a granular material, perpendicular to the tapping force. As a result of a tapping event, particles leave the layer at random and compaction proceeds when particles fall back into the layer under the influence of gravity. The ratio of desorption to adsorption rate $1/K = k_-/k_+$ within the model plays a role similar to the vibration intensity Γ in real experiments [24] (Γ is defined as the ratio of the peak acceleration of the tap to the gravitational acceleration g).

One of the striking features of granular materials are the memory effects observed by measuring the short-time response to an instantaneous change in the tapping acceleration Γ [25]. For a sudden decrease in Γ it was observed that on short-time scales the compaction rate increases, while for a sudden increase in Γ the system dilates for short times. This behavior is transient and after several taps there is a crossover to the “normal” behavior, with the relaxation rate becoming the same as in constant vibration intensity mode. Furthermore, Nicolas et al. [26] have also shown that periodic shear compaction exhibits a nontrivial response to a sudden change in shear amplitude. The rapid variation of volume fraction induced by the sudden change of shear angle is proportional and opposite to the angle change. The short-term memory effects observed in granular materials are reflected in the fact that the future evolution of the packing fraction θ after time t_w depends not only on the $\theta(t_w)$, but also on the previous tapping history. It is important to note that the parking lot model (PLM, 1D off-lattice reversible RSA model) [24,9,27,17] is a widely used model which can reproduce qualitatively the short-term memory effects of a weakly vibrated granular material. In Ref. [10] we have presented the detailed studies of the short-term memory effects in the framework of a two-dimensional reversible RSA model on a square lattice.

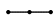


An important issue in two-dimensional deposition is the influence of the shape of the adsorbed particle. It is well known that the size, aspect ratio and symmetry properties of the object have a significant role in the processes of both irreversible and reversible deposition. The numerical analyses for the irreversible deposition of various shapes and their mixtures on a triangular lattice [28,29] establish that the approach to the jamming limit follows the exponential law with the rate dependent mostly on the order of symmetry axis of the shape. In the reversible case of deposition on a triangular lattice [15,30], we have found that the coverage kinetics is severely slowed down with the increase of the order of symmetry of the shape.

The main goal of the present study is to investigate the interplay between the response of the reversible RSA model to sudden perturbations of the desorption probability P_d and the symmetry properties of deposited shapes. Numerical simulations of adsorption–desorption processes are performed for various shapes on the triangular lattice, shown in Table 1. These shapes are made of self-avoiding walks of the same length $\ell = 2$, but they differ in their symmetry properties. The response in the evolution of the density $\theta(t)$ to a change in the desorption probability P_d at a given time t_w is accompanied by transformation of the local configurations in the covering. Essentially, collective (two-particle) events are responsible for the evolution of θ for $\theta > \theta_j$. Size of the objects and their symmetry properties have a significant influence on these collective events, thus affecting the kinetics of the deposition process [15,31,30]. Since we focus our interest on the influence of symmetry of the object on the response of the system to sudden perturbation of the desorption probability P_d , it is necessary to analyze the processes with the objects of the same size. In this paper we also study the response of two-component mixtures of extended objects (see, Table 1) to sudden perturbations of the desorption probability P_d . We did carry out a detailed analysis of the contribution to the densification kinetics coming from each mixture component. Finally, we study the nonequilibrium two-time density–density correlation function $C(t, t_w)$. We focus, in particular, on the influence of symmetry properties of the shapes on the decay of $C(t, t_w)$ and aging effects. This work provides for the first time the link between the short-term memory effects and intrinsic properties of the shapes.

Recently, we have analyzed the growth of the coverage $\theta(t)$ above the jamming limit to its steady-state value θ_∞ within the framework of the adsorption–desorption model of dimers in one dimension [32]. We reported a numerical evidence

Table 1

Various shapes (x) of length $\ell^{(x)} = 2$ on a triangular lattice. Here $n_s^{(x)}$ denotes the order of the symmetry axis of the shape (x), $s^{(x)}$ is the object size, and $\theta_j^{(x)}$ is the jamming coverage. The numbers in parentheses are the numerical values of the standard uncertainty of $\theta_j^{(x)}$ referred to the last digits of the quoted value.

(x)	Shape	$n_s^{(x)}$	$s^{(x)}$	$\ell^{(x)}$	$\theta_j^{(x)}$
(A)		2	2		0.8362(4)
(B)		1	1.5	2	0.8345(5)
(C)		3	1		0.7970(4)

that the time needed for a system to reach the given coverage θ can be significantly reduced if P_d decreases both stepwise and linearly (continuously) over a certain time domain. Based on the results in the present paper, one would expect that the growth of the coverage in the case of the two-dimensional reversible RSA model can also be accelerated by decreasing the desorption rate during the deposition process. However, our results indicate that the efficiency of this process depends on the symmetry properties of the deposited objects. This must be taken into account when developing an optimal protocol which significantly hastens the process for achieving high coverage densities.

The paper is organized as follows. Section 2 describes the details of the simulations. We give the simulation results and discussions in Section 3. Finally, Section 4 contains some additional comments and final remarks.

2. Definition of the model and numerical simulation

The depositing shapes are modeled by directed self-avoiding walks on a triangular lattice. A self-avoiding shape of length ℓ is a sequence of distinct vertices $(\omega_0, \dots, \omega_\ell)$ such that each vertex is a nearest neighbor of its predecessor. Consequently, a walk of length ℓ covers $\ell + 1$ lattice sites. On a triangular lattice objects with a symmetry axis of first, second, third, and sixth order can be formed. Rotational symmetry of order n_s , also called n -fold rotational symmetry, with respect to a particular axis perpendicular to the triangular lattice, means that rotation by an angle of $2\pi/n_s$ does not change the object. In Table 1 three different shapes that can be made by self-avoiding walks of length $\ell = 2$ are shown. It should be noted that size s of an object is taken as the greatest projection of the walk that makes the object on one of the six directions. Thus the size of a dot is $s = 0$, the size of a one-step walk is $s = 1$, and for example the size of the second object (B) in Table 1 is $s = 1.5$ in lattice spacing.

The Monte Carlo simulations are performed on a triangular lattice of size $L^2 = 120 \times 120$. At each Monte Carlo step adsorption is attempted with probability P_a and desorption with probability P_d . In the simulations of deposition processes with desorption, the kinetics is governed by the desorption to adsorption probability ratio $\Gamma = P_d/P_a$ [33,34]. Since we are interested in the ratio Γ , in order to save computer time, it is convenient to take the adsorption probability to be $P_a = 1$, i.e., to try an adsorption at each Monte Carlo step.

We start with an initially empty triangular lattice. Adsorption and desorption processes perform simultaneously with corresponding probabilities. For each of these processes, a lattice site is chosen at random. In the case of adsorption, we attempt to place the object with the beginning at the selected site. If the selected site is unoccupied, one of the six possible orientations is chosen at random and deposition of the object is tried in that direction. We fix the beginning of the walk that makes the shape of length ℓ at the selected site and search whether all successive ℓ sites are unoccupied. If they are empty, we occupy these $\ell + 1$ sites and place the object. If, however, any of the ℓ sites are already occupied, the deposition attempt is rejected and the configuration remains unchanged. This scheme is usually called conventional or standard model of deposition. The other strategy to perform an RSA, where we check all possible directions from the selected site, is named the end-on model [28]. On the other hand, if the attempted process is desorption and if the selected site is already occupied by a previously adsorbed object, the object is removed with probability P_d from the layer.

Adsorption–desorption processes on discrete substrates display a surprisingly complex kinetics [9,35]. Here we consider the case of rapid adsorption and slow desorption ($\Gamma = P_d/P_a \ll 1$). Then there exist two time scales controlling the evolution of the coverage $\theta(t)$. The first stage of the process is dominated by adsorption events and the kinetics displays an RSA-like behavior. With the growth of the coverage the desorption process becomes more and more important. Increasing the coverage over the jamming limit is possible only due to the collective rearrangement of the adsorbed particles in order to open a hole large enough for the adsorption of an additional particle. We are interested in the approach to the equilibrium coverage in this later, post-jamming time range.

Periodic boundary conditions are used in all directions. The time t is counted by the number of adsorption attempts and scaled by the total number of lattice sites L^2 . The data are averaged over 10^3 independent runs for each shape and each desorption probability. The finite-size effects, which are generally weak, can be neglected for object sizes $< L/8$ [36].

Furthermore, during the simulation of irreversible deposition we record the number of inaccessible sites in the lattice. A site is inaccessible if it is occupied or it cannot be the beginning of the shape. The jamming limit θ_j is reached when the number of inaccessible sites is equal to the total number of lattice sites. Values of jamming coverages $\theta_j^{(x)}$ for three objects (x) $\in \{(A), (B), (C)\}$ of length $\ell = 2$ are given in Table 1. Fig. 1 shows a typical snapshot configuration at coverage fraction $\theta = 0.89$ obtained in the case of $P_d = 0.0045$ for line-segments of length $\ell = 2$ (object (A) from Table 1).

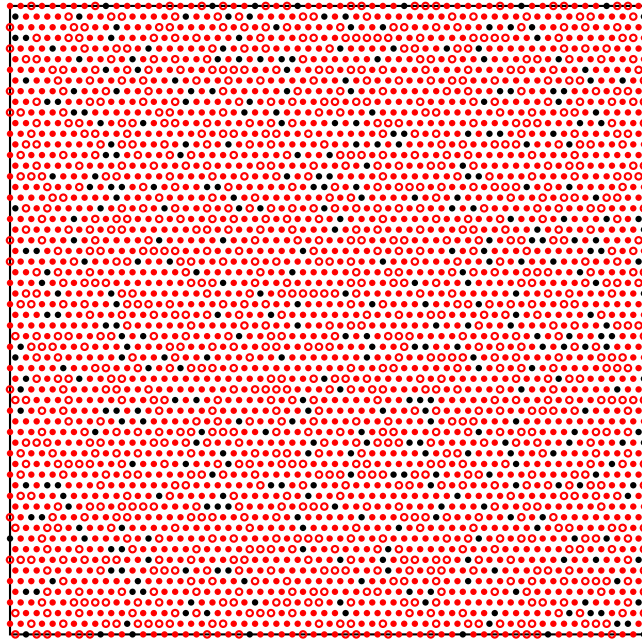


Fig. 1. Snapshot of pattern formed during the reversible deposition of object (A) from Table 1 correspond to coverage fraction $\theta = 0.89$, and $P_d = 0.0045$. Nodes of the grid corresponding to the beginning of the walk that makes the shape are indicated by large open points. Empty nodes are marked with black points. A lattice of size $L^2 = 60 \times 60$ is used.

3. Results and discussion

In order to analyze the response of the reversible RSA model to sudden perturbations of the desorption probability P_d , we have carried out series of Monte Carlo simulations for objects (A), (B), and (C), all of them starting from an empty lattice. The system was evolved at a fixed desorption probability $P_d^{(1)}$. At a certain time, t_w , the value of the desorption probability $P_d^{(1)}$ was instantaneously changed to another value $P_d^{(2)}$. The variations of coverage $\theta(t)$ in the case of object (A), for three different values of t_w are reported in Fig. 2. It must be emphasized that the same kind of numerical experiments for objects (B) and (C) produce qualitatively similar results for the time evolution of the coverage $\theta(t)$. First, in Fig. 2 we show the response of the system to the desorption probability shift from $P_d^{(1)} = 0.0045$ to $P_d^{(2)} = 0.0015$ at the times $t_w = 139, 205, 307$ needed for a system to reach the coverages $\theta_w = 0.87, 0.88, 0.89$, respectively, in the process of reversible RSA with $P_d^{(1)} = 0.0045$. As it can be seen, when $P_d^{(1)} > P_d^{(2)}$, the compaction rate of the perturbed system first increases on short-time scales. After a transient, compaction slows down and the rate of compaction crosses over to the one observed at constant desorption probability $P_d^{(2)}$.

Fig. 2 also shows typical response of the system at short times after an abrupt change of the desorption probability from $P_d^{(1)} = 0.0015$ to $P_d^{(2)} = 0.0045$ at the times $t_w = 304, 441, 639$ needed for a system to reach the coverages $\theta_w = 0.87, 0.88, 0.89$, respectively, in the process of reversible RSA with $P_d^{(1)} = 0.0015$. For $P_d^{(1)} < P_d^{(2)}$ we find a short-term response of the system opposite to the previous case. First, as the desorption probability is increased, one observes a decompaction. Later on, the larger desorption probability $P_d^{(2)}$ begins to prevail and the compaction proceeds faster, at the normal rate for constant $P_d^{(2)}$. In addition, the comparison (not shown here) of the density relaxations $\theta(t)$ at various changes in the desorption probability P_d indicates that the amplitude of the jump in the compaction rate is larger for larger jump of the desorption probability $\Delta P_d = |P_d^{(2)} - P_d^{(1)}|$. The probabilities of $P_d^{(1)} = 0.0015$ and $P_d^{(2)} = 0.0045$ are chosen to provide a wide density range $\theta \in (0.86, 0.89)$ for all three objects where desorption probability can be abruptly changed. We have verified that usage of different, but sufficiently small, values of desorption probabilities $P_d^{(1)}$ and $P_d^{(2)}$ gives quantitatively similar results leading to qualitatively same phenomenology.

This shows that the system has some memory of its history at t_w . Memory effect implies that the system can be found in states, characterized by the same coverage fraction θ , that evolve differently under further reversible deposition with the same desorption probability P_d [17]. This is illustrated in the inset of Fig. 2. The points M and N correspond to states with equal coverage fraction $\theta_c = 0.8686$, equal value of $P_d = 0.0045$, but different further evolution. Their responses to the same desorption probability P_d are different: covering M becomes looser whereas covering N pursues its compaction. In other words, the density evolution $\theta(t)$ after the points M and N depends not only on the density θ_c , but also on the previous tapping history. The memory of the history up to the density θ_c is encoded in the arrangement of the objects in the covering.

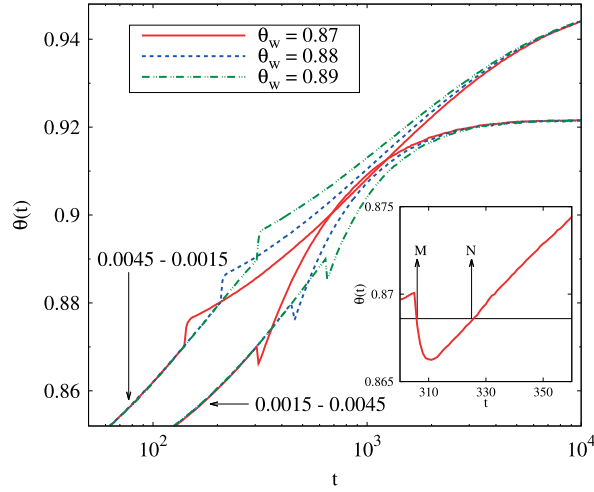


Fig. 2. Time evolution of the coverage $\theta(t)$ for object (A) when the desorption probability is changed from $P_d^{(1)} = 0.0045$ to $P_d^{(2)} = 0.0015$ (from $P_d^{(1)} = 0.0015$ to $P_d^{(2)} = 0.0045$) at times $t_w = 139, 205, 307$ ($t_w = 304, 441, 639$) needed for the system to reach the coverages $\theta_w = 0.87, 0.88, 0.89$, respectively, in the process of reversible RSA with $P_d^{(1)} = 0.0045$ ($P_d^{(1)} = 0.0015$). Inset: Zoom up on the region around $t_w = 304$ ($\theta(t_w) = 0.87$) when the desorption probability switches from $P_d^{(1)} = 0.0015$ to $P_d^{(2)} = 0.0045$. The points M and N correspond to states with equal density $\theta_c = 0.8686$, equal value of $P_d^{(2)} = 0.0045$, but different further evolution.

Interpretation of these results for all objects (A), (B), and (C) is quite straightforward using the results of Refs. [37,9, 34]. The compaction rate just before t_w is determined by the desorption probability $P_d(t_w - 0)$ and by the fraction of the substrate, $\Phi(t_w - 0)$, that is available for the insertion of a new particle. The quantity $\Phi(t_w - 0)$ (the insertion probability) strongly depends on the state of the system, but it is not unambiguously determined by the coverage fraction $\theta(t_w - 0)$ at the same instant [9,10]. When P_d is abruptly lowered, the first effect is that the particles tend to decrease the fraction of the substrate that is available for deposition of new particles, and the layer becomes more compact. Therefore the rate of compaction first increases with respect to the unperturbed case. At larger times, however, the compaction is slowed down by the creation of a denser substrate and smaller fraction of the layer that is available for the insertion of a new particle.

When the desorption probability P_d is suddenly increased at t_w , the first effect is decompaction. On short-time scales, the interplay between the insertion probability and desorption probability leads to the fast density changes. During this transient stage the fraction of the substrate that is available for the insertion of a new particle is an increasing function of time. After this transient interval, the adsorption events prevail, and the compaction proceeds faster. Growing of the insertion probability, $\Phi(t)$, during the transient time, leads to the more efficient densification afterwards.

Here we focus our interest on the influence of the order of symmetry axis of the shape on the response of the reversible RSA model to sudden perturbation of the desorption probability P_d . Consequently, we considered series of numerical experiments where the short-term memory effects were analyzed for the three systems. In this set of experiments the objects (A), (B), and (C) were deposited to the same density θ_w with desorption probability $P_d^{(1)}$. After the density θ_w was achieved, desorption probability P_d was switched from $P_d^{(1)}$ to $P_d^{(2)}$ ($P_d^{(2)} \leq P_d^{(1)}$). In Fig. 3 we show the time evolution of the density $\theta(t)$ during the deposition of objects (A), (B), and (C), when the desorption probability P_d is changed from $P_d^{(1)} = 0.0045$ to $P_d^{(2)} = 0.0015$. Here, the results for three different values of θ_w are reported, namely, 0.87, 0.88, and 0.89. The time origin for each experiment has been taken at the time when the system reached the prescribed density θ_w . In Fig. 4 the same set of numerical experiments is carried out, with the only difference that in this case the desorption probability is changed from $P_d^{(1)} = 0.0015$ to $P_d^{(2)} = 0.0045$. These simulations show that the short-time response to an instantaneous change in desorption probability P_d strongly depends on the symmetry properties of the shapes. From Figs. 3 and 4, it follows that the change in the compaction rate on short-time scales is less pronounced as order of symmetry axis of the shape n_s increases.

Qualitative interpretation of these results can be attained by exploiting the mechanism of collective events for governing the late-time changes in the coverage fraction ($\theta(t) > \theta_j$). In the following, we restrict ourselves to the case of weak desorption (large values of $K = P_a/P_d$), when the system of adsorbed particles evolves continuously toward an equilibrium disordered state. When a value of θ_j is reached, the rare desorption events are generally followed by immediate readsorption. The total number of particles is not changed by these *single* particle events. Essentially, collective events are responsible for the evolution of coverage fraction θ above the jamming limit θ_j . The rearrangement of state corresponding to $\theta > \theta_j$, to its steady-state value θ_∞ , is dominated by the following *two-particle* processes:

- (a) in one process (“2 \rightarrow 1”), responsible for decreasing the number of deposited objects by 1, two adjacent objects leave and a single one comes in their stead;

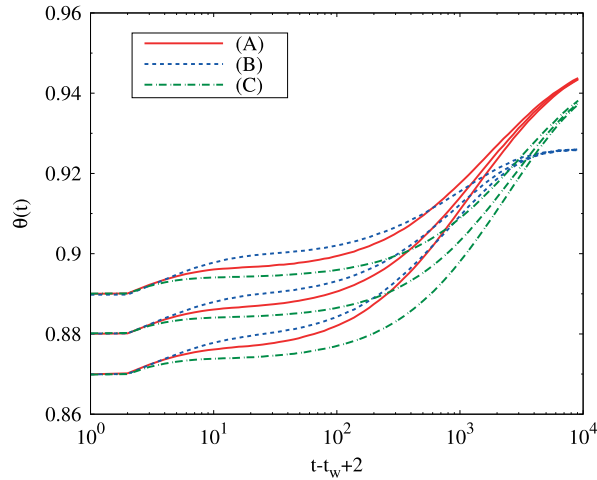


Fig. 3. Time evolution of the coverage $\theta(t)$ for objects (A), (B), and (C) when the desorption probability is changed from $P_d^{(1)} = 0.0045$ to $P_d^{(2)} = 0.0015$ at the times t_w needed for the system to reach the coverages $\theta_w = 0.87, 0.88, 0.89$ in the process of reversible RSA with $P_d^{(1)} = 0.0045$. The time origin for each experiment has been taken at the time when the system reached the prescribed density θ_w .

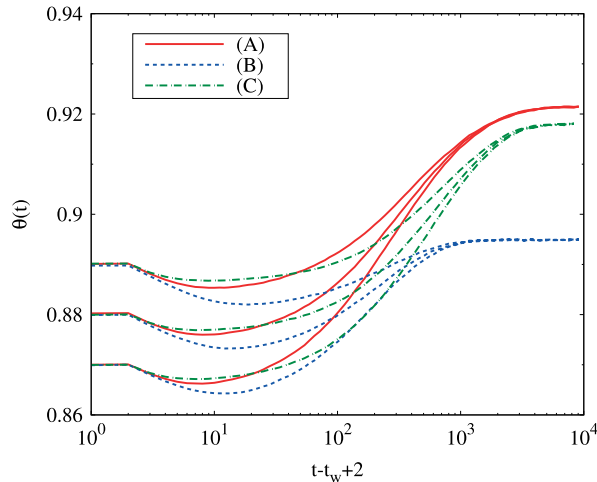


Fig. 4. Time evolution of the coverage $\theta(t)$ for objects (A), (B), and (C) when the desorption probability is changed from $P_d^{(1)} = 0.0015$ to $P_d^{(2)} = 0.0045$ at the times t_w needed for the system to reach the coverages $\theta_w = 0.87, 0.88, 0.89$ in the process of reversible RSA with $P_d^{(1)} = 0.0015$. The time origin for each experiment has been taken at the time when the system reached the prescribed density θ_w .

(b) the opposite process (“1 \rightarrow 2”) results in adding an extra object to the lattice: an object exits and leaves a space big enough for two objects.

The rate of the “2 \rightarrow 1” process has three contributions. First, an object must leave the lattice. Then, an adjacent object must leave before the hole left by the first object fills. Finally, the big hole must be blocked by a badly sited object. In the opposite, “1 \rightarrow 2” process, the void left by the object must be large enough for two objects. Note that the first incoming object must park with a sufficient precision in order to leave enough space for the second object.

It is obvious that the process “1 \rightarrow 2” has an overall rate proportional to P_d ($P_d < 1$). Since the process “2 \rightarrow 1” includes *two* consecutive desorption events, it is plausible that its overall rate is proportional to $(P_d)^2 < P_d < 1$. That is the main reason why, for coverages that are not close to the steady-state value, the collective event “1 \rightarrow 2” is more frequent than the opposite event “2 \rightarrow 1”. This regime persists until the coverage is very close to the equilibrium value. Since the coverage fraction $\theta(t)$ increases and the available surface function Φ decreases, the overall rate at which the density increases is progressively reduced. The efficiency of desorption relative to adsorption increases, and the process reaches a steady state in which the rate of the “2 \rightarrow 1” process is balanced by the “1 \rightarrow 2” process.

Note that in Ref. Kolan et al. [24], the authors calculated the transition rates for the collective processes “1 \rightleftharpoons 2” in the case of a 1D RSA model and found that these rates account for the additional slow time scales. Ghaskadvi and Dennin [11] directly monitored the transition rates for the two-particle processes “1 \rightleftharpoons 2” as part of the simulation. They have directly confirmed the importance of multiparticle transitions “1 \rightleftharpoons 2” for governing the late time behavior of the system.

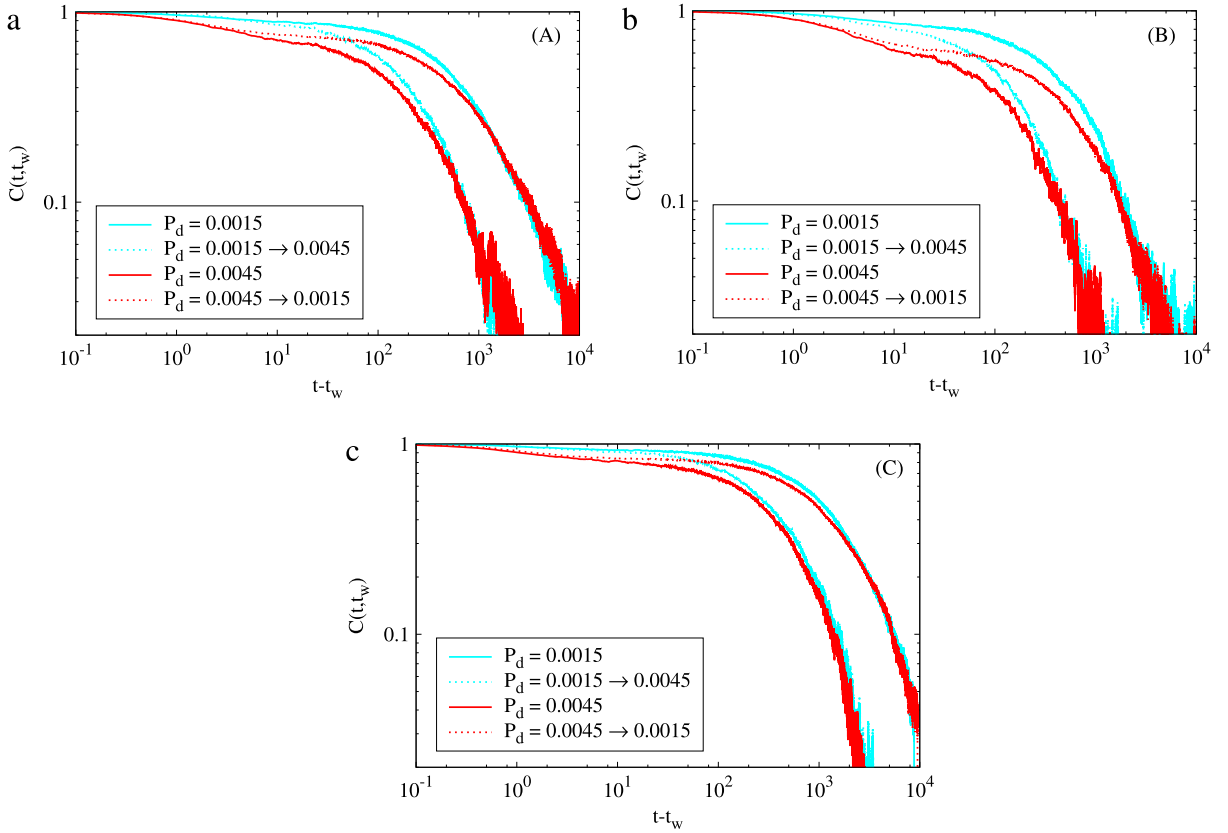


Fig. 5. Two-time density–density correlation function $C(t, t_w)$ for objects (a) (A), (b) (B), and (c) (C), as a function of $t - t_w$. The waiting time t_w corresponds to the time needed for the system to reach the coverage $\theta_w = 0.88$. The solid lines represent the temporal behavior of $C(t, t_w)$ obtained for the fixed desorption probabilities $P_d = 0.0015, 0.0045$, as indicated in the legend. The dashed lines represent the temporal dependence of $C(t, t_w)$ obtained from the runs during which an abrupt change of desorption probability $P_d^{(1)} = 0.0045 \rightarrow P_d^{(2)} = 0.0015$ ($P_d^{(1)} = 0.0015 \rightarrow P_d^{(2)} = 0.0045$) occurs at instant t_w , as indicated in the legend.

Now we try to explain how the order of symmetry axis of the shape changes the dynamics of the collective processes. Symmetry properties of the shapes have a significant influence on the filling of small isolated targets on the lattice. Indeed, there is only a restricted number of possible orientations in which an object can reach a previously opened location, provided the location is small enough. A shape with a symmetry axis of higher order has a greater number of possible orientations for deposition into small isolated locations on the lattice, and therefore enhanced probability of single-particle readsorption. This extends the mean waiting time between consecutive two-particle events “1 \rightarrow 2”, responsible for the density growth above θ_j , and causes a slowing down of the density growth. On the contrary, for the asymmetrical shapes (angled objects) there is a greater probability for blocking the neighboring sites. The noticeable drop in the probability of single-particle readsorption for the asymmetrical shapes is thus a clear consequence of the enhanced frustration of the spatial adsorption. Therefore, desorption process effectively opens holes that are large enough for insertion of two or more particles. This reduces the mean waiting time between consecutive multiparticle events which leads to more rapid growth of the density. When P_d is abruptly lowered, such a different object view is the cause of the enhanced density growth in the case of asymmetrical shapes as compared to those in the case of more round (symmetric) shapes. When the desorption probability P_d is suddenly increased, decompaction rate of the perturbed system on short-time scales is larger for shapes with a symmetry axis of lower order (Fig. 4). This is a consequence of the fact that unlike for the more symmetrical objects, much less orientations are allowed for irregular and asymmetric shapes falling in the isolated selective target spaces.

Below we try to further quantitatively characterize the out-of equilibrium dynamics in our system. Specifically, we have evaluated the two-time density–density correlation function, $C(t, t_w)$, and qualitatively analyzed its dependence on symmetry properties of the shapes. The normalized two-time density–density correlation function is defined as follows,

$$C(t, t_w) = \frac{\langle \theta(t)\theta(t_w) \rangle - \langle \theta(t) \rangle \langle \theta(t_w) \rangle}{\langle \theta^2(t_w) \rangle - \langle \theta(t_w) \rangle^2}, \quad t \geq t_w, \quad (1)$$

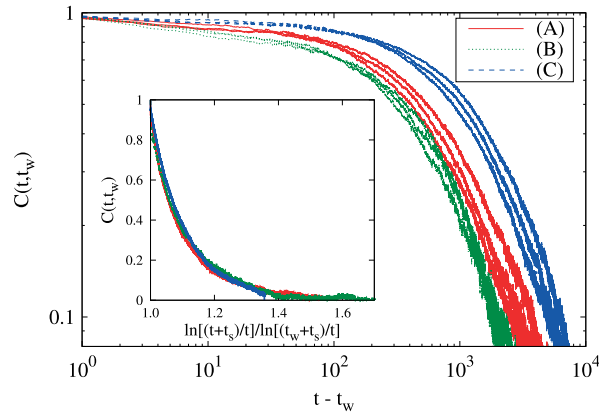


Fig. 6. Two-time density–density correlation function $C(t, t_w)$ for objects (A), (B), and (C), as a function of $t - t_w$. The waiting times t_w for each object correspond to the time needed for the system to reach the coverages $\theta_w = 0.87, 0.88, 0.89$ in the process of reversible RSA with $P_d = 0.0015$. The aging behavior is evident. Inset: The correlation $C(t, t_w)$ as a function of the scaling variable $\alpha = \ln[(t_0 + t_s)/\tau] / \ln[(t + t_s)/\tau]$. Fitting parameters are $t_s = 1760$, and $\tau(A) = 81, \tau(B) = 210, \tau(C) = 43$.

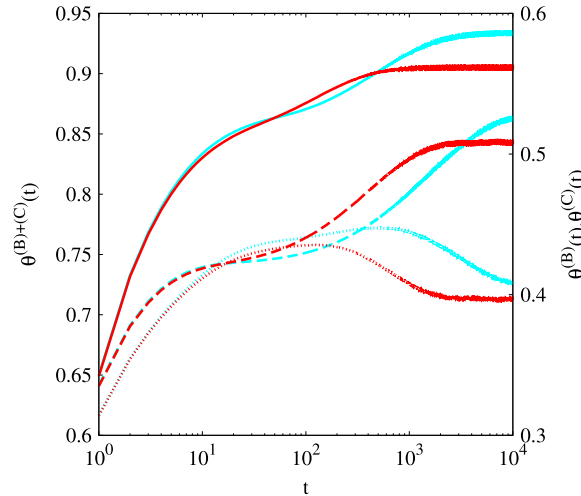


Fig. 7. Shown here is the time dependence of the coverage fraction $\theta^{(B)+(C)}$ for the mixture (B) + (C) and its components for two different values of desorption probability, $P_d = 0.0015, 0.0045$. Black (red) and grey (light blue) lines represent the results obtained for $P_d = 0.0045$ and $P_d = 0.0015$, respectively. The solid lines represent the temporal behavior of the coverage fraction $\theta^{(B)+(C)}(t)$ (left-hand axis). The dashed and dotted lines are plotted against the right-hand axis and give the coverage fraction versus time t of the component shapes (C), $\theta^{(C)}(t)$ (dashed), and (B), $\theta^{(B)}(t)$ (dotted). (For interpretation of the references to color in this figure legend, the reader is referred to the web version of this article.)

where the angular brackets $\langle \dots \rangle$ denote an average over independent runs. In order to obtain reasonable statistics, it is necessary to average over many independent runs (typically 10^4). Out of equilibrium, $C(t, t_w)$ is a function of both times, t and t_w .

In Fig. 5 we show the behavior of the correlation function $C(t, t_w)$ for objects (A), (B), and (C). The waiting time t_w corresponds to the time needed for a system to reach the coverage $\theta_w = 0.88$. Numerical simulations for other densities, $\theta_w = 0.87, 0.89$, produce qualitatively similar results for the time evolution of the correlation function $C(t, t_w)$. In each plot of Fig. 5, the temporal dependence of $C(t, t_w)$ is displayed for the fixed desorption probabilities, $P_d = 0.0015, 0.0045$. For comparison, we also show the temporal dependence of $C(t, t_w)$ calculated from 10^4 independent runs during which an abrupt change of desorption probability $P_d^{(1)} = 0.0045 \rightarrow P_d^{(2)} = 0.0015$ ($P_d^{(1)} = 0.0015 \rightarrow P_d^{(2)} = 0.0045$) occurs at instant t_w . Correlation function obtained from the numerical simulation in which there is an instantaneous change of desorption probability $P_d^{(1)} \rightarrow P_d^{(2)}$, interpolates between two correlation functions calculated for constant desorption probabilities $P_d^{(1)}$ and $P_d^{(2)}$. At short times, this correlation function behaves as $C(t, t_w)$ obtained in the case when the desorption probability has the constant value $P_d^{(1)} = 0.0045$ ($P_d^{(1)} = 0.0015$). However, its long time behavior is consistent with the decay of $C(t, t_w)$ obtained in the case when the desorption probability has the constant value $P_d^{(2)} = 0.0015$ ($P_d^{(2)} = 0.0045$). By comparing the three panels in Fig. 5, it is obvious that global properties of the correlation function $C(t, t_w)$ of the density fluctuations depend on the order of symmetry axis of the shape n_s : as n_s grows, the correlation decays slower. In

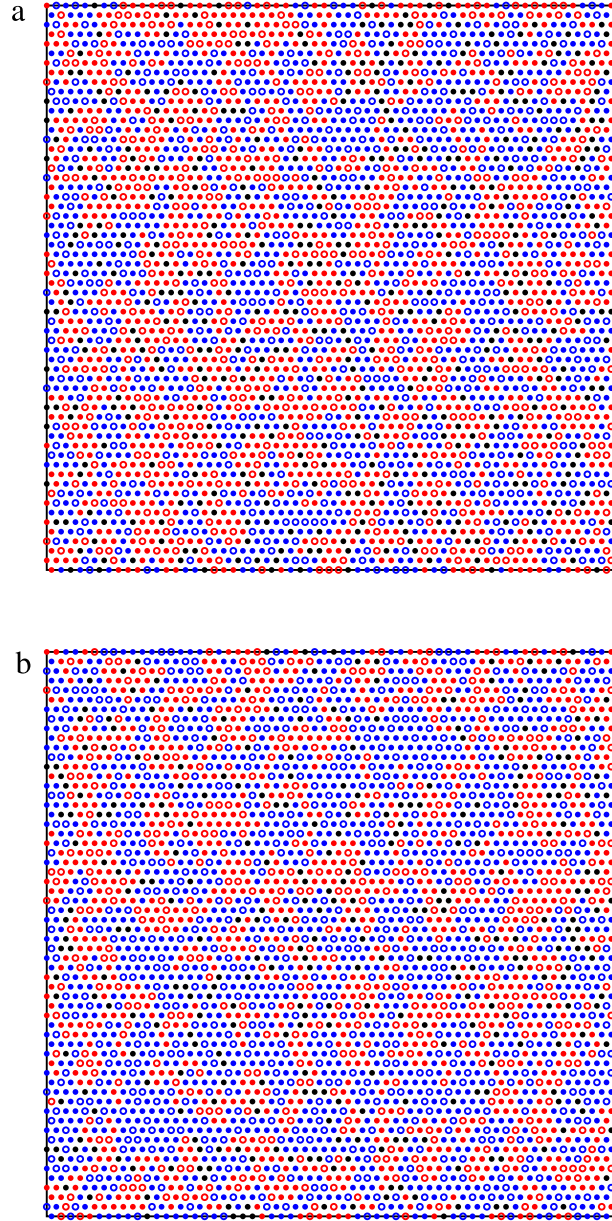


Fig. 8. Snapshot of pattern formed during the reversible deposition of mixture (B) + (C) ((B)-red, (C)-blue) from Table 1 correspond to (a) coverage fraction $\theta^{(B)+(C)} = 0.88$, and (b) steady-state coverage $\theta_{\infty}^{(B)+(C)} = 0.9066$. Nodes of the grid corresponding to the beginning of the walk that makes the shapes are indicated by large open points. Empty nodes are marked with black points. A lattice of size $L^2 = 60 \times 60$ and $P_d = 0.0045$ are used. (For interpretation of the references to color in this figure legend, the reader is referred to the web version of this article.)

other words, longer memory of the initial state persists for the more symmetrical shapes. Indeed, the increase of the order of symmetry of the shape enhances the rate of *single* particle readsorption. This extends the time needed for a system to forget the initial configuration. However, the correlation curves do not differ qualitatively and they have similar shapes for all objects.

It is well known that the aging properties of the system are characterized by specific scaling properties of $C(t, t_w)$. For example, in the Tetris and Ising frustrated lattice gas models, it was found that the relaxation of $C(t, t_w)$ is given by the form [38]:

$$C(t, t_w) = (1 - c_{\infty}) \frac{\ln[(t_w + t_s)/\tau]}{\ln[(t + t_s)/\tau]} + c_{\infty}, \quad (2)$$

where τ , t_s and c_{∞} are fitting parameters. The above behavior is found in our model. In Fig. 6 we show the behavior of the correlation function $C(t, t_w)$ for objects (A), (B), and (C), when $P_d = 0.0015$. The waiting times t_w correspond to the

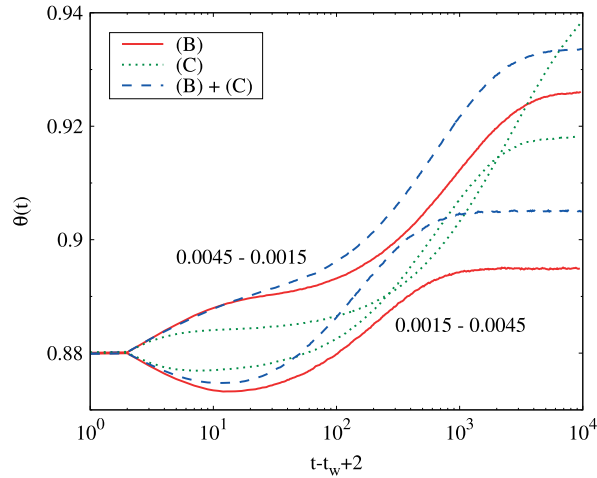


Fig. 9. Time evolution of coverage fraction $\theta^{(B)+(C)}$ for the mixture (B) + (C) when the desorption probability is changed from $P_d^{(1)} = 0.0045$ to $P_d^{(2)} = 0.0015$ (from $P_d^{(1)} = 0.0015$ to $P_d^{(2)} = 0.0045$) at the time $t_w = 126$ ($t_w = 182$) needed for the system to reach the coverage $\theta_w^{(B)+(C)} = 0.88$, in the process of reversible RSA with $P_d^{(1)} = 0.0045$ ($P_d^{(1)} = 0.0015$). The time origin for each experiment has been taken at the time when the system reached the prescribed density θ_w .

time needed for a system to reach the coverages $\theta_w = 0.87, 0.88, 0.89$. For all the shapes, the typical aging behavior is observed: the larger t_w , the longer memory of the initial state persists. The inset of Fig. 6 illustrates that when the two-time correlation function $C(t, t_w)$ is plotted as a function of $\ln[(t + t_s)/\tau]/\ln[(t_w + t_s)/\tau]$ the data for all three objects collapse onto single curve. This figure clearly demonstrates the existence of the single universal master function. It is interesting that the parameter t_s is equal for all objects, $t_s = 1760$. However, parameter τ depends on the shape: $\tau(A) = 81$, $\tau(B) = 210$, $\tau(C) = 43$. The shapes of higher order of symmetry n_s have lower values of scaling parameter τ .

3.1. Memory effects in mixtures

In the following, we shall investigate the role that the mixture composition and the symmetry properties of component shapes play in the deposition process. We shall mainly concentrate on the response of the reversible RSA model to sudden perturbations of the desorption probability P_d in the case of binary mixtures, composed of the shapes of different rotational symmetries but of the same number of segments.

Consider the two-component mixture of objects (B) and (C) with the symmetry axis of $n_s^{(B)} = 1$ and $n_s^{(C)} = 3$ order, respectively. The reversible RSA process for a binary mixture is as follows. From a large reservoir of shapes, that contains the shapes (B) and (C) with equal fractional concentrations, we choose one shape at random. We randomly select a lattice site and try to deposit the chosen shape in the same manner as in the case of the reversible RSA of pure depositing objects. Each adsorption attempt is followed by a desorption one with probability P_d . The quantity of interest is the fraction of total lattice sites, $\theta^{(B)+(C)}(t)$, covered by the deposited objects (B) and (C) at time t .

Fig. 7 shows the time dependence of the partial coverages $\theta^{(B)}(t)$ and $\theta^{(C)}(t)$ resulting from the reversible RSA of the binary mixture of (B) and (C) shapes, for two values of desorption probability, $P_d = 0.0045, 0.0015$. For shape (C) of higher order of symmetry $n_s^{(C)} = 3$, the partial coverage $\theta^{(C)}(t)$ is a monotonously increasing function of time and has the same general features as the coverage $\theta^{(B)+(C)}(t)$ for the mixture (B) + (C). On the other hand, for shape (B) of lower order of symmetry $n_s^{(B)} = 1$, the partial coverage $\theta^{(B)}(t)$ is not monotonic in time. When the coverage $\theta^{(B)+(C)}(t)$ approaches to the coverage fraction that is equal to the jamming limit $\theta_j^{(B)+(C)} = 0.8624$, the partial coverage $\theta^{(B)}(t)$ reaches a broad maximum. This is followed by a slow relaxation of $\theta^{(B)}(t)$ to the smaller steady-state value $\theta_\infty^{(B)}$. At late enough time, when the coverage fraction is sufficient to make the geometry of the unoccupied sites complex, there is a strong dependence of the adsorption rate on the adsorbed shape [28,15]. Then, both rotational symmetry of the shapes and desorption events manage the single-particle readsorptions on the lattice and, eventually, allow replacements of the less symmetric particles by the more symmetric ones. This is reflected in the gradual decrease of the coverage fraction with time for the shape with the symmetry axis of lower order. Our results confirm that, for sufficiently high coverages of a mixture, the large times coverage fraction of more symmetric shapes exceeds the coverage fraction of less symmetric ones [31]. The steady-state value of the coverage fraction of the mixture components is always larger for the shapes with the symmetry axis of higher order n_s [31]. In Fig. 8 we compare the geometric status of the representative snapshots of patterns formed during the reversible deposition of mixture (B) + (C). The snapshots are taken at the times t_w needed for the system to reach (a) the coverage $\theta^{(B)+(C)}(t_w) = 0.88$, and (b) the steady-state coverage $\theta_\infty^{(B)+(C)} = 0.9066$ in the process of reversible deposition with $P_d = 0.0045$. In Fig. 8(a) the partial coverage of triangles (C) ($\theta^{(C)}(t_w) = 0.4375$) is slightly smaller than that of angled

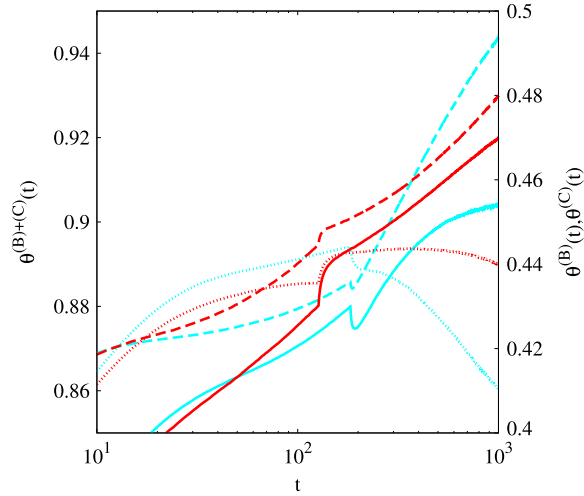


Fig. 10. Shown here is the response of the mixture (B) + (C) to the desorption probability shift $P_d^{(1)} \rightarrow P_d^{(2)}$. Black (red) lines represent the results obtained for the abrupt change $P_d^{(1)} = 0.0045 \rightarrow P_d^{(2)} = 0.0015$ at the time t_w needed for the system to reach the coverage $\theta_w^{(B)+(C)} = 0.88$ in the process of reversible RSA with $P_d^{(1)} = 0.0045$. Grey (light blue) lines represent the results obtained for the abrupt change $P_d^{(1)} = 0.0015 \rightarrow P_d^{(2)} = 0.0045$ at the time t_w needed for the system to reach the coverage $\theta_w^{(B)+(C)} = 0.88$ in the process of reversible RSA with $P_d^{(1)} = 0.0015$. The solid lines represent the temporal behavior of the coverage fraction $\theta^{(B)+(C)}(t)$ (left-hand axis). The dashed and dotted lines are plotted against the right-hand axis and give the coverage fraction versus time t of the component shapes (C), $\theta^{(C)}(t)$ (dashed), and (B), $\theta^{(B)}(t)$ (dotted). (For interpretation of the references to color in this figure legend, the reader is referred to the web version of this article.)

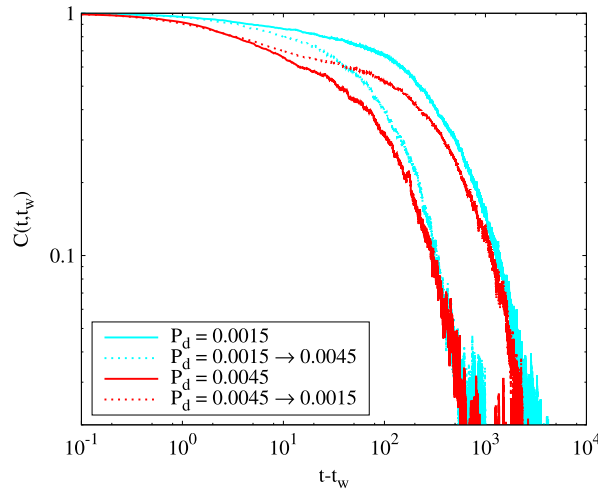


Fig. 11. Two-time density–density correlation function $C(t, t_w)$ for the mixture (B) + (C), as a function of $t - t_w$. The waiting time t_w corresponds to the time needed for the system to reach the coverage $\theta_w^{(B)+(C)} = 0.88$. The solid lines represent the temporal behavior of $C(t, t_w)$ obtained for the fixed desorption probabilities $P_d = 0.0015$ and 0.0045 , as indicated in the legend. The dashed lines represent the temporal dependence of $C(t, t_w)$ obtained from the runs during which an abrupt change of desorption probability $P_d^{(1)} = 0.0045 \rightarrow P_d^{(2)} = 0.0015$ ($P_d^{(1)} = 0.0015 \rightarrow P_d^{(2)} = 0.0045$) occurs at instant t_w , as indicated in the legend.

objects (B) ($\theta^{(B)}(t_w) = 0.4433$). However, at the steady-state density $\theta_\infty^{(B)+(C)} = 0.9066$ (Fig. 8(b)) the partial coverage fraction is larger for the shape with symmetry axis of higher order, i.e. $\theta_\infty^{(C)} = 0.5266 > \theta_\infty^{(B)} = 0.3800$.

Fig. 9 shows typical short-term memory effects after an abrupt change of the desorption probability P_d for the mixture (B) + (C) and for pure component shapes, (B) and (C). Desorption probability P_d is switched from $P_d^{(1)} = 0.0045$ to $P_d^{(2)} = 0.0015$ and vice-versa, at the time t_w needed for a mixture to reach the coverage $\theta_w = 0.88$. Again, we observe that after several adsorption/desorption events the “anomalous” response ceases and there is a crossover to the “normal” behavior, with the relaxation rate becoming the same as in the constant forcing mode. However, it is interesting to note that during this transient stage, the temporal evolution of the total coverage fraction $\theta^{(B)+(C)}(t)$ is very similar to the one observed for the shape with the symmetry axis of lower order. Hence, the dynamics of the short-time response of the mixture (B) + (C) to sudden perturbation of the desorption probability P_d is usually determined by the shape (B) of lower order of

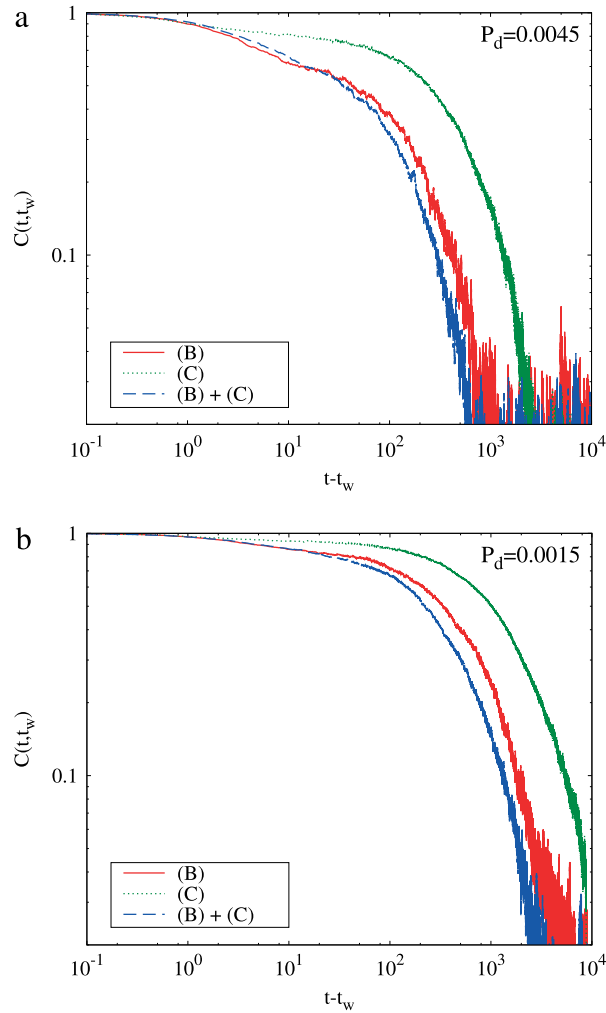


Fig. 12. Two-time density–density correlation function $C(t, t_w)$ for objects (B), (C), and mixture (B) + (C), as a function of $t - t_w$. The waiting time t_w corresponds to the time needed for the system to reach the coverage $\theta_w = 0.88$ when the desorption probability has the constant values (a) $P_d^{(1)} = 0.0045$, and (b) $P_d^{(1)} = 0.0015$.

symmetry, $n_s^{(B)} = 1$. Fig. 10 puts into evidence the temporal behavior of the partial coverage fraction for component shapes (B) and (C) during the transient time. As in the case of pure lattice shapes, we observe that the change in the compaction rate on short-time scales is less pronounced for the component shape of higher symmetry order.

In Fig. 11 we show the temporal dependence of $C(t, t_w)$ (see, Eq. (1)) for the mixture (B) + (C), when the waiting time t_w corresponds to the time needed for a system to reach the coverage $\theta_w^{(B)+(C)} = 0.88$. Correlation function $C(t, t_w)$ is displayed both for the fixed desorption probabilities, $P_d = 0.0015, 0.0045$, and for the cases with abrupt changes of desorption probability $P_d^{(1)} = 0.0045 \rightarrow P_d^{(2)} = 0.0015$, and $P_d^{(1)} = 0.0015 \rightarrow P_d^{(2)} = 0.0045$ at instant t_w . As for the pure lattice shapes, correlation functions calculated for the mixture (B) + (C) in the case of perturbed systems ($\Delta P_d = P_d^{(1)} - P_d^{(2)} \leq 0$) interpolates between the two correlation functions obtained for the systems with constant desorption probabilities $P_d^{(1)}$, and $P_d^{(2)}$.

It is instructive to compare the temporal behavior of the correlation function $C(t, t_w)$ for the mixture with results for $C(t, t_w)$ in the case of reversible deposition of pure component shapes. In Fig. 12 we show the time evolution of $C(t, t_w)$ during the deposition of objects (B), (C), and the mixture (B) + (C), for the waiting time t_w needed for a system to reach the coverage $\theta_w = 0.88$ when the desorption probability has the constant values $P_d^{(1)} = 0.0045$ (Fig. 12(a)) and $P_d^{(1)} = 0.0015$ (Fig. 12(b)). We can clearly see that for short times, $C(t, t_w)$ for the mixture (B) + (C) decays in a similar way as for shape (B) with the symmetry axis of lower order, $n_s^{(B)} = 1$. This changes slightly at intermediate times, when the correlation function $C(t, t_w)$ for the mixture starts to decay faster than the density correlations of component shapes. Hence, we observe the weakening of correlation features in multicomponent systems.

4. Conclusions

Along this paper, we have studied the nonequilibrium response of reversible RSA model to an instantaneous change in the value of desorption probability P_d . We have performed extensive simulations of reversible deposition using objects of different rotational symmetries on a triangular lattice. The shapes are made by self-avoiding lattice steps. First, it was shown that the change in the compaction rate has opposite sign than that of the modification of the desorption probability P_d , in contrast with the long-time behavior, where the relaxation is faster for larger P_d . These results are in a qualitative agreement with the observations in experiments on granular compaction [25]. Further, our numerical simulations have shown that the short-time response to an instantaneous change in the desorption probability P_d strongly depends on the symmetry properties of the shapes. We have found that the dynamical behavior is severely slowed down with the increase of the order of symmetry of the shape. When the desorption probability P_d is suddenly decreased/increased, compaction/decompaction rate of the perturbed system on short-time scales is larger for shapes with symmetry axis of lower order. We have also pointed out the importance of collective events for governing the short-time coverage behavior of shapes with different rotational symmetry.

We have also considered the nonequilibrium two-time density–density correlation function $C(t, t_w)$. We have observed that decay of the correlation function $C(t, t_w)$ depends on the order of symmetry axis of the shape n_s . It was confirmed that the density correlation decays slower for more symmetrical shapes. Eq. (2) states that, for the long enough times, the correlation $C(t, t_w)$ is a function of the ratio $\ln(t_w)/\ln(t)$. Such scaling behavior is in agreement with the Ising frustrated lattice gas model and the Tetris model [38], but in contrast with the parking lot model [27], for which a t/t_w behavior has been observed.

Special attention has been paid to the mixtures containing objects of various shapes, but made of the same number of segments. It was found that the dynamics of the short-time response of the mixture to sudden perturbation of the desorption probability P_d is determined by the shape of lower order of symmetry. In addition, our results confirm the weakening of correlation features for the deposition processes in multicomponent systems.

Acknowledgments

This work was supported by the Ministry of Education, Science, and Technological Development of the Republic of Serbia under projects ON171017 and III45016. Numerical simulations were run on the PARADOX supercomputing facility at the Scientific Computing Laboratory of the Institute of Physics Belgrade.

References

- [1] P.J. Flory, Intramolecular reaction between neighboring substituents of vinyl polymers, *J. Am. Chem. Soc.* 61 (1939) 1518.
- [2] J.W. Evans, Random and cooperative sequential adsorption, *Rev. Modern Phys.* 65 (1993) 1281–1329.
- [3] V. Privman, Dynamics of nonequilibrium deposition, *Colloids Surf. A* 165 (2000) 231–240.
- [4] A. Cadilhe, N.A.M. Araújo, V. Privman, Random sequential adsorption: from continuum to lattice and pre-patterned substrates, *J. Phys.: Condens. Matter* 19 (2007) 065124.
- [5] V. Privman (Ed.), *Nonequilibrium Statistical Mechanics in One Dimension*, Cambridge University Press, Cambridge, UK, 1997.
- [6] B. Senger, J.C. Voegel, P. Schaaf, Irreversible adsorption of colloidal particles on solid substrates, *Colloids Surf. A* 165 (2000) 255–285.
- [7] J. Talbot, G. Tarjus, P.R. Van Tassel, P. Viot, From car parking to protein adsorption: an overview of sequential adsorption processes, *Colloids Surf. A* 165 (2000) 287–324.
- [8] J.J. Ramsden, G.I. Bachmanova, A.I. Archakov, Kinetic evidence for protein clustering at a surface, *Phys. Rev. E* 50 (1994) 5072.
- [9] J. Talbot, G. Tarjus, P. Viot, Adsorption–desorption model and its application to vibrated granular materials, *Phys. Rev. E* 61 (2000) 5429–5438.
- [10] Lj. Budinski-Petković, S.B. Vrhovac, Memory effects in vibrated granular systems: Response properties in the generalized random sequential adsorption model, *Eur. Phys. J. E* 16 (2005) 89–96.
- [11] R.S. Ghaskadvi, M. Dennin, Reversible random sequential adsorption of dimers on a triangular lattice, *Phys. Rev. E* 61 (2000) 1232–1238.
- [12] E. Frey, A. Vilfan, Anomalous relaxation kinetics of biological latticeliquid binding models, *Chem. Phys.* 284 (2002) 287.
- [13] P.L. Krapivsky, E. Ben-Naim, Collective properties of adsorption–desorption processes, *J. Chem. Phys.* 100 (1994) 6778–6782.
- [14] Lj. Budinski-Petković, U. Kozmidis-Luburić, Adsorption–desorption processes of extended objects on a square lattice, *Physica A* 301 (2001) 174.
- [15] Lj. Budinski-Petković, M. Petković, Z.M. Jakšić, S.B. Vrhovac, Symmetry effects in reversible random sequential adsorption on triangular lattice, *Phys. Rev. E* 72 (2005) 046118.
- [16] I. Lončarević, Lj. Budinski-Petković, S.B. Vrhovac, A. Belić, Adsorption, desorption, and diffusion of k -mers on a one-dimensional lattice, *Phys. Rev. E* 80 (2009) 021115.
- [17] G. Tarjus, P. Viot, Statistical mechanical description of the parking–lot model for vibrated granular materials, *Phys. Rev. E* 69 (2004) 011307.
- [18] J.B. Knight, C.G. Fandrich, C.N. Lau, H.M. Jaeger, S.R. Nagel, Density relaxation in a vibrated granular material, *Phys. Rev. E* 51 (1995) 3957–3963.
- [19] F.X. Villarruel, B.E. Lauderdale, D.M. Mueth, H.M. Jaeger, Compaction of rods: Relaxation and ordering in a vibrated, anisotropic granular material, *Phys. Rev. E* 61 (2000) 6914–6921.
- [20] P. Philippe, D. Bideau, Compaction dynamics of granular medium under vertical tapping, *Europhys. Lett.* 60 (2002) 677.
- [21] P. Ribière, P. Richard, D. Bideau, R. Delannay, Experimental compaction of anisotropic granular media, *Eur. Phys. J. E* 16 (2005) 415–420.
- [22] P. Richard, M. Nicodemi, R. Delannay, P. Ribière, D. Bideau, Slow relaxation and compaction of granular systems, *Nature Mater.* 4 (2005) 121–128.
- [23] P. Ribière, P. Richard, P. Philippe, D. Bideau, R. Delannay, On the existence of stationary states during granular compaction, *Eur. Phys. J. E* 22 (2007) 249–253.
- [24] A.J. Kolan, E.R. Nowak, A.V. Tkachenko, Glassy behavior of the parking lot model, *Phys. Rev. E* 59 (1999) 3094–3099.
- [25] C. Jossierand, A. Tkachenko, D.M. Mueth, H.M. Jaeger, Memory effects in granular materials, *Phys. Rev. Lett.* 85 (2000) 3632–3635.
- [26] M. Nicolas, P. Duru, O. Poulliquen, Compaction of a granular material under cyclic shear, *Eur. Phys. J. E* 3 (2000) 309–314.
- [27] J. Talbot, G. Tarjus, P. Viot, Aging and response properties in the parking–lot model, *Eur. Phys. J. E* 5 (2001) 445–449.
- [28] Lj. Budinski-Petković, U. Kozmidis-Luburić, Random sequential adsorption on a triangular lattice, *Phys. Rev. E* 56 (1997) 6904.
- [29] Lj. Budinski-Petković, S.B. Vrhovac, I. Lončarević, Random sequential adsorption of polydisperse mixtures on discrete substrates, *Phys. Rev. E* 78 (2008) 061603.

- [30] D. Dujak, I. Lončarević, Lj. Budinski-Petković, S.B. Vrhovac, A. Karač, Adsorption–desorption processes of polydisperse mixtures on a triangular lattice, *Phys. Rev. E* 91 (2015) 032414. <http://dx.doi.org/10.1103/PhysRevE.91.032414>.
- [31] I. Lončarević, Lj. Budinski-Petković, S.B. Vrhovac, Reversible random sequential adsorption of mixtures on a triangular lattice, *Phys. Rev. E* 76 (2007) 031104.
- [32] S. Živković, Z.M. Jakšić, I. Lončarević, Lj. Budinski-Petković, S.B. Vrhovac, A. Belić, Optimization of the monolayer growth in adsorption–desorption processes, *Phys. Rev. E* 88 (2013) 052131. <http://dx.doi.org/10.1103/PhysRevE.88.052131>.
- [33] Lj. Budinski-Petković, U. Kozmidis-Luburić, A. Mihailović, Random sequential adsorption with diffusional relaxation on a square lattice, *Physica A* 293 (2001) 339.
- [34] Lj. Budinski-Petković, T. Tošić, Adsorption, desorption and diffusion of extended objects on a square lattice, *Physica A* 329 (2003) 350.
- [35] P. Ranjith, J.F. Marko, Filling of the one-dimensional lattice by k -mers proceeds via fast power-law-like kinetics, *Phys. Rev. E* 74 (2006) 041602.
- [36] S.S. Manna, N.M. Švrakić, Random sequential adsorption: line segments on the square lattice, *J. Phys. A: Math. Gen.* 24 (1991) L671–L676.
- [37] J. Talbot, G. Tarjus, P. Viot, Sluggish kinetics in the parking lot model, *J. Phys. A: Math. Gen.* 32 (1999) 2997–3003.
- [38] M. Nicodemi, A. Coniglio, Aging in out-of-equilibrium dynamics of models for granular media, *Phys. Rev. Lett.* 82 (1999) 916–919.

EPJ B

Condensed Matter
and Complex Systems

EPJ.org

your physics journal

Eur. Phys. J. B (2017) 90: 108

DOI: [10.1140/epjb/e2017-70597-6](https://doi.org/10.1140/epjb/e2017-70597-6)

The electrical conductance growth of a metallic granular packing

Zorica M. Jakšić, Milica Cvetković, Julija R. Šćepanović, Ivana Lončarević,
Ljuba Budinski-Petković and Slobodan B. Vrhovac

edp sciences



 Springer

The electrical conductance growth of a metallic granular packing

Zorica M. Jakšić¹, Milica Cvetković¹, Julija R. Šćepanović¹, Ivana Lončarević²,
Ljuba Budinski-Petković², and Slobodan B. Vrhovac^{1,a}

¹ Institute of Physics Belgrade, University of Belgrade, Pregrevica 118, 11080 Zemun, Belgrade, Serbia

² Faculty of Engineering, Trg D. Obradovića 6, 21000 Novi Sad, Serbia

Received 7 October 2016 / Received in final form 12 March 2017

Published online 14 June 2017 – © EDP Sciences, Società Italiana di Fisica, Springer-Verlag 2017

Abstract. We report on measurements of the electrical conductivity on a two-dimensional packing of metallic disks when a stable current of ~ 1 mA flows through the system. At low applied currents, the conductance σ is found to increase by a pattern $\sigma(t) = \sigma_\infty - \Delta\sigma E_\alpha[-(t/\tau)^\alpha]$, where E_α denotes the Mittag-Leffler function of order $\alpha \in (0, 1)$. By changing the inclination angle θ of the granular bed from horizontal, we have studied the impact of the effective gravitational acceleration $g_{\text{eff}} = g \sin \theta$ on the relaxation features of the conductance $\sigma(t)$. The characteristic timescale τ is found to grow when effective gravity g_{eff} decreases. By changing both the distance between the electrodes and the number of grains in the packing, we have shown that the long term resistance decay observed in the experiment is related to local micro-contacts rearrangements at each disk. By focusing on the electro-mechanical processes that allow both creation and breakdown of micro-contacts between two disks, we present an approach to granular conduction based on subordination of stochastic processes. In order to imitate, in a very simplified way, the conduction dynamics of granular material at low currents, we impose that the micro-contacts at the interface switch stochastically between two possible states, “on” and “off”, characterizing the conductivity of the micro-contact. We assume that the time intervals between the consecutive changes of state are governed by a certain waiting-time distribution. It is demonstrated how the microscopic random dynamics regarding the micro-contacts leads to the macroscopic observation of slow conductance growth, described by an exact fractional kinetic equations.

1 Introduction

The electrical resistance of a granular packing is a combination of the individual resistances of both the grains and the contacts between them [1]. Such a combination is a strong function of global properties concerning the grain assembly (packing size and density, external loads) and local properties at the contact scale of two grains (surface state, roughness, degree of oxidation, presence of impurities). Understanding the electrical conduction through real granular materials is a complicated many body problem since particles may have simultaneously broad distributions of sizes and strongly varying morphologies.

The main contribution to the overall conductivity of the packing of metallic grains comes from the contact resistances, which may have two origins: tunneling [2] and constrictions [3]. The tunneling resistances may have very high values, but especially concern metallic powders coated by thin oxide film. On the other hand, constriction resistances are due to the narrowness of the conducting path owing to the small contact area between two particles. Actually, any contact is made of a number of touching points rather than by well-defined surface.

Experiments on the electrical properties of granular systems have been performed in the past. In 1890, Branly [4] discovered the extreme sensitivity of the conductivity of metal filling to an electromagnetic wave. The Branly’s effect is an instability of the electrical conductance that appears in oxidized granular metallic material under mechanical loading [5–9]. Electrical conduction within metallic granular packings displays other interesting properties. Indeed, in both 1D and 2D granular systems at low current, the wide distribution of contact resistances results in a logarithmic behavior for the voltage/current characteristics [10]. At high enough current, the voltage saturates due to the local welding of micro-contacts between grains [11]. Furthermore, electrical conduction shows a large sensitivity on the small mechanical and thermal perturbations of the packing [12,13]. Origin of these large non-Gaussian conductance fluctuations should be found in local micro-contact rearrangements at each grain rather than collective rearrangements of grains inside the packing.

Although many experiments have been performed for studying electrical aspects of granular matter, only few reports [14,15] can be found for describing the temporal evolution of the electrical resistance $R(t)$ in packing

^a e-mail: vrhovac@ipb.ac.rs

of metallic grains when a stable current flows through the system. Dorbolo et al. [14] measured the electrical resistance in a 2D system and found that the decay process in the case of injected currents $35 \lesssim I \lesssim 50$ mA may be decomposed into three phases. At first the resistance decreases during the first minute, after that the curves $R(t)$ are stabilized during $\sim 10^3$ s before decreasing again. However, for lower injected currents $10 \lesssim I \lesssim 25$, the resistance $R(t)$ is a monotonically decreasing function. It would be interesting to find out where such unusual behavior comes from. Dorbolo et al. [14] suggested that the long term decay of the electric resistance $R(t)$ seems to be related to the enhancement of contacts themselves. The aim of this work is to investigate the regime of very small electric currents $I \sim 1$ mA in order to gain a better understanding the origin of the slow electrical resistance relaxation in granular packing.

We focus on the electrical transport within 2D packing of metallic disks directly connected to an electrical source. A fixed current has been injected during a few hours and conductance $\sigma(t) = 1/R(t)$ has been recorded at regular intervals. Experiments were performed for two different inclination angles θ of the granular bed from horizontal. Consequently, we have considered the impact of the effective gravitational acceleration $g_{\text{eff}} = g \sin \theta$ on the relaxation features of the conductance $\sigma(t)$. We could change the distance between the electrodes, i.e. the number of grains in the packing. In this way we were able to compare the influence of large force chain rearrangements with impact of local micro-contact rearrangements at each disk on overall electrical conductivity of the packing.

We have tried to fit different functional forms to the slow temporal relaxation of $\sigma(t)$ obtained in the experiments, looking in particular at the relaxation functions proposed in the experimental and numerical studies of disordered systems [16]. We have found that the most suitable functional form for our experimental data is the Mittag-Leffler law (1) (corresponding mathematical definitions are provided later in the text; see Eqs. (2) and (3)). The main question that needs an answer is whether equation (1) represents only a convenient fitting expression or it has a more fundamental meaning, associated to some peculiar dynamical events which are dominant in the conductance relaxation. We would like to elucidate this point more thoroughly in order to develop a dynamic model for the electric contact between two grains based on the stochastic fractional process that captures this relaxation dynamics.

A typical rough surface of metallic grain may include many small contacts of varying sizes. Our model assumes the electrical current flow is between two contiguous bulk conducting materials and the current flows through the conducting a-spots or constrictions (micro-contacts) [3]. The model does not explicitly account for quantum effects or the spreading resistance resulting from the thin film micro-contacts. Our approach is based on the probabilistic formalism of limit theorems which provides tools to relate the non-differentiable nature of microscopic dynamics of components in complex systems to the macroscopic

description of such systems in the form of fractional operators [17–20]. We suppose that there are only two possible states of micro-contacts, referred to as “switched on” and “switched off”. In order to imitate, in a very simplified way, the relaxation features of conductance $\sigma(t)$ under low currents, we impose that the micro-contacts at interface switch stochastically between two possible states. Starting with the description of the two-state system evolution as a Markovian process, we develop the analysis on a subordinated random process. The process differs from the Markovian ones by the temporal variable becoming random [19]. This generalization is of a stochastic origin and produces the fractional operator in the resulting evolution equation for the conductance. The evolution equation is capable of reproducing a wide range of experimental behavior.

In the following section, we present the experimental set-up and describe the experimental procedures. The experimental results are reported and discussed in Section 3. Definition of the model and discussion on the physical interpretation of the model parameters are given in Section 4. In the same section results of numerical simulation are presented, discussed, and wherever possible compared with analytical results. Finally, we summarize our findings in Section 5.

2 Experiment

Let us now describe our experimental set-up, which is presented in Figure 1. Experiments were carried out on a 2D granular medium, i.e. the motion of the grains was confined to a plane. The granular packing is constituted of metallic cylinders of millimetric size contained in a rectangular box made of two parallel glass plates, with an inner gap of thickness 3.4 mm, slightly larger than the height of the cylinders, $h = 3.00 \pm 0.01$ mm. The lateral walls of the box delimit a rectangular frame of height $H = 340$ mm and an adjustable width of typically $L = 300$ mm. We can change the distance between the lateral walls, i.e. the number of grains in 2D packing, to separate local behavior from collective behavior. The box is secured on a heavy plane able to be inclined at different rates (5° – 20° s^{-1}) so that we could set an arbitrary inclination angle θ from the horizontal. The angle of inclination θ is measured by means of a goniometer fixed to the plane. See Figure 1b for a sketch of this angle definition.

The cylinders of diameter $d = 6.00 \pm 0.05$ mm were used to prepare the monodisperse packings containing about 2400 grains. Disordered packings are prepared by pouring grains onto an initially horizontal glass plate at once. Then, they are spread until a flat layer is obtained, where the cylinders are randomly deposited without contact between them and at rest. The angle of the plane is then slowly increased up to the angle $\theta = 45^\circ$ or $\theta = 85^\circ$, at constant angular velocity. These final inclination angles correspond to a value larger than the static Coulomb angle of friction between the metallic grains and the glass plate, which is around 25° . During the plane rotation, grains therefore freely slide downward and reach a mechanically

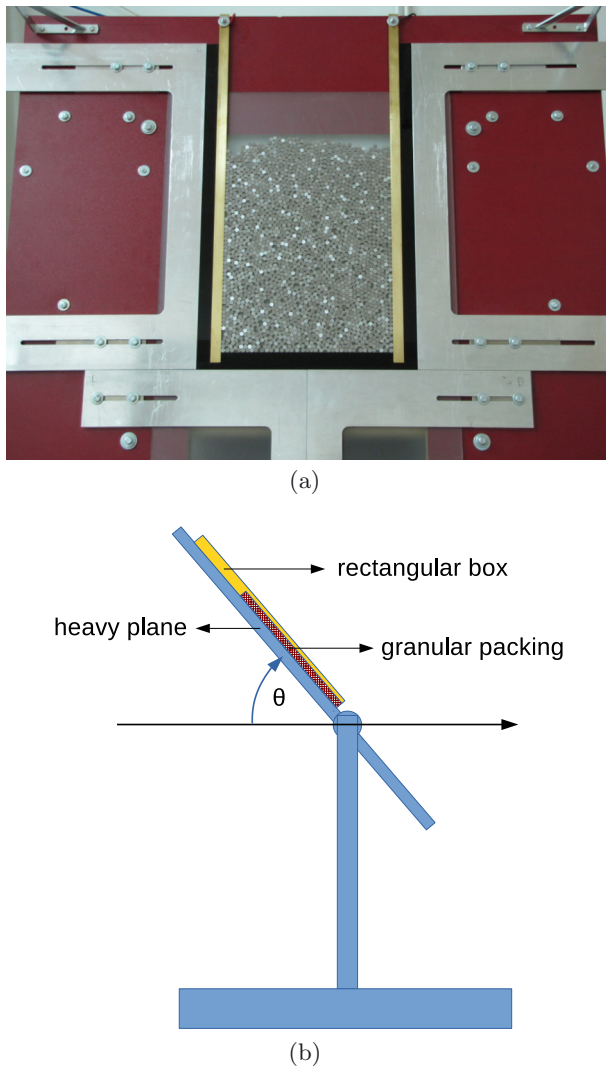


Fig. 1. (a) Photograph of the experimental setup. (b) Schematic diagram of the experimental setup (side view). The hatched area indicates the granular packing and θ is the inclination angle of the packing from the horizontal.

stable state. This way we control the balance of tangential and normal gravitational force on the layer and thus the contact network (and certainly also force network) inside the granular material. The measured packing fractions of these disordered packings are $\rho = 0.78\text{--}0.80 \pm 0.01$. Partially ordered packings are obtained by using the same initial procedure followed by the vibration of the inclined plane with a hammer-like device installed below the container. The packing fraction of densely packed systems is $\rho = 0.81\text{--}0.86 \pm 0.01$. Those densities are far from the close packing limit $\rho_{cp} = \pi/2\sqrt{3} \approx 0.91$ [21].

The bottom side of the rectangular box is electrically insulated. The current is injected to the packing side and not to only one grain. Long electrical contacts are disposed on two opposite lateral walls of the box. Electrical contacts are connected by cables to a Fluke 8008A Digital Multimeter which allows to measure the resistance. During

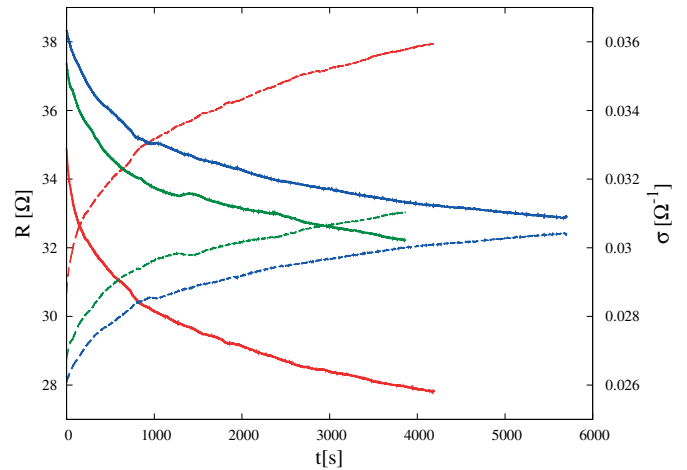


Fig. 2. Typical temporal evolutions of the resistance $R(t)$ obtained for an injected current $I = 1$ mA and an inclination angle $\theta = 85^\circ$ (solid lines). The corresponding values of the conductance $\sigma(t)$ are given on the right axis (dashed lines). The different curves are obtained for several disordered packings prepared by using the same procedure.

the experiment, we have recorded the temporal evolution of the electrical resistance $R(t)$ of a metallic grains heap when a stable current flows through the system. A fixed current of $I = 1$ mA is injected during $\sim 20\text{--}100$ min and the resistance $R(t)$ is sampled every 5 s. Different materials have been used for the electrodes (brass and stainless steel). We observed that the main relaxation features of conductance $\sigma(t)$ do not qualitatively depend on the electrode material. After each measurement of resistance $R(t)$, effective gravitational force on the grains is reduced to zero by placing the container in a horizontal position, and we rearrange the cylinders which creates new contacts for the next measurement.

The experimental setup has a high sensitivity to thermal perturbations and mechanical vibrations. It should be noted that we controlled the ambient humidity and temperature of the laboratory. The experimental reproducibility is qualitatively good although the exact values of conductance may exhibit fluctuations from one packing preparation to another.

3 Experimental results and discussion

In Figure 2, typical variations of the resistance $R(t)$ are shown versus time for an injected current $I = 1$ mA and an inclination angle $\theta = 85^\circ$. Also included in Figure 2 is the temporal evolution of the conductance $\sigma(t)$ for the same experimental conditions. We observe that for the fixed injected current, the initial resistance for different packings differs from one another. This should be attributed to the changes in the contact network during the formation of new packings. It must be noted that the initial resistance dependence on the injected current in the range between 10 and 65 mA has been extensively analyzed in the experiments by Dorbolo et al. [14], that suggested that the initial

resistance decreases with the injected current. As seen in Figure 2, resistance $R(t)$ decreases very slowly with time for each packing. Our measurements have suggested that resistance $R(t)$ continues to decrease toward some saturation value. With the compacted (partially ordered) granular medium we made the same experiments and obtained qualitatively the same long-time behavior of the conductivity. Such behavior of the electrical conductivity, Dorbolo et al. [14] was demonstrated in the experiments at higher currents, $10 \text{ mA} \leq I \lesssim 25 \text{ mA}$.

Looking for a function that gives the best fit to the temporal evolution of the conductance $\sigma(t)$ in the case of very low injected currents $I \approx 10^{-3} \text{ A}$, we have obtained that the best agreement with our experimental data gives the Mittag-Leffler function. The fitting function we have used is of the form

$$\sigma(t) = \sigma_\infty - \Delta\sigma E_\alpha(-(t/\tau)^\alpha), \quad (1)$$

where σ_∞ , $\Delta\sigma$, τ , and α are the fitting parameters. Parameter τ determines the characteristic time of the temporal evolution of conductance $\sigma = \sigma(t)$, and α measures the rate of conductance relaxation on this time scale. The parameter σ_∞ is the asymptotic value of the conductance $\sigma(t)$ when $t \rightarrow \infty$, and $\Delta\sigma = \sigma_\infty - \sigma(0)$.

In equation (1), E_α denotes the Mittag-Leffler function of order $\alpha \in (0, 1)$ [22]. It is defined through the inverse Laplace transform \mathcal{L}

$$E_\alpha[-(t/\tau)^\alpha] = \mathcal{L}[(u + \tau^{-\alpha}u^{1-\alpha})^{-1}], \quad (2)$$

from which the series expansion

$$E_\alpha[-(t/\tau)^\alpha] = \sum_{n=0}^{\infty} \frac{(-t/\tau)^\alpha n}{\Gamma(1 + \alpha n)}, \quad (3)$$

can be deduced; in particular, $E_1(-t/\tau) = \exp(-t/\tau)$. The Mittag-Leffler function interpolates between the initial stretched exponential form

$$E_\alpha[-(t/\tau)^\alpha] \sim \Phi_1(t) = \exp\left[-\frac{1}{\Gamma(1 + \alpha)}(t/\tau)^\alpha\right], \quad t \ll \tau, \quad (4)$$

and the long-time power-law behavior

$$E_\alpha[-(t/\tau)^\alpha] \sim \Phi_2(t) = \frac{1}{\Gamma(1 - \alpha)}(t/\tau)^{-\alpha}, \quad t \gg \tau. \quad (5)$$

In Figure 3 we compare the temporal evolution of the conductivity $\sigma(t)$ obtained when the experiment is performed for two different inclination angles of the plane, $\theta = 85^\circ$, 45° . In the same figure the fits to the Mittag-Leffler law (Eq. (1)) are also given, demonstrating that it is excellently obeyed. The two fitting parameters are $\tau(85^\circ) = 1.46 \times 10^4 \text{ s}$, $\alpha(85^\circ) = 0.461$ for $\theta = 85^\circ$, and $\tau(45^\circ) = 2.68 \times 10^5 \text{ s}$, $\alpha(45^\circ) = 0.327$ for $\theta = 45^\circ$. In addition, the inset of Figure 3 compares the evolution of normalized conductivity $\sigma_r(t) = (\sigma(t) - \sigma(0))/(\sigma_\infty - \sigma(0)) = 1 - E[-(t/\tau)^\alpha]$ for the two values of inclination angle, $\theta = 85^\circ$, 45° . It can be seen that the relaxation dynamics gets slower ($\tau(85^\circ) < \tau(45^\circ)$), and the evolution of the

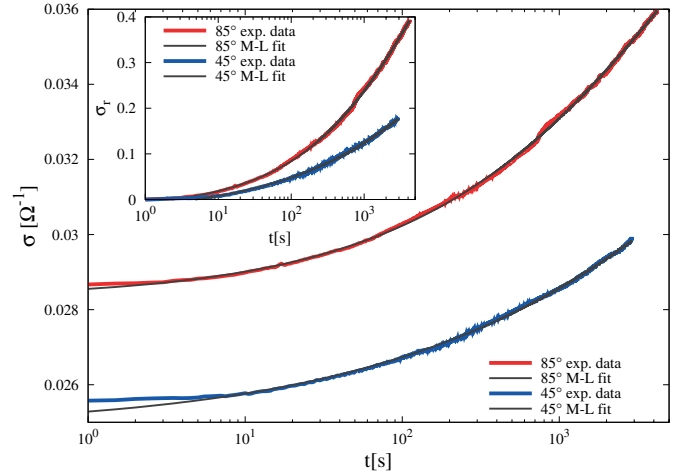


Fig. 3. Temporal evolution of the conductivity $\sigma(t)$ obtained for two different inclination angles of the plane, $\theta = 85^\circ$, 45° . The thin (black) lines are the Mittag-Leffler fits of equation (1), with parameters $\tau(85^\circ) = 1.46 \times 10^4 \text{ s}$, $\alpha(85^\circ) = 0.461$, and $\tau(45^\circ) = 2.68 \times 10^5 \text{ s}$, $\alpha(45^\circ) = 0.327$. Inset: temporal evolution of the normalized conductance $\sigma_r(t) = (\sigma(t) - \sigma(0))/(\sigma_\infty - \sigma(0)) = 1 - E[-(t/\tau)^\alpha]$ for $\theta = 85^\circ$, 45° .

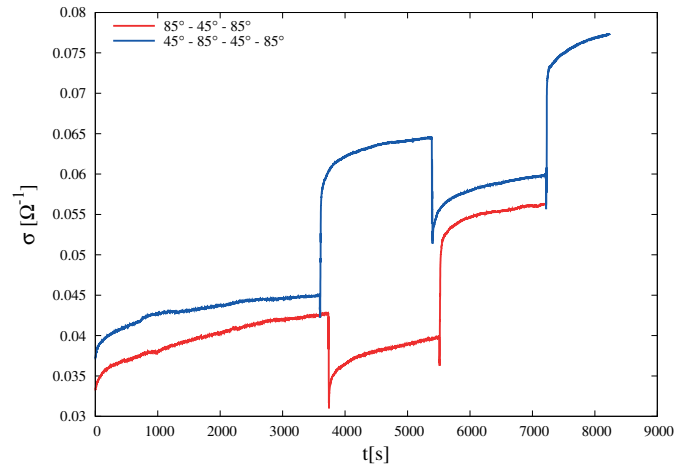


Fig. 4. Time evolution of the conductivity $\sigma(t)$ when the inclination angle θ is changed from $\theta_1 = 85^\circ$ to $\theta_2 = 45^\circ$ and vice versa in different time instants.

conductivity $\sigma(t)$ toward the saturation value takes place on much wider time scale ($\alpha(85^\circ) > \alpha(45^\circ)$) when the effective gravity $g_{\text{eff}} = g \sin \theta$ decreases.

Figure 4 shows the rapid variation of the electrical conductivity $\sigma(t)$ of granular packing induced by the abrupt change of the effective gravity $g_{\text{eff}} = g \sin \theta$. In this experiment, the inclination angle θ is changed from $\theta_1 = 85^\circ$ to $\theta_2 = 45^\circ$ and vice versa in three different time instants. For a sudden decrease in $g_{\text{eff}}(\theta_1) \rightarrow g_{\text{eff}}(\theta_2)$ it is observed that on short-time scales the conductivity σ decreases rapidly, while for a sudden increase in $g_{\text{eff}}(\theta_2) \rightarrow g_{\text{eff}}(\theta_1)$ the conductivity increases for short times. This behavior is transient, and after short time the usual increasing rate of conductivity $\sigma(t)$ growth is recovered. In addition, the rapid variation of the electrical conductivity induced

by a sudden change of the inclination angle θ is proportional to the angle change, $\Delta\theta = |\theta_1 - \theta_2|$ (not shown here).

Our findings for the behavior of the electrical conductivity, shown in Figures 3 and 4, clearly demonstrate that a granular material in the case of the higher values of effective gravity has a higher electrical conductivity. This is in agreement with experiments and numerical simulations examining the effect of gravity on the force network and microstructural properties of granular packings [23–27]. As gravity decreased, the spatial distribution of the force chain network changed from a dense, tangled network to one consisting of less tangled, longer chains. Intuitively, we would expect that shorter chains can support greater stress since there are fewer potential failure points. Thus, packings with more branching in their force chain network, induced by higher values of effective gravity are macroscopically stronger and more electrically conductive, since there are more pathways available for stress and electric current transmission.

Previously described “geometrical” contact disorder which arises from the lowering of the number of real contacts when the effective gravity decreases is not the sole cause that induces the abrupt changes of conductivity shown in Figure 4. Additionally, the “physical” contact disorder appears because some contacts are good transmitters, other are not. As the stress increases, some contacts may become active in turn, as the contact area may be cleaned of oxide coating or some other impurities. Consequently, the number of active contacts increases with the effective gravity. This effect contributes to the conductance due to the growth of the conducting network.

In order to better understand the reasons for the long term decay of the electric resistance, we have made the following experiment. The distance between the lateral walls of the box (electrodes) is reduced to $d(1 + \sqrt{2})$. In this channel, six, nine or twelve disks are arranged to form square packing as illustrated in Figure 5a. This packing can easily be reproduced before each experiment. For the given configurations, each conductive path between the electrodes always includes only three disks. Therefore, the total number of possible conductive paths is equal to 5, 9, and 13, for configurations with 6, 9, and 12 disks, respectively. For configurations with small number of possible conductive paths, one should expect to detect abrupt changes in the resistance as a result of forming new conductive paths or termination of existing ones. However, Figure 5b shows that the resistance decreases continuously for all three configurations of disks. This means that the number of conductive paths does not change, but their conductivity increases over time. The fact that the decay of the resistance still holds for six disks (or five conductive paths), suggests that the origin of these changes is local. Consequently, long term resistance decay observed in the experiment is not related to large force chain rearrangements, but to individual microcontacts between two disks that rearrange.

It must be stressed that the time behavior of the conductance $\sigma(t)$ in experiments with reduced distance between the lateral walls (electrodes) is consistent with the

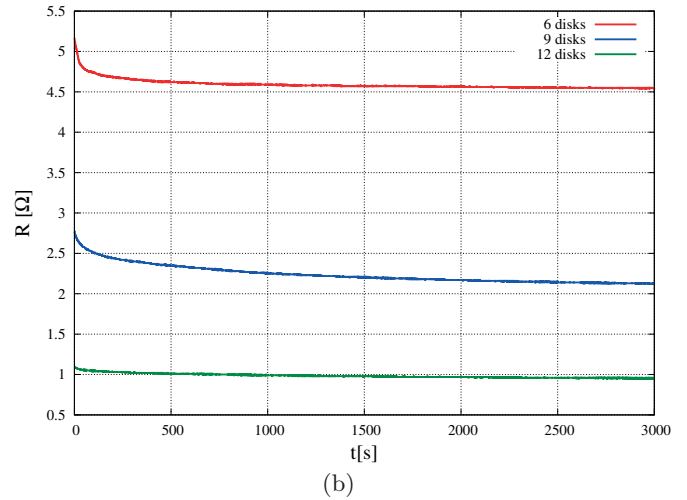
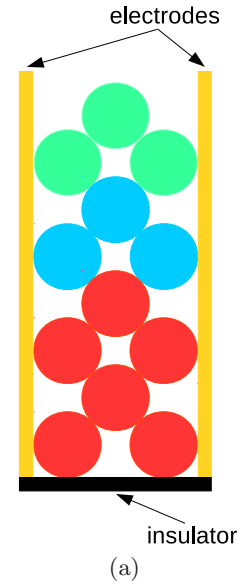


Fig. 5. Experiment with reduced distance between the lateral walls (electrodes). (a) Sketch of the 2D experimental setup. (b) Temporal evolutions of the resistance $R(t)$ obtained for configurations with 6, 9, and 12 disks shown on plot (a).

Mittag-Leffler law (1). According to equation (1), we get

$$\frac{\Delta\sigma(t)}{\Delta\sigma(0)} = \frac{\sigma_\infty - \sigma(t)}{\sigma_\infty - \sigma(0)} = E_\alpha(-(t/\tau)^\alpha). \quad (6)$$

Temporal evolution of the quantity $\Delta\sigma(t)/\Delta\sigma(0)$ for the configuration with 9 disks (see Fig. 5) is shown in Figure 6 on double logarithmic scale together with the Mittag-Leffler fitting function $E_\alpha(-(t/\tau)^\alpha)$. In addition, Figure 6 shows the functions $\Phi_1(t)$ and $\Phi_2(t)$ (see Eqs. (4) and (5)) determined by fitting the conductance behavior $\sigma(t)$ to the Mittag-Leffler functional form (1).

The observed slow resistance decay might be related to the roughness of the surface of the disks. When two surfaces meet, and because no surface is perfectly smooth, asperity peaks or “a-spots” from each surface meet at the interface and form contact areas [3]. In this

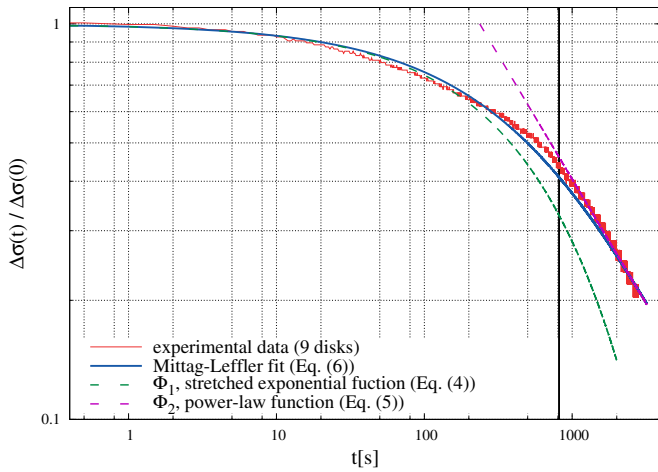


Fig. 6. Shown here is the double logarithmic plot of the temporal evolution of the normalized conductance deviation from the asymptotic value, $\Delta\sigma(t)/\Delta\sigma(0) = (\sigma_\infty - \sigma(t))/(\sigma_\infty - \sigma(0))$ (Eq. (6)). Data for $\sigma(t)$ are obtained for configuration with 9 disks in the experiment with reduced distance between the electrodes (Fig. 5). The solid (blue) line is the Mittag-Leffler function $E_\alpha(-(t/\tau)^\alpha)$, with parameters $\tau = 815.3$ s, $\alpha = 0.628$, and $\sigma_\infty = 0.497$. The dashed lines give the functions $\Phi_1(t)$ and $\Phi_2(t)$ (see Eqs. (4) and (5)), as indicated in the legend. The solid vertical line indicates the characteristic time $\tau = 815.3$ of the temporal evolution of conductance $\sigma(t)$.

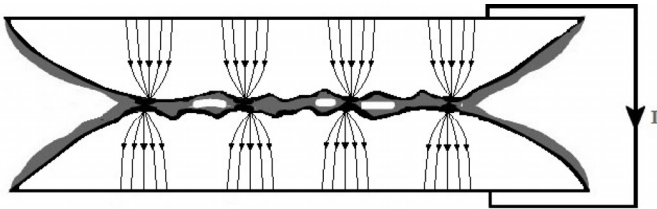


Fig. 7. Schematic diagram of current flow through a contact spot. The electrical connection between the two surfaces takes place at discrete solid spots, also known as a-spots or asperities, based on the roughness of the surfaces. These spots determine the true size of the contact area that can be as small as only a fraction of the nominal contact area.

way, when two disks are brought into contact, the surface irregularities of each disk create a large number of conducting micro-channels. The presence of the micro-contacts leads to a constriction of the current lines on tiny areas. Figure 7 shows a graphical representation of a contact area and contacting a-spots. Instead of passing uniformly through the oxide layer, electric current prefers to be divided in a large number of micro-currents following conducting micro-channels [2,3,11,13]. The convergence of the electrical current through the conducting a-spots is known as the constriction resistance or commonly the contact resistance [1]. With a small contact region comes a large contact resistance. Consequently, the flow of the current through the micro-contacts contributes to their heating by Joule effect and causes a softening or even melting some of them. At the same time, the mechanical stabilization of the discs, initiated by thermal perturbations,

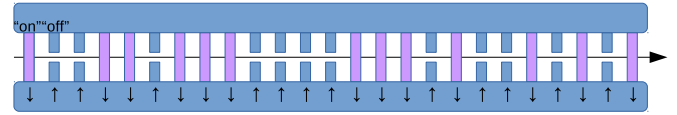


Fig. 8. Schematic picture of the dynamic model of the electric contact between two grains described in the text.

leads to the local micro-contact rearrangements at each disk, during which the new micro-contacts can be created. These electro-mechanical processes then allow both creation and breakdown of the micro-contacts between two disks. Adaptation of the micro-contacts to the flow of the electric current leads to a larger effective contact surface, thereby making the resistance of contact smaller.

4 Definition of the model and numerical simulation

Previous findings allow us to build a dynamic model of the electric contact between two grains that provides a very slow relaxation of electrical conductivity observed in the experiments. Our model can be regarded as a very simple picture of the interface between two metallic grains which is composed of a large number of micro-contacts. We consider a one-dimensional lattice, with N micro-contacts located at its lattice points (see Fig. 8). Each micro-contact can take two possible states, referred to as “switched on” (\downarrow) and “switched off” (\uparrow). A configuration of the contact is uniquely defined by N orientation variables $\{\Lambda_n | n = 1, \dots, N\}$, with $\Lambda_n = +1$ denoting a micro-contact in state “on” (\downarrow), and $\Lambda_n = 0$ denoting a micro-contact in state “off” (\uparrow). To each micro-channel n in the state “on”, we assigned the same resistance, $r_n \equiv r^{(c)}$. When micro-channel n is in the state “off”, its resistance is too high and no current flows through it, so that we formally take $r_n = \infty$.

At first, we can try to model the contact interface, naively, by a continuous-time stochastic dynamics, described by the following general kinetic equations:

$$\frac{dp^{(\downarrow)}}{dt} = \omega_{\uparrow\downarrow}p^{(\uparrow)}(t) - \omega_{\downarrow\uparrow}p^{(\downarrow)}(t), \quad (7)$$

$$\frac{dp^{(\uparrow)}}{dt} = \omega_{\downarrow\uparrow}p^{(\downarrow)}(t) - \omega_{\uparrow\downarrow}p^{(\uparrow)}(t), \quad (8)$$

where $p^{(\uparrow)}(t)$ and $p^{(\downarrow)}(t)$ are the probabilities for finding the micro-contact in the states “off” and “on” at time t , respectively. Here, $\omega_{\uparrow\downarrow}$ and $\omega_{\downarrow\uparrow}$ represent, respectively, the constant transition probability rate from the state “off” to the state “on”, and from the state “on” to the state “off”. The term $\omega_{\downarrow\uparrow}p^{(\downarrow)}$ describes transition into the state “on” from the state “off”, and $\omega_{\uparrow\downarrow}p^{(\downarrow)}$ corresponds to transition out of the “on” into the other state “off”. Since the micro-channels of conduction are connected in parallel, the total contact conductance $\sigma(t) = 1/R(t)$ is expressed as the sum of their individual conductances

$$\sigma_n = 1/r_n = 1/r^{(c)} \equiv \sigma^{(c)}:$$

$$\sigma(t) = \sum_{n=1}^N A_n(t) \sigma^{(c)} = \sigma_{\max} p^{(\downarrow)}(t), \quad (9)$$

where $\sigma_{\max} = N\sigma^{(c)}$ is the conductance when all micro-contacts are in the state “on”. We have two limits: $p^{(\downarrow)} = 1$ when $\sigma = \sigma_{\max}$ (resistance is minimal) and $p^{(\downarrow)} = 0$ when $\sigma = 0$. Setting $\left. \frac{dp^{(\downarrow)}}{dt} \right|_{t \rightarrow \infty} = 0$ and $\left. \frac{dp^{(\uparrow)}}{dt} \right|_{t \rightarrow \infty} = 0$ in equations (7) and (8) they become a set of two algebraic equations whose solution provides the steady-state values of the conductance $\sigma(\infty)$:

$$\sigma(\infty) = \sigma_{\max} p^{(\downarrow)}(\infty) = \sigma_{\max} \frac{\omega_{\downarrow\uparrow}}{\omega}, \quad (10)$$

where $\omega = \omega_{\downarrow\uparrow} + \omega_{\uparrow\downarrow}$ is the total transition probability rate. This steady state will be reached by the system from any initial configuration. Assume that for $t = 0$:

$$p^{(\uparrow)}(0) = \frac{N^{(\uparrow)}(t=0)}{N}, \quad p^{(\downarrow)}(0) = \frac{N^{(\downarrow)}(t=0)}{N}, \quad (11)$$

where $N^{(\uparrow)}$ and $N^{(\downarrow)}$ are the number of micro-contacts in the states “off” and “on”, respectively. Without loss of generality we assume that for $t = 0$ the states “off” dominate, i.e. $N^{(\uparrow)}(t=0) > N^{(\downarrow)}(t=0)$. The solution of equations (7) and (8) with initial conditions (11) is straightforward. Accordingly, the conductance of the contact (Eq. (9)) grows exponentially in time towards the steady state value:

$$\sigma(t) = \sigma(\infty) - [\sigma(\infty) - \sigma(0)] \exp(-\omega t), \quad (12)$$

where $\sigma(0) = \sigma_{\max} p^{(\downarrow)}(0) = \sigma_{\max} N^{(\downarrow)}(t=0)/N$ is the conductance at the moment $t = 0$, when an electric current is turned on.

Not unexpectedly, this simplified model does not describe the behavior of a real electrical contact between metallic grains at low applied current, i.e. it is not a good approximation for the conduction dynamics. Our model requires substantial addition and extension in order to have the ability to properly capture the slow relaxation dynamics of conductivity observed in the experiments. The main physical idea of our approach is that the time intervals between the successive micro-contact closing/opening are governed by a certain waiting-time distribution $\psi(t)$. This function governs the *random time* intervals between single microscopic jumps “on” (\downarrow) \leftrightarrow “off” (\uparrow) of the micro-contacts. Actually, in our model the evolutions of the number of micro-contacts in the states “on” and “off” are subordinated by another random process. Random switching of micro-contacts between the states “on” and “off” are *parent* random processes $Y(t)$ in the sense of subordination (see Eqs. (7) and (8)). Recall that a subordinated process $Y[U(t)]$ is obtained by randomizing the time clock of a random process $Y(t)$ using a random process $U(t)$. The latter process is referred to as the randomized time. The new clock generalizes the deterministic

time clock of the kinetic equation for the Markovian process (Eqs. (7) and (8)).

Now we consider in more details the evolution of the number of micro-contacts in the states “on” and “off”. These are *parent* random processes in the sense of subordination. Consider a sequence T_i , $i = 1, 2, \dots$ of non-negative, independent, identically distributed random variables which represent the waiting time intervals between single microscopic jumps “on” (\downarrow) \leftrightarrow “off” (\uparrow) of the micro-contacts. If the waiting times T_i belong to the strict domain of attraction of an α -stable distribution ($0 < \alpha < 1$), their sum $n^{-1/\alpha} \sum_{i=1}^n T_i$, $n \in N$ converges in distribution to a stable law with the same index α [17,28,29]. The continuous limit of the discrete counting process $\{N_t\}_{t \geq 0} = \max\{n \in N | \sum_{i=1}^n T_i \leq t\}$ is the hitting time process $S(t)$ (also called the first passage time). We choose the nondecreasing random process $S(t)$ for a new time clock (stochastic time arrow). The probability density of the process $S(t)$ has the following form [30]:

$$p_\alpha^S(t, \tau) = \frac{1}{2\pi j} \int_{\text{Br}} u^{\alpha-1} \exp(ut - \tau u^\alpha) du = t^{-\alpha} F_\alpha\left(\frac{\tau}{t^\alpha}\right), \quad (13)$$

where Br denotes the Bromwich path and $j = \sqrt{-1}$. The function $F_\alpha(z)$ can be expanded as a Taylor series:

$$F_\alpha(z) = \sum_{k=0}^{\infty} \frac{(-z)^k}{k! \Gamma(1 - \alpha - k\alpha)}, \quad (14)$$

where $\Gamma(\cdot)$ is the gamma function. The probability density $p_\alpha^S(t, \tau)$ determines the probability to be at the internal time (or so-called operational time) τ on the real time t [29,31].

The stochastic time arrow can be applied to the kinetic equations (7) and (8). Take the process $S(t)$ as a subordinator. It accounts for the amount of time when a micro-contact does not change its state. If $p^{(\downarrow)}(\tau)$ and $p^{(\uparrow)}(\tau)$, taken from equations (7) and (8) as probability laws of the parent process, depend now on the local time τ , then the resulting probabilities $p_\alpha^{(\downarrow)}(t)$ and $p_\alpha^{(\uparrow)}(t)$ after the subordination are determined by the integral relations

$$p_\alpha^{(\downarrow)}(t) = \int_0^\infty d\tau p_\alpha^S(t, \tau) p^{(\downarrow)}(\tau), \quad (15)$$

$$p_\alpha^{(\uparrow)}(t) = \int_0^\infty d\tau p_\alpha^S(t, \tau) p^{(\uparrow)}(\tau). \quad (16)$$

Now the relaxation of conduction $\sigma(t)$ is defined by two stochastic processes, random switching of micro-contacts and random waiting times between these events. The ratio of micro-contacts in the state “off” (\uparrow) and another in the state “on” (\downarrow) is subordinated by the process $S(t)$. In other words, the new relaxation process (Eqs. (15) and (16)) is obtained by randomizing the time clock of the continuous-time stochastic dynamics (Eqs. (7) and (8)) using the random process $S(t)$ [29,31]. The stochastic time clock has a clear physical sense. The electrical connection between the two surfaces takes place at discrete solid a-spots in random points of time.

The equation describing the present model takes the form similar to equations (7) and (8), but the derivatives of first order become fractional of order $0 < \alpha < 1$ determined by the index of the process $S(t)$. In the following, using properties of the stochastic time clock, we derive the corresponding master equation with the fractional derivative of time, along the lines of references [31–33]. Let us present equations (7) and (8) in compact form

$$\frac{d}{dt}\mathbf{p}(t) = \hat{\omega} \mathbf{p}(t), \quad (17)$$

where $\mathbf{p}(t) = [p^{(\downarrow)}(t) p^{(\uparrow)}(t)]^T$ and $\hat{\omega}$ denotes the transition rate operator:

$$\hat{\omega} = \begin{bmatrix} -\omega_{\uparrow\downarrow} & \omega_{\uparrow\downarrow} \\ \omega_{\uparrow\downarrow} & -\omega_{\uparrow\downarrow} \end{bmatrix}. \quad (18)$$

It is important to note that the operator $\hat{\omega}$ is independent of time. Equation (17) can be written in the integral form

$$\mathbf{p}(t) = \mathbf{p}(0) + \int_0^t d\tau \hat{\omega} \mathbf{p}(\tau). \quad (19)$$

The Laplace transform of equation (19) gives the relation

$$\hat{\omega} \tilde{\mathbf{p}}(s) = s\tilde{\mathbf{p}}(s) - \tilde{\mathbf{p}}(0), \quad (20)$$

where the Laplace transform \mathcal{L} is defined as:

$$\mathcal{L}\mathbf{p}(t) \equiv \tilde{\mathbf{p}}(s) = \int_0^\infty dt \exp(-st)\mathbf{p}(t). \quad (21)$$

In the Laplace space the probabilities $\mathbf{p}_\alpha(t) = [p_\alpha^{(\downarrow)}(t) p_\alpha^{(\uparrow)}(t)]^T$ (see Eqs. (15) and (16)) take the most simple form

$$\tilde{\mathbf{p}}_\alpha(s) = s^{\alpha-1} \tilde{\mathbf{p}}(s^\alpha), \quad (22)$$

since $\tilde{\mathbf{p}}_\alpha^S(s, \tau) = s^{\alpha-1} \exp(-\tau s^\alpha)$ [34]. When the operator $\hat{\omega}$ acts on the Laplace image $\tilde{\mathbf{p}}_\alpha(s)$ (Eq. (22)), we obtain

$$\begin{aligned} \hat{\omega} \tilde{\mathbf{p}}_\alpha(s) &= s^{\alpha-1} \hat{\omega} \tilde{\mathbf{p}}(s^\alpha) = s^{\alpha-1} (s^\alpha \tilde{\mathbf{p}}(s^\alpha) - \tilde{\mathbf{p}}(0)) \\ &= s^\alpha \tilde{\mathbf{p}}_\alpha(s) - s^{\alpha-1} \tilde{\mathbf{p}}(0). \end{aligned} \quad (23)$$

The inverse Laplace transform \mathcal{L}^{-1} of the latter expression (23) gives the abstract partial differential equation with the fractional derivative of time:

$$\mathbf{p}_\alpha(t) = \mathbf{p}(0) + {}_0D_t^{-\alpha} \hat{\omega} \mathbf{p}_\alpha(t). \quad (24)$$

Here we use the fractional Riemann-Liouville integral operator defined via the formula

$${}_0D_t^{-\alpha} f(t) = \frac{1}{\Gamma(\alpha)} \int_0^t d\tau (t-\tau)^{\alpha-1} f(\tau), \quad 0 < \alpha < 1, \quad (25)$$

with the convenient property $\mathcal{L}[{}_0D_t^{-\alpha} f(t)] = s^{-\alpha} \tilde{f}(s)$ [35]. Using equation (24) and taking into account that $\sigma(t) = \sigma_{\max} p_\alpha^{(\downarrow)}(t)$, we obtain that the deviation $\Delta\sigma(t) = \sigma(\infty) - \sigma(t)$ of the conduction $\sigma(t)$

from its steady-state value $\sigma(\infty)$ obeys the fractional differential equation

$$\Delta\sigma(t) = \Delta\sigma(0) - \omega [{}_0D_t^{-\alpha} \Delta\sigma(t)], \quad (26)$$

where $\omega = \omega_{\downarrow\uparrow} + \omega_{\uparrow\downarrow}$ is the total transition probability rate and $\sigma(\infty)$ is defined by equation (10). In equation (26), the fractional derivative on the rhs describes a process which is subordinated to the simple micro-contact switching; the subordination is defined by the α -stable waiting time distribution. By differentiating equation (26) with respect to time and with the help of the formula [35]

$$\frac{d}{dt} {}_0D_t^{-\alpha} f(t) = {}_0D_t^{1-\alpha} f(t), \quad (27)$$

it is found that

$$\frac{d}{dt} \Delta\sigma(t) = -\tau_r^{-\alpha} {}_0D_t^{1-\alpha} \Delta\sigma(t), \quad (28)$$

where $\tau_r = \omega^{-1/\alpha} = (\omega_{\downarrow\uparrow} + \omega_{\uparrow\downarrow})^{-1/\alpha}$. Equation (28) is an integro-differential equation. The Riemann-Liouville operator ${}_0D_t^{1-\alpha}$ introduces a convolution integral with the power-law kernel $M(t) \propto t^{\alpha-2}$. The parameter τ_r may be interpreted as a generalized relaxation time. Indeed, the solution of equation (28) can be expressed in terms of the Mittag-Leffler function E_α of order α via [35,36]

$$\Delta\sigma(t) = \Delta\sigma(0) E_\alpha \left[-\left(\frac{t}{\tau_r} \right)^\alpha \right]. \quad (29)$$

Let us briefly describe the algorithm used in our numerical simulation. At each Monte Carlo step one lattice site is selected at random, and one of the two possible transitions between the two different states of the micro-contact is chosen at random. The choice of the transition from the state “off” to the state “on” occurs with probability $p_{\downarrow\uparrow}$, and from the state “on” to the state “off” with probability $p_{\uparrow\downarrow}$. The transition probabilities obey the normalization condition $p_{\downarrow\uparrow} + p_{\uparrow\downarrow} = 1$. When the attempted process is an “off” \rightarrow “on” transition, and if randomly chosen micro-contact is in the “off” state, its state switches from “off” to “on”. On the contrary, if randomly chosen micro-contact is in the “on” state the attempt is abandoned. When the attempted process is an “on” \rightarrow “off” transition, and provided that the selected micro-contact is in the “on” state, its state is changed from the “on” to “off”. Otherwise, we reject the switching trial. Switching processes at micro-contacts are assumed to happen instantaneously or at least in negligible time.

The random time τ between the successive micro-contact closing/opening attempts is extracted from a residence time distribution $\psi(\tau)$. We assume that the waiting-time intervals T_i between single microscopic jumps “on” (\downarrow) \leftrightarrow “off” (\uparrow) of the micro-contacts belong to the strict domain of attraction of an α -stable distribution ($0 < \alpha < 1$) [17,28]. In that case, the probability that T_i is greater than some number $t > 0$ (tail probability) is asymptotically a power law, i.e. $P(T_i > t) \propto t^{-\alpha}$ as $t \rightarrow \infty$ [28]. Accordingly, decreasing of the parameter α in the range

$(0, 1)$ increases the contribution of long waiting-time intervals T_i during the relaxation process. A suitable possible choice for a residence time distribution $\psi(\tau)$ is the Mittag-Leffler distribution defined by

$$\psi(\tau) = -\frac{d}{d\tau}E_\alpha(-(\tau/\nu)^\alpha), \quad (30)$$

where E_α is the Mittag-Leffler function of order $\alpha \in (0, 1)$ and the constant ν is the time-scaling parameter. The basic role of the Mittag-Leffler waiting time probability density in the time fractional continuous time random walk (CTRW) has become well known by the seminal paper of Hilfer and Anton [37]. The probability density $\psi(\tau)$ for the waiting times can be numerically calculated by the series expansion (3). This method produces a pointwise representation of the density on a finite interval. Random numbers can then be produced by rejection, most efficiently with a look-up table and interpolation. More convenient is the following inversion formula by Kozubowski and Rachev [38,39]:

$$\tau = -\nu \ln u \left(\frac{\sin(\alpha\pi)}{\tan(\alpha\pi v)} - \cos(\alpha\pi) \right)^{1/\alpha}, \quad (31)$$

where $u, v \in (0, 1)$ are independent uniform random numbers, ν is the scale parameter, and τ is a Mittag-Leffler random number. For $\alpha = 1$, equation (31) reduces to the inversion formula for the exponential distribution, i.e. $\tau = -\nu \ln u$. In each computational step the time t and the conductance σ are updated, $t \rightarrow t + \tau$ and $\sigma \rightarrow \sigma + \Delta\sigma$, where $\Delta\sigma \in \{\pm\sigma^{(c)}, 0\}$. Reiterating this algorithm, the full conductance growth above the initial value $\sigma(0) = \sigma_{\max}N^{(l)}(t=0)/N$ to the steady-state limit $\sigma(\infty)$ (Eq. (10)) can be computed.

The time-scaling parameter ν in equation (31) is calculated using the procedure detailed in references [40,41]. The quantities $\omega_{\downarrow\uparrow} = (p_{\downarrow\uparrow}/N)\nu^{-\alpha}$ and $\omega_{\uparrow\downarrow} = (p_{\uparrow\downarrow}/N)\nu^{-\alpha}$ in the fractional kinetic equation (28) are referred to as the fractional “off” \rightarrow “on” and “on” \rightarrow “off” rates. Using the normalization condition for the transition probabilities, i.e. $p_{\downarrow\uparrow} + p_{\uparrow\downarrow} = 1$, one obtains that

$$p_{\downarrow\uparrow} = \frac{\omega_{\downarrow\uparrow}}{\omega_{\downarrow\uparrow} + \omega_{\uparrow\downarrow}}, \quad p_{\uparrow\downarrow} = \frac{\omega_{\uparrow\downarrow}}{\omega_{\downarrow\uparrow} + \omega_{\uparrow\downarrow}}, \quad (32)$$

and

$$\nu = (N(\omega_{\downarrow\uparrow} + \omega_{\uparrow\downarrow}))^{-1/\alpha}. \quad (33)$$

In that case, the results of simulations are independent of the number of micro-contacts in the system. The fractional rates can be chosen as

$$\omega_{\downarrow\uparrow} = \omega \frac{1}{1+\gamma}, \quad \omega_{\uparrow\downarrow} = \omega \frac{\gamma}{1+\gamma}, \quad (34)$$

where $\gamma = p_{\uparrow\downarrow}/p_{\downarrow\uparrow}$. We impose that the parameter $\omega > 0$ in equation (34) depends only on the micromechanical properties of the contact, i.e. ω does not depend on the injected current I and the effective gravity $g_{\text{eff}} = g \sin \theta$ (an inclination angle θ of the plane) in the experiment. In

fact, the form (34) of the fractional rates ensures that the total rate $\omega_{\downarrow\uparrow} + \omega_{\uparrow\downarrow} = \omega \neq f(\gamma)$ is independent on the parameter γ .

The crucial parameter which determines the final steady-state conductance $\sigma(\infty)$ and controls the dynamics, is the ratio $\gamma = p_{\uparrow\downarrow}/p_{\downarrow\uparrow} = \omega_{\uparrow\downarrow}/\omega_{\downarrow\uparrow}$. According to equation (10), the steady-state value of the conductivity $\sigma(\infty)$ is determined by

$$\sigma(\infty) = \sigma_{\max} \frac{1}{1+\gamma}. \quad (35)$$

The conductance $\sigma(\infty)$ is a decreasing function of the parameter $\gamma \geq 0$ and varies between 0 ($\gamma \rightarrow \infty$) and σ_{\max} ($\gamma = 0$).

It is important to note that the coefficient α is not independent as far as its functional dependence on the parameter γ is concerned. We postulate that the parameters $0 < \alpha < 1$ and $\gamma > 0$ obey a simple relation:

$$\alpha = \frac{1}{1+\gamma}. \quad (36)$$

The value of parameter α decreases monotonically from unity as a function of the parameter γ . This relationship can be justified by the following phenomenological argument. Mapping the model on to the experiment, “on” \rightarrow “off” event is associated with the opening of a micro-contact, whereas an “off” \rightarrow “on” event is associated with the closing of a micro-contact. The number of micro-contacts in the state “off” and another in the state “on” is controlled by the parameter $\gamma = p_{\uparrow\downarrow}/p_{\downarrow\uparrow}$. Higher values of the effective gravity g_{eff} mean stronger interaction between the contact surfaces, thereby reducing the possibility of termination of micro-contacts, and stimulates the process of creating new ones. Therefore, it is acceptable to suppose that increasing the effective gravity g_{eff} corresponds to reduction of the parameter γ . Consequently, equation (35) indicates that the steady-state value of the conductivity $\sigma(\infty)$ increases with the increasing of the effective gravity g_{eff} . Furthermore, from equation (36) it follows that higher values of effective gravity are consistent with the greater values of the parameter α . Increasing of the parameter α in the range $(0, 1)$ decreases the contribution of long waiting-time intervals T_i during the relaxation process, because $P(T_i > t) \propto t^{-\alpha}$ as $t \rightarrow \infty$ [28]. This causes that the relaxation dynamics gets faster when the effective gravity g_{eff} increases, in accordance with our experiment. Analogously, in the present model, parameter γ has higher values for the lower values of effective gravity g_{eff} . In addition, decreasing of the parameter α (Eq. (36)) increases the contribution of long waiting-time intervals T_i during the relaxation process. Accordingly, evolution of the conductivity $\sigma(t)$ toward saturation value takes place on much wider time scale when the effective gravity g_{eff} decreases, which is consistent with the results of the experiment. Now it can be concluded that the parameter γ within a model plays a role similar to that of the intensity of effective gravity g_{eff} in real experiments.

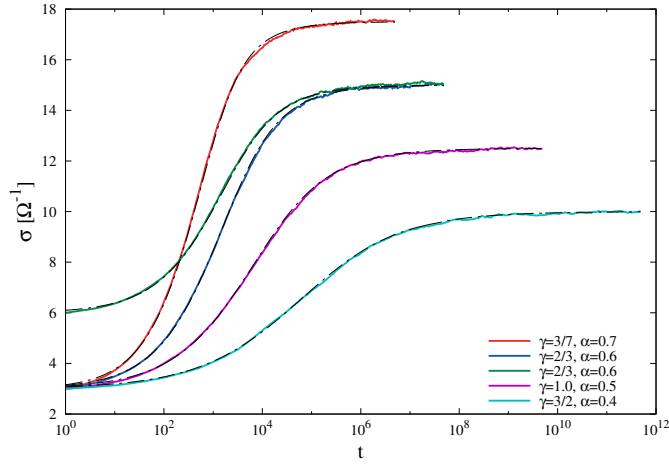


Fig. 9. Temporal evolution of the conduction $\sigma(t)$ obtained through Monte-Carlo simulations (solid lines) and analytically (dashed lines) for various values of parameter $\gamma = 3/7, 2/3, 1, 3/2$. Two curves, for the same value of $\gamma = 2/3$, demonstrate that the same steady-state will be reached by the system from any initial configuration.

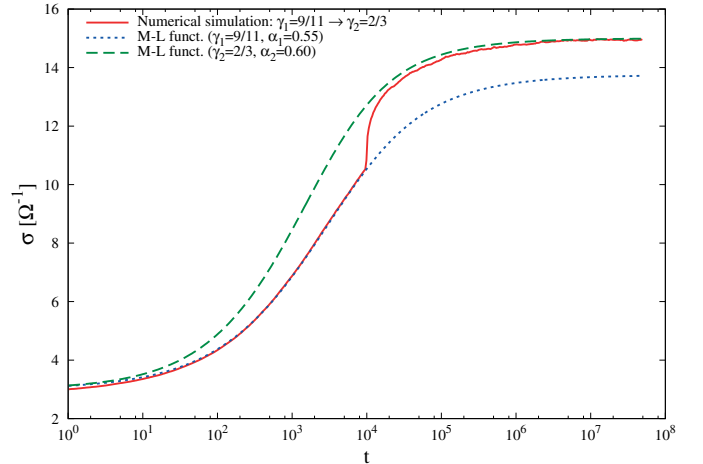
The growth of a generalized relaxation time τ_r with γ can be accurately described by the exponential law:

$$\tau_r = \tau_0 \exp(\gamma_0 \cdot \gamma). \quad (37)$$

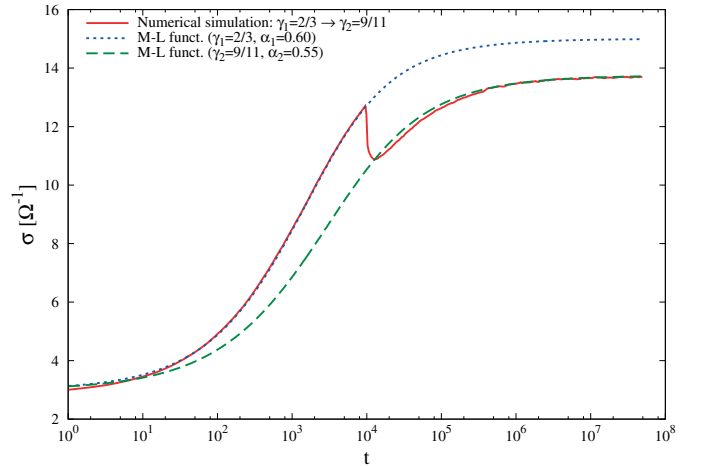
Indeed, inserting expressions $\gamma_0 = \ln(1/\omega) \neq f(\gamma)$ and $\tau_0 = 1/\omega \neq f(\gamma)$ into equation (37), and eliminating γ with the help of relation (36), we can obtain the expression for the generalized relaxation time, $\tau_r = \omega^{-1/\alpha}$ (see Eq. (28)).

Now, we present and discuss numerical results regarding the temporal evolution of the conductivity $\sigma(t)$. All numerical simulations were performed on a system of $N = 25$ micro-contacts. The parameter ω was chosen to be $\omega = 10^{-2}$. In order to sufficiently diminish statistical fluctuations, it is necessary to average over many independent runs for each value of the parameter γ . Therefore, curves of the $\sigma(t)$ relaxation reported here are averages of 10^4 independent simulations. A detailed description for the computation of the averages can be found in reference [40].

Variation of the conductance $\sigma(t)$ with time for several values of parameter γ is presented in Figure 9. We have observed that the relaxation of the conductance gets slower when the parameter γ increases. The simulation curves are in a good qualitative agreement with our experimental data, since the parameter γ has higher values for lower values of the effective gravity g_{eff} . Actually, for small values of the effective gravity we obtain higher values for the relaxation times τ and lower values of the asymptotic conductance $\sigma(\infty)$. In the same figure, the relaxation curves obtained analytically by equation (29) are also given, demonstrating that the Mittag-Leffler law (29) is excellently obeyed in our simulations. For very small values of γ , i.e. for high values of g_{eff} , there is a rapid approach to the asymptotic conductance $\sigma(\infty)$, and consequently the parameter α reaches a value close to 1 (see Eq. (36)). Since $E_\alpha[-(t/\tau_r)^\alpha] \rightarrow \exp(-t/\tau_r)$ when $\alpha \rightarrow 1$,



(a)



(b)

Fig. 10. Time evolution of the conductance $\sigma(t)$ when the parameter γ is switched (a) from $\gamma_1 = 9/11$ ($\alpha_1 = 0.55$) to $\gamma_2 = 2/3$ ($\alpha_2 = 0.60$) and (b) from $\gamma_1 = 2/3$ ($\alpha_1 = 0.60$) to $\gamma_2 = 9/11$ ($\alpha_2 = 0.55$), at a time $t_w = 10^4$ (solid curves). The dotted and dashed curves, obtained analytically by equation (29), correspond to the processes at constant γ_1 and γ_2 .

the slow relaxation feature disappears in the regime of strong external forces.

Next we show that the proposed model reproduces qualitatively the rapid variation of the electrical conductivity $\sigma(t)$ of granular packing induced by the abrupt change of the effective gravity $g_{\text{eff}} = g \sin \theta$ (see Fig. 4). Since the parameter γ within a model plays a role similar to that of the intensity of the effective gravity g_{eff} in our experiment, we simulate the abrupt change of g_{eff} as an instantaneous change of the parameter γ in our model. Figure 10 shows a typical change of the electrical conductivity in our model after an abrupt change of the parameter γ . In Figure 10a the parameter γ is switched from $\gamma_1 = 9/11$ ($\alpha_1 = 0.55$) to $\gamma_2 = 2/3$ ($\alpha_2 = 0.60$) at $t_w = 10^4$. We observe that after the transient interval, the rapid growth of $\sigma(t)$ ceases and there is a crossover to the “normal” behavior, with relaxation rate becoming

the same as in the case of constant value of parameter γ . When $\gamma = p_{\downarrow\downarrow}/p_{\downarrow\uparrow}$ is abruptly lowered, the first effect is that the system tends to decrease the fraction of opened micro-contacts, so that conductance becomes larger. Therefore the rate of conductivity growth increases with respect to the unperturbed case. At larger times, however, the relaxation of $\sigma(t)$ is slowed down by the creation of smaller fraction of the micro-contacts that is available for transition from the state “off” to the state “on”. In Figure 10b we show the response of the system to instantaneous shift of parameter γ from $\gamma_1 = 2/3$ ($\alpha_1 = 0.60$) to $\gamma_2 = 9/11$ ($\alpha_2 = 0.55$) at a time $t_w = 10^4$. We observe an effect opposite to the previous case, i.e. we find that the conductance $\sigma(t)$ drops immediately following t_w . Both numerical results are qualitatively consistent with our experimental results shown in Figure 4.

5 Concluding remarks

We have reported experiments on the electrical conductivity in 2D packings of metallic disks at fixed injected current of $I = 1$ mA. This work provides experimental and theoretical additions to the studies of references [14,15] mostly carried out in the regime of higher currents ($I > 10$ mA). The scenario of the evolution of the conductance depends on both the injected current and external forces acting on the packing. In this paper, we have attempted to give some insights into the mechanisms by which granular materials handle slow relaxation of electrical conductivity in the regime of very low injected currents and without external load.

We have experimentally investigated the conductance of 2D packings of metallic disks for different values of the effective gravity g_{eff} . We have shown that evolution of the conductivity $\sigma(t)$ toward saturation value takes place on much wider time scale when the effective gravity g_{eff} decreases. We have fitted the time dependences of the conductance $\sigma(t)$ with the Mittag-Leffler function (1). The characteristic timescale τ (Eq. (1)) is found to grow when the effective gravity g_{eff} decreases. By changing both the distance between the electrodes and the number of grains in the packing, it was shown that the long-term resistance decay observed in the experiment is not related to large force chain rearrangements, but to individual micro-contacts between two disks that rearrange. Hence, this long-term decay seems to be related to the enhancement of the contacts themselves. The behavior of granular material is thus completely different from a metallic bulk material. When the current is switched on, the metallic wire produces heat. This change in temperature makes the electrical conductance decrease. On the other hand, in the case of granular material, the opposite effect occurs. The local micro-contact rearrangements at each grain influence the conduction by increasing it. Consequently, in the case of granular material with weak links between conductive grains, electrical measurements have to be carefully implemented. The intensity of the injected current, external load and surface state of grains are seen to be relevant parameters.

These results were used as a basis for building of a dynamic model of the electric contact between two grains which is composed of a large number of micro-contacts. Actually, we have developed an artificial, but instructive model of a contact which can be regarded as a very simple picture of the interface between two metallic grains. We impose that the micro-contacts at the interface switch stochastically between the two states (“on” and “off”). By appropriately choosing this random process, one can provide the essential ingredients in our model to reproduce the slow relaxation of the electrical conductivity and mimic the rapid variation of the conductance $\sigma(t)$ induced by the abrupt change of the effective gravity g_{eff} . We think that the success of the model in emulating the experiments indicates that the dominant physical mechanisms have been correctly identified. Even though the model is simple enough as to be analytically tractable, the theoretical results are corroborated by numerical simulations of the corresponding stochastic fractional processes.

This work was supported by the Ministry of Education, Science, and Technological Development of the Republic of Serbia under projects ON171017, III45016, and by the European Commission under H2020 project VI-SEEM, Grant No. 675121. Numerical simulations were run on the PARADOX supercomputing facility at the Scientific Computing Laboratory of the Institute of Physics Belgrade.

Author contribution statement

Study conception and design: S.B. Vrhovac and Z.M. Jaksic; Acquisition of data: Z.M. Jaksic, M. Cvetkovic, and J.R. Scepanovic; Analysis and interpretation of experimental data: Z.M. Jaksic, M. Cvetkovic, and J.R. Scepanovic; Development of the theoretical formalism and analytic calculations: S.B. Vrhovac, Lj. Budinski-Petkovic, and I. Loncarevic; Development of the numerical simulations: S.B. Vrhovac, Lj. Budinski-Petkovic, and I. Loncarevic; Drafting of manuscript: S.B. Vrhovac and Lj. Budinski-Petkovic; Critical revision: S.B. Vrhovac, Lj. Budinski-Petkovic, and I. Loncarevic.

References

1. R. Holm, *Electric Contacts: Theory and Applications*, 4th edn. (Springer-Verlag, Berlin/Heidelberg, 1967)
2. V. Da Costa, Y. Henry, F. Bardou, M. Romeo, K. Ounadjela, Eur. Phys. J. B **13**, 297 (2000)
3. B.F. Toler, R.A. Coutu Jr., J.W. McBride, J. Micromech. Microeng. **23**, 103001 (2013)
4. E. Branly, C. R. Acad. Sci. **280**, 785 (1890)
5. S. Dorbolo, M. Ausloos, N. Vandewalle, Phys. Rev. E **67**, 040302 (2003)
6. E. Falcon, B. Castaing, C. Laroche, Europhys. Lett. **65**, 186 (2004)
7. E. Falcon, B. Castaing, Am. J. Phys. **73**, 302 (2005)
8. S. Dorbolo, N. Vandewalle, Traffic Granul. Flow **5**, 521 (2005)
9. P. Bèquin, V. Tourant, Granul. Matter **12**, 375 (2010)

10. M. Creyssels, S. Dorbolo, A. Merlen, C. Laroche, B. Castaing, E. Falcon, Eur. Phys. J. E **23**, 255 (2007)
11. E. Falcon, B. Castaing, M. Creyssels, Eur. Phys. J. B **38**, 475 (2004)
12. N. Vandewalle, C. Lenaerts, S. Dorbolo, Europhys. Lett. **53**, 197 (2001)
13. D. Bonamy, L. Laurent, Ph. Claudin, J.-Ph. Bouchaud, Europhys. Lett. **51**, 614 (2000)
14. S. Dorbolo, M. Ausloos, N. Vandewalle, M. Houssab, J. Appl. Phys. **94**, 7835 (2003)
15. J.J. Lee, C.W. Lee, I. Yu, Y.K. Jung, J. Lee, J. Phys.: Condens. Matter **19**, 356202 (2007)
16. R. Hilfer, J. Non-Cryst. Solids **305**, 122 (2002)
17. M.M. Meerschaert, H.-P. Scheffler, J. Appl. Probab. **41**, 623 (2004)
18. A.A. Stanislavsky, Phys. Rev. E **61**, 4752 (2000)
19. R. Metzler, J. Klafter, Phys. Rep. **339**, 1 (2000)
20. G.M. Zaslavsky, Phys. Rep. **371**, 461 (2002)
21. T. Aste, J. Phys.: Condens. Matter **17**, S2361 (2005)
22. E.W. Weisstein, Mittag-Leffler function, From MathWorld – A Wolfram Web Resource (2017), <http://mathworld.wolfram.com/Mittag-LefflerFunction.html>
23. D. Howell, R.P. Behringer, C. Veje, Phys. Rev. Lett. **82**, 5241 (1999)
24. M. Muthuswamy, A. Tordesillas, in *Proceedings of the 10th ASCE Aerospace Division International Conference on Engineering, Construction and Operations in Challenging Environments (Earth & Space 2006)*, edited by R.B. Malla, W.K. Binienda, A.K. Maji (Aerospace Division of the American Society of Civil Engineers, Reston, VA, 2006), p. 33
25. M. Muthuswamy, A. Tordesillas, JSTAT **P09003** (2006)
26. A. Modaresi, S. Boufellouh, P. Evesque, Chaos **9**, 523 (1999)
27. Z.M. Jakšić, J.R. Šćepanović, I. Lončarević, Lj. Budinski-Petković, S.B. Vrhovac, A. Belić, Phys. Rev. E **90**, 062208 (2014)
28. A. Janicki, A. Weron, Stat. Sci. **9**, 109 (1994)
29. M. Magdziarz, K. Weron, Physica A **367**, 1 (2006)
30. F. Mainardi, Chaos Solitons Fract. **7**, 1461 (1996)
31. A.A. Stanislavsky, Phys. Rev. E **67**, 021111 (2003)
32. A.A. Stanislavsky, Chaos Solitons Fract. **34**, 51 (2007), in Search of a Theory of Complexity
33. Aleksander Stanislavsky, Karina Weron, Aleksander Weron, Commun. Nonlinear Sci. Numer. Simul. **24**, 117 (2015)
34. A.A. Stanislavsky, Acta Phys. Polonica B **34**, 3649 (2003)
35. F. Mainardi, R. Gorenflo, J. Comput. Appl. Math. **118**, 283 (2000)
36. R.K. Saxena, A.M. Mathai, H.J. Haubold, Physica A **344**, 657 (2004)
37. R. Hilfer, L. Anton, Phys. Rev. E **51**, R848 (1995)
38. T.J. Kozubowski, S.T. Rachev, J. Comput. Anal. Appl. **1**, 177 (1999)
39. D. Fulger, E. Scalas, G. Germano, Phys. Rev. E **77**, 021122 (2008)
40. E. Heinsalu, M. Patriarca, I. Goychuk, G. Schmid, P. Hänggi, Phys. Rev. E **73**, 046133 (2006)
41. E. Heinsalu, M. Patriarca, I. Goychuk, P. Hänggi, J. Phys.: Condens. Matter **19**, 065114 (2007)

Particle morphology effects in random sequential adsorption

Lj. Budinski-Petković,¹ I. Lončarević,¹ D. Dujak,² A. Karač,³ J. R. Šćepanović,⁴ Z. M. Jakšić,⁴ and S. B. Vrhovac^{4,*}

¹*Faculty of Engineering, Trg D. Obradovića 6, Novi Sad 21000, Serbia*

²*Faculty of Metallurgy and Materials, University of Zenica, Zenica, Bosnia and Herzegovina*

³*Polytechnic Faculty, University of Zenica, Zenica, Bosnia and Herzegovina*

⁴*Scientific Computing Laboratory, Center for the Study of Complex Systems, Institute of Physics Belgrade, University of Belgrade, Pregrevica 118, Zemun 11080, Belgrade, Serbia*

(Received 12 October 2016; published 13 February 2017)

The properties of the random sequential adsorption of objects of various shapes on a two-dimensional triangular lattice are studied numerically by means of Monte Carlo simulations. The depositing objects are formed by self-avoiding lattice steps, whereby the size of the objects is gradually increased by wrapping the walks in several different ways. The aim of this work is to investigate the impact of the geometrical properties of the shapes on the jamming density θ_j and on the temporal evolution of the coverage fraction $\theta(t)$. Our results suggest that the order of symmetry axis of a shape exerts a decisive influence on adsorption kinetics near the jamming limit θ_j . The decay of probability for the insertion of a new particle onto a lattice is described in a broad range of the coverage θ by the product between the linear and the stretched exponential function for all examined objects. The corresponding fitting parameters are discussed within the context of the shape descriptors, such as rotational symmetry and the shape factor (parameter of nonsphericity) of the objects. Predictions following from our calculations suggest that the proposed fitting function for the insertion probability is consistent with the exponential approach of the coverage fraction $\theta(t)$ to the jamming limit θ_j .

DOI: [10.1103/PhysRevE.95.022114](https://doi.org/10.1103/PhysRevE.95.022114)

I. INTRODUCTION

Understanding various aspects of random sequential adsorption (RSA) has a great scientific and industrial importance as it has been linked to a wide range of applications in biology, nanotechnology, device physics, physical chemistry, and materials science [1–4]. Depositing objects range in size from micrometer scale down to nanometer scale, and depending on the application in question, the objects could be colloidal particles, polymer chains, globular proteins, nanotubes, DNA segments, or general geometrical shapes, such as disks, polygons, etc.

The RSA model adsorption process considers sequential addition of particles on the n -dimensional substrate such that at each time step only one particle is added on the substrate at a randomly selected position. During the process of addition, newly added particles are forbidden from overlapping with the already adsorbed particles, and any attempt of adsorption resulting in an overlap is rejected. The adsorbed particles are permanently fixed at their spatial positions so that they affect the geometry of all later placements. This leads to slowing of the rate of adsorption due to unavailability of the surface for further addition. The most common parameter to characterize the kinetic properties of a deposition process is the coverage $\theta(t)$, defined as the ratio of the number of occupied sites at time t and the total number of sites. Due to the blocking of the substrate area by the already randomly adsorbed particles, at large times the coverage $\theta(t)$ approaches the jammed-state value θ_j , where only gaps too small to fit new particles are left in the monolayer.

The RSA models are broadly classified into continuum models and lattice models on the basis of the nature of the

substrate. The long-term behavior of the coverage fraction $\theta(t)$ is known to be asymptotically algebraic for continuum systems [5–8] and exponential for lattice models [9–12]. For the latter case the approach of the coverage fraction $\theta(t)$ to its jamming limit θ_j is given by the time dependence:

$$\theta_j - \theta(t) \sim \exp(-t/\sigma), \quad (1)$$

where parameters θ_j and σ depend on the shape, orientational freedom of depositing objects, and the dimensionality of the substrate [11,12].

An important issue in RSA is the influence of the shape of depositing objects on kinetics of irreversible deposition and on the morphological characteristics of coverings. RSA of many different geometric objects has been studied for both continuum and lattice models in order to determine the significance of particle anisotropy in formation of the jammed-state coverings. For this purpose, the jamming coverings generated by RSA on continuous substrates have been analyzed for depositing particles of various shapes, such as spherocylinders and ellipsoids [13,14], rectangles [15,16], starlike particles [17,18], and polymers [19,20]. Results obtained for anisotropic particles show that jamming coverage reaches its maximum when the long-to-short particle axis ratio is approximately 1.5–2.0 [13,16]. Recently Cieřla *et al.* have performed an extensive numerical simulation of the RSA of smoothed n -mers, spherocylinders, and ellipses [21–23] in order to find a shape which maximizes the jamming coverage. It is found that the highest packing fraction is obtained for ellipses having the long-to-short axis ratio of 1.85, which is the largest anisotropy among the investigated shapes.

The kinetics of the deposition process is strongly dependent on geometrical properties of the objects. For instance, Khandkar *et al.* [24] have studied RSA of zero-area symmetric angled objects on a continuum substrate for the full range

*vrhovac@ipb.ac.rs; <http://www.ipb.ac.rs/~vrhovac/>

(0° – 180°) of values of the arm angle ϕ and have observed that $\theta_j - \theta(t) \sim t^\alpha$ as expected. Value of the exponent α exhibits a crossover near $\phi = 0^\circ$ or 180° and is significantly lower in the case of the angled objects than in the case of needles.

Formation of random deposits of extended objects on discrete substrates and their properties have been extensively studied in many different contexts and using a number of different tools, including irreversible deposition [11,25,26], an adsorption-desorption model [27–29], random deposition with diffusional relaxation [30–32], and percolations [33–35].

Wang and Pandey [36] have studied the kinetics and jamming coverage in RSA of self-avoiding walk chains on a square lattice and found that the jamming coverage θ_j decreases with the chain length with a power law. They observed a crossover from a power-law variation of the coverage fraction $\theta(t)$ in the intermediate time regime to an exponential growth in the long time, especially for short chains.

Budinski and Kozmidis [11,26] have carried out extensive simulations of irreversible deposition using objects of different sizes and rotational symmetries on a square and triangular lattice. They reported that shapes with the symmetry axis of a higher order have lower values of σ [Eq. (1)], i.e., they approach their jamming limit more rapidly. This confirms the crucial role of the geometrical character of the objects in deposition dynamics.

The main goal of the present study is to extend the analysis in Ref. [11] to large collections of objects of various shapes that can be made by self-avoiding random walks on a triangular lattice. The large number of examined objects represents a good basis for testing the impact of the geometrical properties of the shapes on the jamming density θ_j and on the temporal evolution of the coverage fraction $\theta(t)$. We address the following questions regarding the influence of the shape on the rapidity of the approach to the jamming state. First, we investigate the interplay between the size and the symmetry properties of depositing shapes. This is an important question because the slowing of the dynamics in the RSA model can be understood as a consequence of steric effects that make certain insertions of particles infeasible owing to an effective high local density on the lattice. Second, we analyze whether there is some intrinsic property of the objects that, in addition to symmetry, also promotes or suppresses rare adsorption events which take place on isolated islands of connected unoccupied sites at the late times of the deposition process.

For this purpose we use the concept of the shape factor to measure the circularity of depositing objects. The shape factor (parameter of nonsphericity) was introduced by Moučka and Nezbeda [37], for tracking the change in structure as a liquid-like system approaches a disordered jammed state. Shape factor, ζ , is defined as the degree to which a particle is similar to a circle, taking into consideration the smoothness of the perimeter. This means the parameter ζ is a measurement of both the particle form and roughness. Thus, the farther away from a perfectly round and smooth circle that a particle becomes, the higher the ζ value. The shape factor is a dimensionless value. Moreover, we generalize the definition of the shape factor for planar geometric figures [see Eq. (6)] to make it applicable to the objects made by directed self-avoiding walks on the two-dimensional lattice.

In this paper the shape factor ζ is associated with the evolution of probability for the insertion of a new particle onto a lattice during the deposition process. This work provides a closer insight into the behavior of the insertion probability during the irreversible deposition of extended objects. The decay of the insertion probability is described in a broad range of the coverage θ by the product between linear and stretched exponential function for all examined objects. We discuss the fitting parameters from the proposed fitting function within the context of the shape descriptors, such as rotational symmetry and shape factor of the objects.

The paper is organized as follows. Section II describes the details of the simulations. The approach of the coverage fraction $\theta(t)$ to the jamming limit θ_j is analyzed in Sec. III A. Section III B is devoted to the analysis of the behavior of probability for the insertion of a particle onto a lattice during the deposition process. Finally, Sec. IV contains some additional comments and final remarks.

II. DEFINITION OF THE MODEL AND THE SIMULATION METHOD

The depositing objects are modeled by self-avoiding walks on the planar triangular lattice. A self-avoiding shape of length ℓ is a sequence of *distinct* vertices $(\omega_0, \dots, \omega_\ell)$ such that each vertex is a nearest neighbor of its predecessor, i.e., a walk of length ℓ covers $j = \ell + 1$ lattice sites. Starting from a dimer, size of the objects is gradually increased by wrapping the walks in several different ways. Formation of wrapping triangles T_j is shown in Table I. In a similar way, rhombuses R_j and hexagons H_j of larger sizes $j = 2, 3, \dots, 30$ are obtained by wrapping as shown in Tables II and III, respectively. In this manner, wrapping objects of larger sizes occupy all comprised sites on the lattice.

On a triangular lattice objects with a symmetry axis of first, second, third, and sixth order can be formed. Rotational symmetry of order n_s , also called n -fold rotational symmetry, with respect to a particular axis perpendicular to the triangular lattice, means that rotation by an angle of $2\pi/n_s$ does not change the object. The values of the order of symmetry axis n_s are given in Tables I–III for all wrapping triangles, rhombuses, and hexagons. We concentrate here on the influence of the order of symmetry axis of the shape on the kinetics of the adsorption process. Special attention is paid to the comparison of the results for lattice objects of different rotational symmetries but of the same number of segments.

At each Monte Carlo step a lattice site is selected at random. If the selected site is unoccupied, we fix the beginning of the walk that makes the chosen shape T_j (or R_j, H_j) at this site. Then we randomly pick one of the six possible orientations on the lattice with equal probability, start the corresponding ℓ -step walk in that direction, and search whether all successive ℓ sites are unoccupied. If so, we occupy these $j = \ell + 1$ sites and place the object. If the attempt fails, a new site and a new direction are selected at random. This scheme is usually called the conventional or standard model of RSA. The other strategy to perform an RSA, where we check all possible directions from the selected site, is named the end-on model [11]. The jamming limit is reached when no more objects can be placed in any position on the lattice. Since the local domain

TABLE I. Wrapping triangles, T_j . The colors are associated with different order n_s of the symmetry axis. For each shape, θ_j is the jamming coverage and σ is the relaxation time [Eq. (1)].



























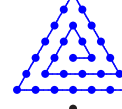


Shape (T_j)	j	n_s	σ	θ_j
	2	2	3.03	0.9141
	3	3	1.97	0.7969
	4	1	5.99	0.7741
	5	1	6.01	0.7605
	6	3	2.04	0.7210
	7	1	5.97	0.6901
	8	1	6.09	0.6993
	9	1	5.99	0.7101
	10	3	2.00	0.6816
	11	1	5.83	0.6493
	12	1	5.71	0.6624
	13	1	5.97	0.6683
	14	1	5.94	0.6816
	15	3	2.01	0.6572
	16	1	5.81	0.6263
	17	1	5.80	0.6368
	18	1	6.05	0.6445
	19	1	5.95	0.6518
	20	1	5.90	0.6633
	21	3	1.99	0.6407
	22	1	5.56	0.6119
	23	1	6.05	0.6197

TABLE I. (Continued.)

Shape (T_j)	j	n_s	σ	θ_j
	24	1	5.89	0.6286
	25	1	5.98	0.6323
	26	1	5.79	0.6406
	27	1	5.92	0.6498
	28	3	1.93	0.6286
	29	1	5.86	0.6016
	30	1	5.92	0.6079

structures for the end-on model are more dense than those of the conventional model, the jamming limit θ_j for the end-on model is slightly larger than that for the conventional model.

It is well established that correlations in RSA decay extremely fast [1,6,38]. Therefore, one can obtain high-precision results numerically on relatively small lattices, without worrying about finite-size effects [39–41] and averaging over not too many runs because the system is self-averaging. Numerical studies have shown that the finite-size effects on the lattice of size L can be neglected for object sizes $\leq L/8$ [10]. Consequently, Monte Carlo simulations are performed on a triangular lattice of size $L = 240$. Periodic boundary conditions are used in all directions. The time t is counted by the number of attempts to select a lattice site and scaled by the total number of lattice sites $N = L^2 = 57\,600$. The simulation data are averaged over 1000 independent runs for each depositing object.

III. RESULTS AND DISCUSSION

A. Particle jamming and late-stage deposition kinetics

First, we report and discuss the numerical results regarding the influence of the order of the symmetry axis of the shape on the kinetics of the deposition processes. The simulations have been performed for all wrapping triangles, rhombuses, and hexagons from Tables I–III. Figure 1 shows the plots of $\ln[\theta_j - \theta(t)]$ versus t for three wrapping triangles (T_3 , T_4 , T_6) and hexagons (H_4 , H_7 , H_{19}), and for two wrapping rhombuses

TABLE II. Wrapping rhombuses, R_j . The colors are associated with different order n_s of the symmetry axis. For each shape, θ_j is the jamming coverage and σ is the relaxation time [Eq. (1)].






























Shape (R_j)	j	n_s	σ	θ_j
	2	2	3.02	0.9141
	3	1	6.03	0.8345
	4	2	3.08	0.7591
	5	1	6.00	0.7605
	6	2	3.00	0.7299
	7	1	5.98	0.7075
	8	1	6.01	0.6956
	9	2	2.99	0.6792
	10	1	5.98	0.6706
	11	1	5.78	0.6885
	12	2	2.90	0.6716
	13	1	6.01	0.6506
	14	1	6.04	0.6531
	15	1	6.01	0.6463
	16	2	2.99	0.6428
	17	1	6.02	0.6332
	18	1	6.00	0.6439
	19	1	5.72	0.6549
	20	2	2.97	0.6416
	21	1	5.79	0.6224
	22	1	5.99	0.6258
	23	1	5.78	0.6254
	24	1	6.02	0.6226
	25	2	2.79	0.6220
	26	1	5.95	0.6126
	27	1	5.90	0.6199

TABLE II. (*Continued.*)

Shape (R_j)	j	n_s	σ	θ_j
	28	1	5.71	0.6260
	29	1	5.97	0.6349
	30	2	3.10	0.6236

(R_3 , R_6), so that it contains results for shapes of all symmetry orders. Lines with four different slopes are plotted in Fig. 1, showing the late times of the deposition process corresponding to objects of different symmetry order, $n_s = 1, 2, 3, 6$, as indicated in the legend. Following the objects formed by walks of increasing length (e.g., T_3 and T_4), we can see that objects differing in only one self-avoiding lattice step can have significantly different values of the relaxation time σ . On the other hand, for a given value of symmetry order n_s , these plots are parallel lines in the late stages of the deposition process for shapes of very different lengths (e.g., H_7 and H_{19}). This means that for a given n_s , rapidity of the approach to the jamming state is not affected by the length of the shape. Consequently, order of symmetry of the shape has an essential influence in the late times of the deposition process. To further confirm this notion, we have calculated the values of the parameter σ [Eq. (1)] from the slopes of the $\ln[\theta_j - \theta(t)]$ versus t curves in the late times of the process. Parameter σ determines how fast the lattice is filled up to the jamming coverage θ_j . The values of relaxation time σ are given in Tables I–III for all examined

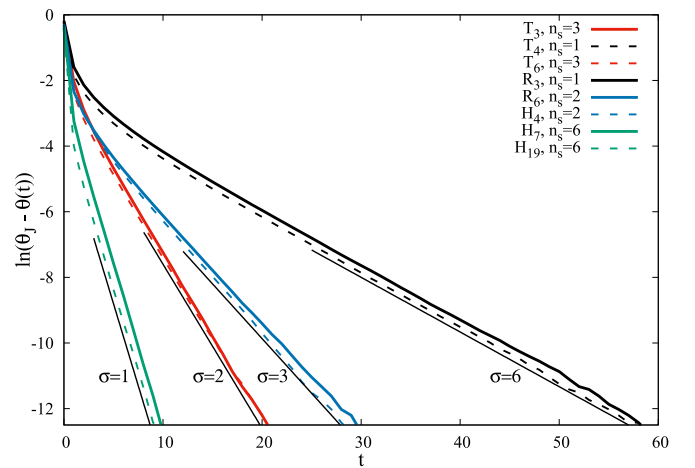


FIG. 1. Plots of $\ln(\theta_j - \theta(t))$ vs t for wrapping triangles T_3 , T_4 , T_6 , rhombuses R_3 , R_6 , and hexagons H_4 , H_7 , H_{19} from Tables I–III. The curves correspond to various values of the order of symmetry axis of the shape, n_s , as indicated in the legend. Additionally, the slanted straight lines with the slope $-1/\sigma = -1, -1/2, -1/3, -1/6$ are shown, indicating the late-time RSA behavior and are guides for the eye.

TABLE III. Wrapping hexagons, H_j . The colors are associated with different order n_s of the symmetry axis. For each shape, θ_j is the jamming coverage and σ is the relaxation time [Eq. (1)].





























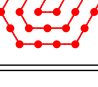
Shape (H_j)	j	n_s	σ	θ_j
	2	2	2.99	0.9141
	3	3	1.99	0.7970
	4	2	2.94	0.7591
	5	1	6.01	0.7604
	6	1	6.00	0.7347
	7	6	0.98	0.6697
	8	1	5.78	0.6923
	9	1	5.99	0.6857
	10	2	2.97	0.6813
	11	1	6.00	0.6665
	12	3	2.01	0.6508
	13	1	5.98	0.6431
	14	2	3.00	0.6457
	15	1	5.99	0.6433
	16	1	6.00	0.6623
	17	1	6.05	0.6472
	18	1	6.01	0.6367
	19	6	1.02	0.6147
	20	1	6.05	0.6163
	21	1	5.79	0.6352
	22	1	6.01	0.6265
	23	1	6.03	0.6293
	24	2	2.98	0.6327

TABLE III. (Continued.)

Shape (H_j)	j	n_s	σ	θ_j
	25	1	6.01	0.6204
	26	1	5.94	0.6190
	27	3	2.01	0.6136
	28	1	5.98	0.6057
	29	1	5.76	0.6099
	30	2	2.83	0.6119

objects. Approximate values of the parameter σ for the four classes of objects of different symmetry are found to be the following:

- $\sigma \simeq 6.0$ for the shapes with a symmetry axis of first order, $n_s = 1$;
- $\sigma \simeq 3.0$ for the shapes with a symmetry axis of second order, $n_s = 2$;
- $\sigma \simeq 2.0$ for the shapes with a symmetry axis of third order, $n_s = 3$;
- $\sigma \simeq 1.0$ for the shapes with a symmetry axis of sixth order, $n_s = 6$.

This means that the approach to the jamming limit is faster for more regular and symmetric shapes. At large times, adsorption events take place on islands of unoccupied sites. The individual islands act as selective targets for specific deposition events. In other words, there is only a restricted number of possible orientations in which an object can reach a vacant location, provided the location is small enough. For a shape of a higher order of symmetry n_s , there is a greater number of possible orientations for deposition into a selective target on the lattice. Hence, the increase of the order of symmetry of the shape enhances the rate of single particle adsorption. This shortens the mean waiting time between consecutive deposition events and the approach to the jamming state is faster.

Figures 2(a)–2(c) show the dependence of the jamming coverage θ_j on the number j of sites covered by an object for wrapping triangles (a), rhombuses (b), and hexagons (c). Numerical values of the obtained jamming coverages θ_j are also given in Tables I–III for all examined wrapping shapes.

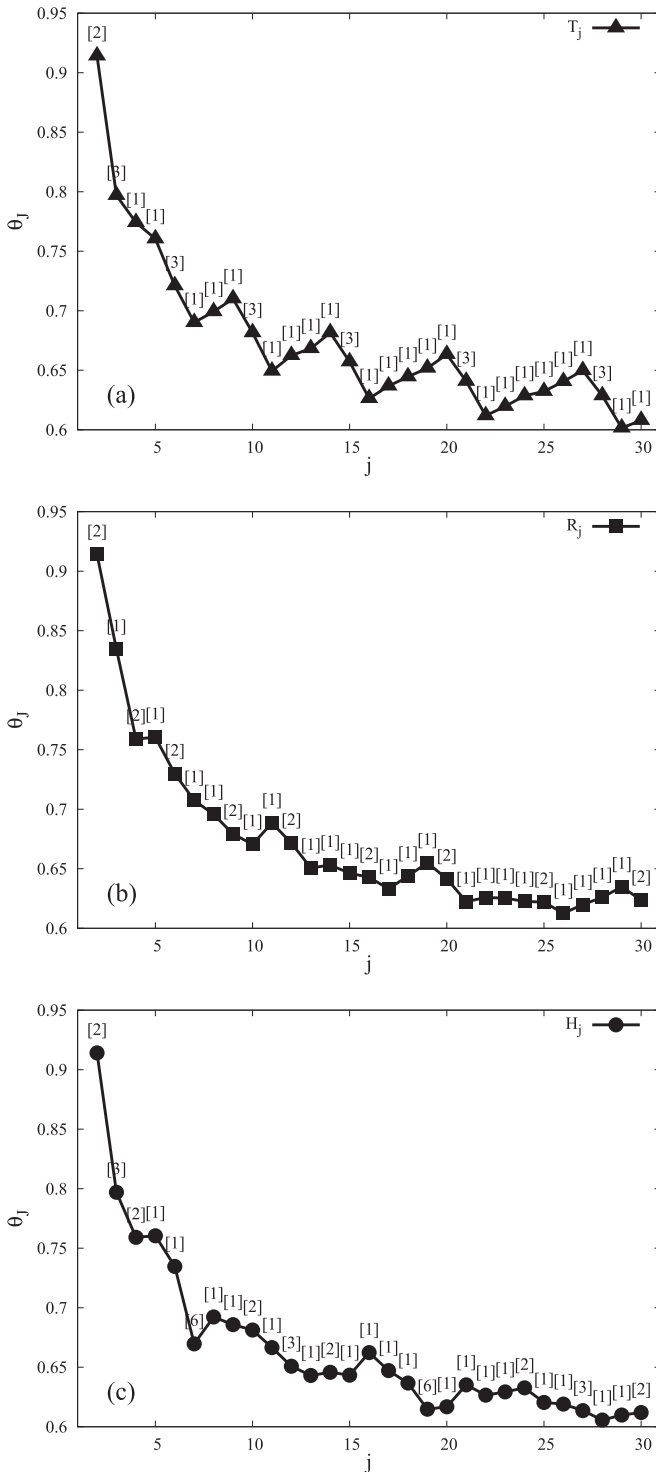


FIG. 2. Jamming coverages θ_j for all wrapping (a) triangles T_j , (b) rhombuses R_j , and (c) hexagons H_j , from Tables I–III. Here $j = 2, \dots, 30$ denotes the number of sites covered by an object. Numerical values of the symmetry order n_s of the shapes are given in the square brackets above the corresponding plot symbols.

From Fig. 2 it is evident that for small values of $j \lesssim 7$, jamming coverages θ_j decrease very rapidly with the size of the objects. A noticeable drop in the jamming coverage θ_j is thus a clear consequence of the enhanced frustration of the spatial

adsorption. However, adding a single node to large objects does not result in a significant increasing in their size. Therefore, changing the shape of the large objects has considerably more influence on the jamming density than increasing the object size. For example, jamming coverages for objects T_{11} and T_{27} from Table I are almost identical, although they are of different sizes. The presented results in Fig. 2 also suggest that there is no correlation between the order of symmetry axis n_s of the shape and the corresponding values of the jamming density θ_j . It is interesting that, for the wrapping hexagons [Fig. 2(c)], the jamming density θ_j reaches a local minimum for the most regular hexagons H_7 and H_{19} with symmetry axis of sixth order, $n_s = 6$, while the jamming density θ_j for object H_{16} of low symmetry order, $n_s = 1$, is greater than θ_j for the wrapping hexagons that cover more than $j = 11$ sites.

In order to gain a better insight into the complex kinetics of the adsorption processes of wrapping objects it is useful to analyze in particular the temporal evolution of probability for the insertion of a new particle onto a lattice. Insertion probability p_j for the object j at time t is calculated from the expression

$$p_j = 1 - \frac{c_j}{N}, \quad j = 1, 2, 3, \dots, 30, \quad (2)$$

where

$$c_j = \frac{1}{6} (6n_0^{(j)} + 5n_1^{(j)} + 4n_2^{(j)} + 3n_3^{(j)} + 2n_4^{(j)} + n_5^{(j)}). \quad (3)$$

Here $n_k^{(j)}$ is the total number of sites at which the beginning of the walk that makes the shape j can be placed, whereby the deposited object j at each available site can be oriented in k ($k = 0, \dots, 5$) different ways. We emphasize that the first step determines the orientation k of the object. In Eq. (2), N denotes the total number of lattice sites, $N = L^2$. The quantities $n_k^{(j)}$, $k = 0, 1, 2, 3, 4, 5$ are calculated numerically from the simulation data. Let us remark that a different choice of the head of the object (the beginning of the walk) does not change the value of the coefficient c_j . We have verified that usage of a different head for all examined objects gives quantitatively the same results for coefficients c_j and probabilities p_j .

Below we try to characterize quantitatively the time and density dependence of the insertion probability p_j during irreversible deposition of wrapping triangles T_j , rhombuses R_j , and hexagons H_j . In Fig. 3(a) the coefficients c_j [Eq. (3)] are plotted as a function of the number n of randomly deposited objects for all wrapping triangles T_j (Table I). Numerical simulations for wrapping rhombuses R_j and hexagons H_j (Tables II and III) produce qualitatively similar results for the evolution of coefficients $c_j(n)$ during the deposition process. At very early times of the process, deposited objects do not “feel” the presence of the others, and $c_j(n) = n c_j(1)$ for sufficiently low densities θ . Therefore, at the very early times, the plot of the coefficients c_j with respect to n is linear on a double logarithmic scale with the slope 1. At higher densities, “excluded volumes” for deposited objects begin to overlap, leading to slowing of the linear growth of the coefficients c_j with n . In Fig. 3(b) we show the behavior of coefficients $c_j(\theta)$ in the late stages of deposition process. As can be seen from Fig. 3(b), the final value $N = L^2 = 57600$ of coefficients c_j is reached when the coverage θ of the system approaches the jammed-state value θ_j . The curves $c_j(\theta)$ shift to lower

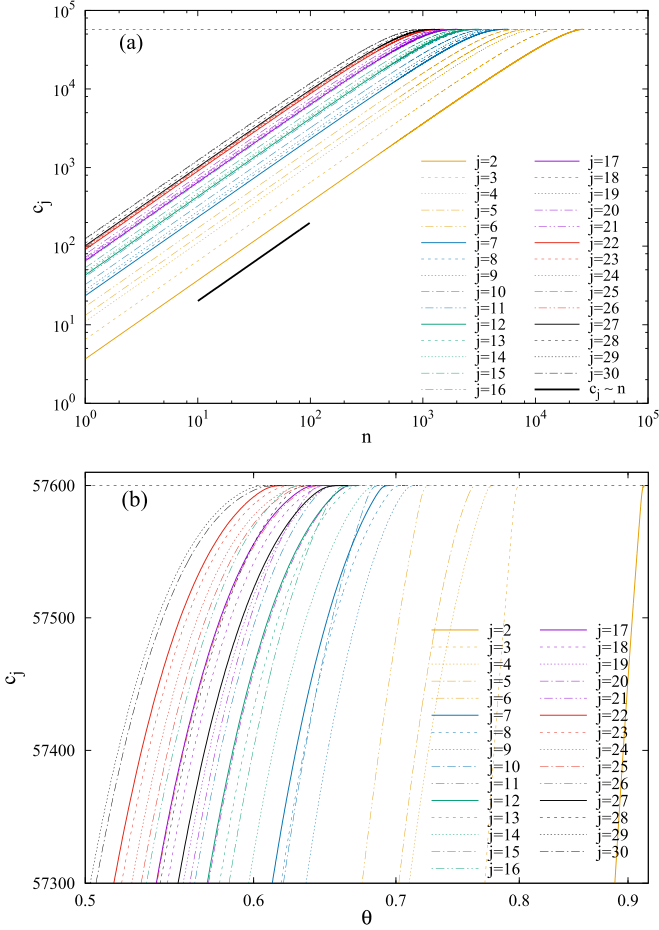


FIG. 3. The coefficients c_j [Eq. (3)] as a function (a) of the number n of deposited objects, and (b) of the coverage θ , in the late stage of the deposition process, for all wrapping triangles T_j (Table I). The horizontal line represents the final value $N = L^2 = 57600$ of the coefficients c_j that is reached when the coverage θ approaches to the jamming limit θ_j . The solid black line has slope 1 and is a guide for the eye.

densities θ when the object size increases. Some of the lines $c_j(\theta)$ intersect with the other ones in the late stage of the process when the influence of the shape on the densification kinetics becomes very important.

The results for the insertion probability p_j are shown in Fig. 4 for the same wrapping objects as in Fig. 1. Insertion probability p_j is a monotonically decreasing function of the coverage fraction θ for all the shapes. When the coverage θ approaches the jamming limit θ_j , the probability p_j decreases very rapidly with θ and vanishes at θ_j .

B. Properties of the insertion probability: Role of rotational symmetry of the shapes

In the following, we try to find a universal functional type that describes the decay of the insertion probability p_j for all shapes in a broad range of the coverage θ . In addition, the proposed function $p_j = f(\theta)$ should be consistent with the exponential approach of the coverage fraction $\theta(t)$ to the jamming limit θ_j [Eq. (1)]. Looking for a function that gives the best fit to probability p_j , we have tried a wide set of

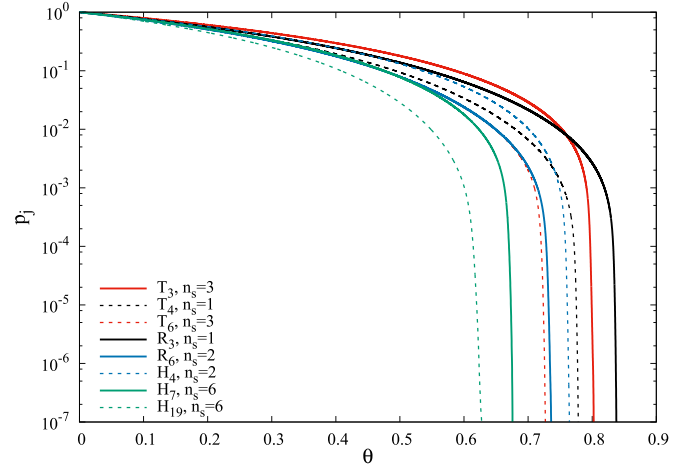


FIG. 4. Shown here is the insertion probability p_j vs the coverage θ for triangles T_3 , T_4 , T_6 , rhombuses R_3 , R_6 , and hexagons H_4 , H_7 , H_{19} from Tables I–III.

phenomenological fitting functions for relaxation processes in many complex disordered systems [42]. The best agreement with our simulation data was obtained by the fitting function of the form

$$\begin{aligned} p_j(\theta) &= A \left(1 - \frac{\theta}{\theta_j}\right) \exp(-\lambda_1 \theta^{\lambda_2}) \\ &= A \left(1 - \frac{\theta}{\theta_j}\right) \exp \left[- \left(\frac{\theta}{\theta^{(c)}} \right)^{\lambda_2} \right], \end{aligned} \quad (4)$$

where A , λ_1 , and λ_2 are the fitting parameters, and

$$\theta^{(c)}(j) = [\lambda_1(j)]^{(-1/\lambda_2(j))}. \quad (5)$$

Parameter $\theta^{(c)}(j)$ determines the characteristic density scale, and exponent λ_2 measures the decay rate of the probability $p_j(\theta)$ on this scale. Interestingly, Ludewig *et al.* [43] have proposed that the decrease of the grain mobility with the packing fraction during the granular compaction is well described by the empirical law of the form (4).

In Fig. 5 some representative results for the insertion probability $p_j(\theta)$ are shown together with the fitting functions of the form (4). The fitting parameters are obtained by using the nonlinear fitting routine `FMINSEARCH` in `MATLAB`[®] (MathWorks, Natick, MA). This is an implementation of the Nelder-Mead simplex algorithm [44], which minimizes a nonlinear function of several variables. For each shape, a fitting procedure is carried out within a certain range of coverage θ below θ_j , where the probability p_j is lower than $p_j^c = 0.15$. The cutoff probability $p_j^c = 0.15$ is chosen to provide a wide density range within which the fitting procedure is implemented for all wrapping shapes. For most shapes, the cutoff probability $p_j^c = 0.15$ corresponds to the densities that are 30%–40% lower than the corresponding jamming limit θ_j . We have verified that usage of different, but sufficiently small, values of the cutoff parameter p_j^c gives quantitatively similar results for fitting coefficients leading to qualitatively same conclusions.

The data for fitting parameters λ_1 and λ_2 for all wrapping triangles T_j from Table I are plotted in Fig. 6. The parameters

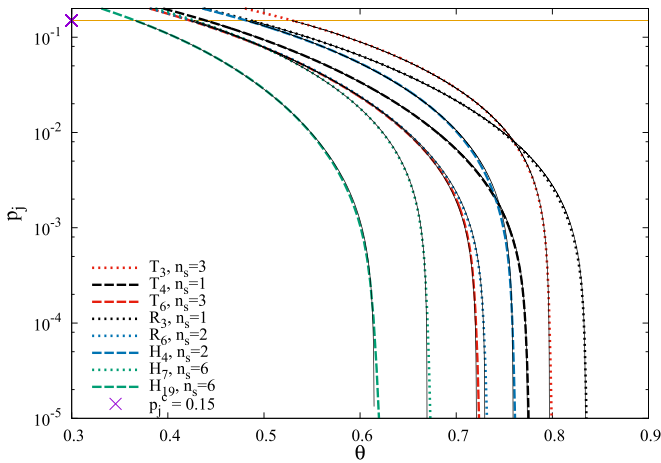


FIG. 5. The decay of the insertion probability $p_j(\theta)$ for the same objects as in Fig. 4 in the range of coverage θ where the corresponding probability p_j is lower than $p_j^c = 0.15$ (thin horizontal line). The continuous superimposed lines are the fits according to Eq. (4). The fitting parameters λ_1 and λ_2 are reported in Fig. 6.

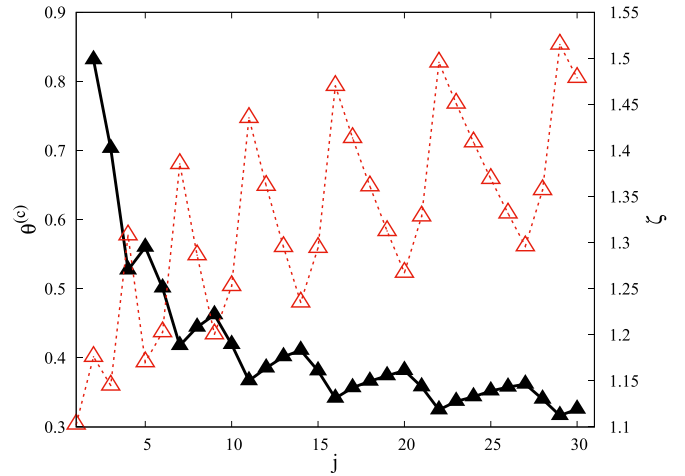


FIG. 7. Characteristic density $\theta^{(c)}$ (Eq. (5)) for all wrapping triangles T_j from Table I (solid symbols, left-hand axis). The opened symbols are plotted against the right-hand axis and give the values of the shape factor $\zeta(j)$ for all wrapping triangles T_j . The characteristic density $\theta^{(c)}(j)$ is anticorrelated with the shape factor $\zeta(j)$.

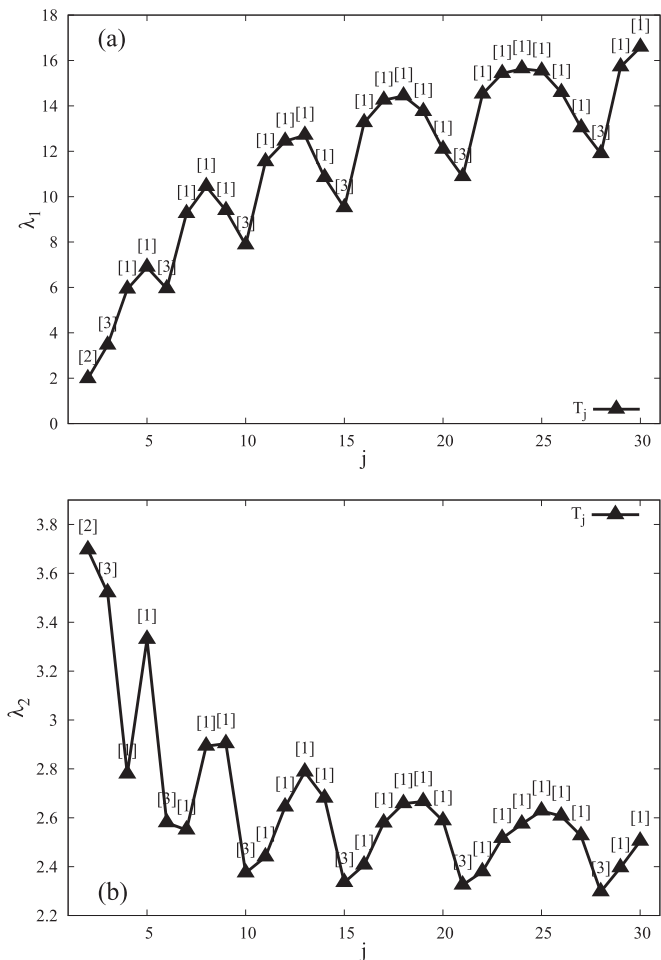


FIG. 6. Parameters (a) λ_1 and (b) λ_2 of the fit (4) for all wrapping triangles from Table I. Numerical values of the symmetry order n_s of the shape j are given in the square brackets above the corresponding plot symbols.

λ_1 and λ_2 depend both on the symmetry order and on the size of the object. The size dependence of the fitting parameters is more pronounced for the parameter λ_1 . However, the most striking feature is that the fitting parameters λ_1 and λ_2 exhibit a local minima for wrapping triangles of the highest symmetry order, $n_s = 3$. It is important to note that the fitting procedure for wrapping rhombuses R_j and hexagons H_j from Tables II and III produce qualitatively similar results for the dependence of the fitting parameters λ_1 and λ_2 both on the symmetry order n_s and on the size j of the object.

We have also considered the behavior of the characteristic density $\theta^{(c)}$ [Eq. (5)] as a function of the object size j . Figure 7 shows the variation of the parameter $\theta^{(c)}$ with j for all wrapping triangles T_j . It is obvious that the symmetry order n_s of the shape is not correlated with the characteristic density $\theta^{(c)}(j)$ for various objects. The behavior of $\theta^{(c)}(j)$ differs from case to case. For example, for shapes $j = 4, 7, 11, 16, 22, 29$ formed by adding a node to the triangle of the highest symmetry order ($n_s = 3$), $\theta^{(c)}(j)$ has a local minima. On the other hand, for shapes $j = 5, 9, 14, 20, 27$ formed by removing a node from the triangle of the highest symmetry order ($n_s = 3$), $\theta^{(c)}(j)$ has a local maxima.

Previous findings suggest that we should consider the connection of deposition kinetics with some of the new geometrical properties of the extended objects. For this purpose we use the concept of the shape factor, which is a dimensionless measure of deviation of the extended objects from circularity. Let us first mention the definition of the shape factor in the case of planar geometric figures. Shape factor ζ (parameter of nonsphericity) combines the circumference C and the surface S of the planar figure [37,45]. It is defined as

$$\zeta = \frac{C^2}{4\pi S}. \tag{6}$$

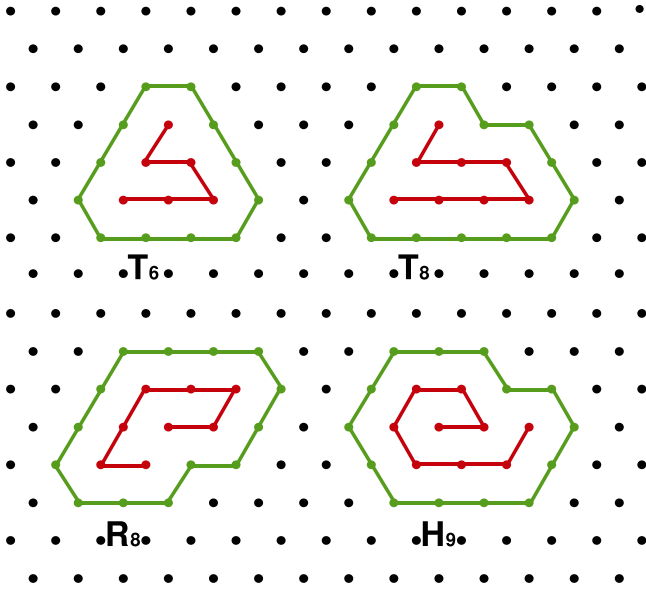


FIG. 8. Construction of the polygon determined by the first neighboring sites on the lattice for the wrapping triangles T_6 and T_8 , rhombus R_8 , and hexagon H_9 . The shape factor of the extended object is equal to the shape factor (6) of the polygon of the first neighboring sites on the lattice.

For a square $\zeta = 4/\pi \approx 1.273$, for a regular pentagon $\zeta = \pi/5 \tan(\pi/5) \approx 1.156$, and for a regular hexagon $\zeta = 6/\sqrt{3\pi^2} \approx 1.103$. Generally, for a regular N -sided polygon we have $\zeta = (N/\pi) \tan(\pi/N)$, which sets a lower bound for other N -sided polygons. Thus a circular structure has a shape factor $\zeta = 1$, while for a convex polygon, the more anisotropic is the polygon, the higher is $\zeta > 1$.

In the case of extended objects on a triangular lattice, the above definition of the shape factor (6) must be generalized. Each lattice shape can be surrounded by the first neighboring sites on the lattice. These nodes unambiguously define a polygon containing the given object. For example, the polygon of the first neighboring sites for a monomer ($j = 1$) is a hexagon; the constructions of such polygon for wrapping triangles T_6 and T_8 , rhombus R_8 , and hexagon H_9 are shown in Fig. 8. Thus, the shape factor of the extended object is equal to the shape factor (6) of the polygon defined by the first neighboring sites on the lattice.

Values of the shape factor $\zeta(j)$ for all wrapping triangles T_j are given in Fig. 7 together with the corresponding characteristic densities $\theta^{(c)}(j)$. We can see that $\theta^{(c)}(j)$ increases with $j > 2$ if $\zeta(j)$ decreases and vice versa. In other words, positions of the local maxima (minima) of $\theta^{(c)}(j)$ coincide with position of the local minima (maxima) of $\zeta(j)$. Qualitatively the same behavior of the shape factor $\zeta(j)$ and the parameter $\theta^{(c)}(j)$ is found in the cases of wrapping rhombuses R_j and hexagons H_j . Indeed, in Figs. 9 and 10 we show that the characteristic density $\theta^{(c)}(j)$ is anticorrelated with the shape factor $\zeta(j)$ for the wrapping rhombuses R_j and hexagons H_j .

Figure 11 illustrates that when the product between the shape factor and the characteristic density, $\zeta(j) \times \theta^{(c)}(j)$, is plotted as a function of the object size j , the data for wrapping triangles T_j , rhombuses R_j , and hexagons H_j collapse onto

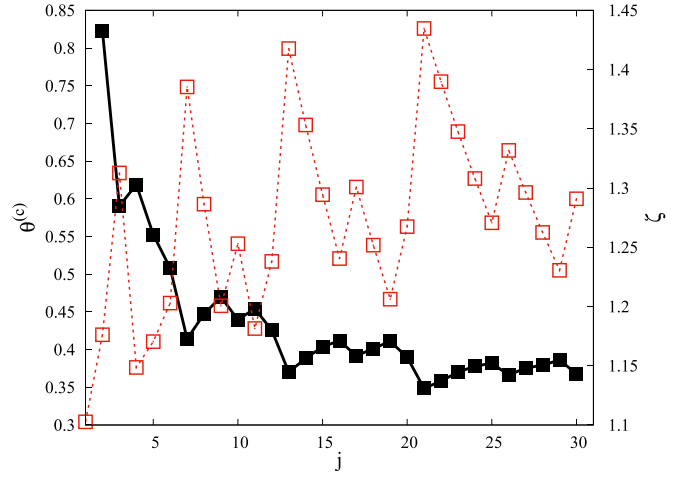


FIG. 9. Characteristic density $\theta^{(c)}$ [Eq. (5)] for all wrapping rhombuses R_j from Table II (solid symbols, left-hand axis). The opened symbols are plotted against the right-hand axis and give the values of the shape factor $\zeta(j)$ for all wrapping rhombuses R_j . The characteristic density $\theta^{(c)}(j)$ is anticorrelated with the shape factor $\zeta(j)$.

a single curve. This figure demonstrates the existence of the single universal master function of the form

$$F(j) = \zeta(j) \times \theta^{(c)}(j) = 1 - C_1 \{1 - \exp[-\frac{1}{2}(j - 2)^{C_2}]\}, \tag{7}$$

where the two fitting parameters are $C_1 = 0.525$ and $C_2 = 0.685$. This result strongly suggests that, for various objects of the same length, the characteristic density $\theta^{(c)}(j)$ of more rounded shapes exceeds the $\theta^{(c)}(j)$ of the elongated ones. Indeed, in Fig. 12 we show the parameter $\theta^{(c)}$ as a function of the shape factor ζ for various triplets of triangles, rhombuses, and hexagons (T_j, R_j, H_j) of the same size,

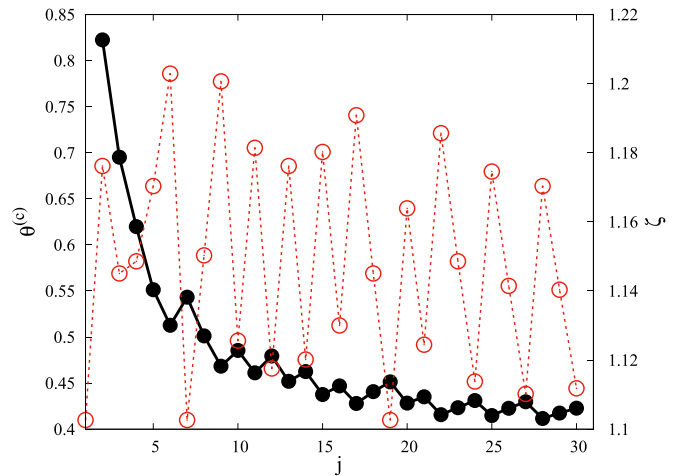


FIG. 10. Characteristic density $\theta^{(c)}$ [Eq. (5)] for all wrapping hexagons H_j from Table III (solid symbols, left-hand axis). The opened symbols are plotted against the right-hand axis and give the values of the shape factor $\zeta(j)$ for all wrapping hexagons H_j . The characteristic density $\theta^{(c)}(j)$ is anticorrelated with the shape factor $\zeta(j)$.

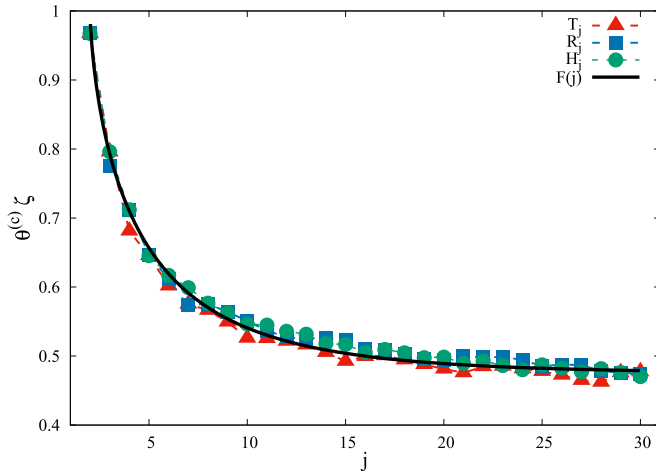


FIG. 11. The product between the shape factor and characteristic density, $\zeta(j) \times \theta^{(c)}(j)$, as a function of the object size j for all wrapping triangles T_j , rhombuses R_j , and hexagons H_j from Tables I–III. The black solid curve is the stretched exponential fit of Eq. (7).

$j = 14, 17, 19, 22, 25, 28, 30$. For each triplet (T_j, R_j, H_j) , our data confirm that the parameter $\theta^{(c)}$ decreases with the shape factor ζ .

Now, it is necessary to establish a connection between the proposed fitting function $p_j(\theta)$ [Eq. (4)] and the exponential approach of the coverage fraction $\theta(t)$ to the jamming limit θ_j [Eq. (1)]. It is easy to show that the following differential equation,

$$\frac{d\theta}{dt} = j p_j(\theta) = j A \left(1 - \frac{\theta}{\theta_j}\right) \exp \left[- \left(\frac{\theta}{\theta^{(c)}} \right)^{\lambda_2} \right], \quad (8)$$

describes the temporal evolution of the coverage $\theta(t)$ in the late stages of deposition process. Let $\theta(t) = jn(t)/L^2$ be the fraction of total lattice sites covered by the deposited objects of

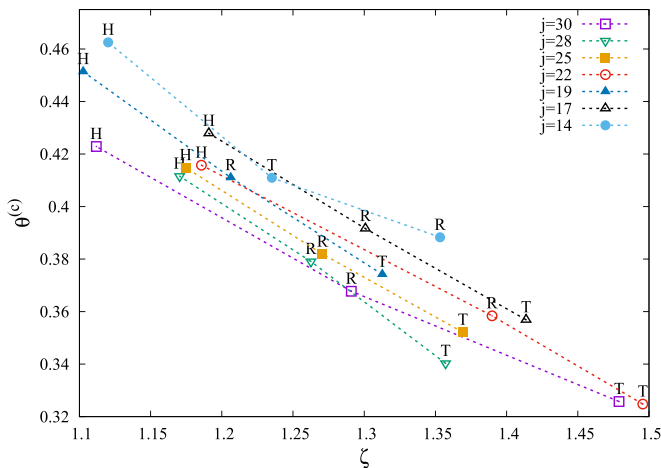


FIG. 12. Characteristic density $\theta^{(c)}$ [Eq. (5)] as a function of the shape factor ζ for various triplets of triangles, rhombuses and hexagons (T_j, R_j, H_j) of the same size, $j = 14, 17, 19, 22, 25, 28, 30$. The letter above the plot symbol indicates the object type. Sizes of the objects for the corresponding triplets are given in the legend.

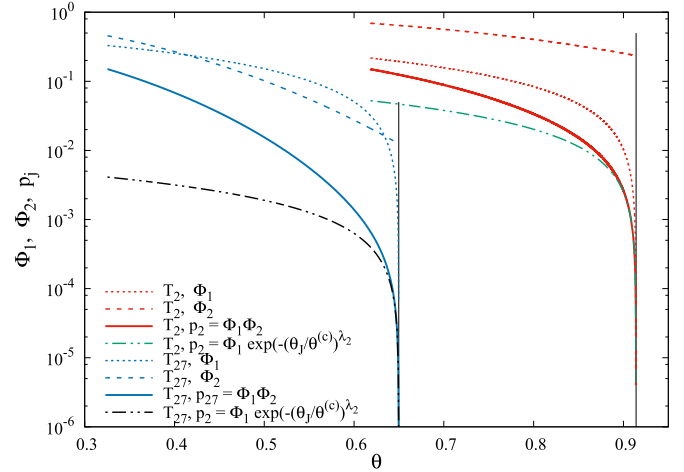


FIG. 13. Functions $\Phi_1(\theta)$ and $\Phi_2(\theta)$ [Eqs. (9) and (10)] obtained by fitting Eq. (4) to the insertion probability data for wrapping triangles T_2 and T_{27} in the case of $p_j^c = 0.15$. The solid lines give the fitting function $p_j(\theta) = \Phi_1(\theta)\Phi_2(\theta)$ [Eq. (4)]. The dot-dashed lines give the approximation $p_j(\theta) = \Phi_1(\theta) \exp[-(\theta_j/\theta^{(c)})^{\lambda_2}]$, as indicated in the legend. Approximation (11) is applicable in the narrower density range in the case of the large object T_{27} than in the case of the dimer T_2 . The parameters of the fit (4) are $\theta^{(c)} = 0.8313$, $\lambda_2 = 3.6964$ for shape T_2 , and $\theta^{(c)} = 0.3619$, $\lambda_2 = 2.5266$ for shape T_{27} . The thin vertical lines indicate the values of jamming coverage for shapes T_2 ($\theta_j = 0.9141$) and T_{27} ($\theta_j = 0.6498$).

size j at time t [$n(t)$ denotes the number of objects adsorbed at time t]. Since the time t is counted by the number of adsorption attempts and scaled by the total number of lattice sites L^2 , the number of deposited objects is increased by $p_j L^2$ per unit time $t \rightarrow t + 1$. Therefore, the coverage at time $t + 1$ is equal to $\theta(t + 1) = j[n(t) + p_j L^2]/L^2$, so that $\theta(t + 1) - \theta(t) = j p_j$ is the increase of the coverage per unit time. Since $\theta(t + 1) - \theta(t) \approx d\theta/dt$, we get $d\theta/dt = j p_j$. Finally, we obtain Eq. (8) assuming that function (4) describes the decay of the insertion probability p_j for all shapes in a wide range of the coverage θ just below θ_j .

Unfortunately, differential equation (8) cannot be solved analytically. However, Eq. (8) can be simplified and solved if we restrict ourselves to the consideration of the very late-time behavior of the deposition process. The right side of differential Eq. (8) is proportional to the product between linear Φ_1 and stretched exponential function Φ_2 , which are given by

$$\Phi_1(\theta) = A \left(1 - \frac{\theta}{\theta_j}\right), \quad (9)$$

$$\Phi_2(\theta) = \exp \left[- \left(\frac{\theta}{\theta^{(c)}} \right)^{\lambda_2} \right]. \quad (10)$$

There is a significant difference in the behavior of these functions near the jamming density for all examined objects. Figure 13 shows the functions $\Phi_1(\theta)$ and $\Phi_2(\theta)$ obtained by fitting Eq. (4) to the insertion probability data in the late stage of the deposition processes for wrapping triangles T_2 and T_{27} . Since the time derivative of coverage $d\theta/dt$ vanishes at $t \rightarrow \infty$ and $\Phi_2 \rightarrow \exp[-(\theta_j/\theta^{(c)})^{\lambda_2}] > 0$, $t \rightarrow \infty$, it is obvious that the function Φ_1 is essential for controlling the kinetics of

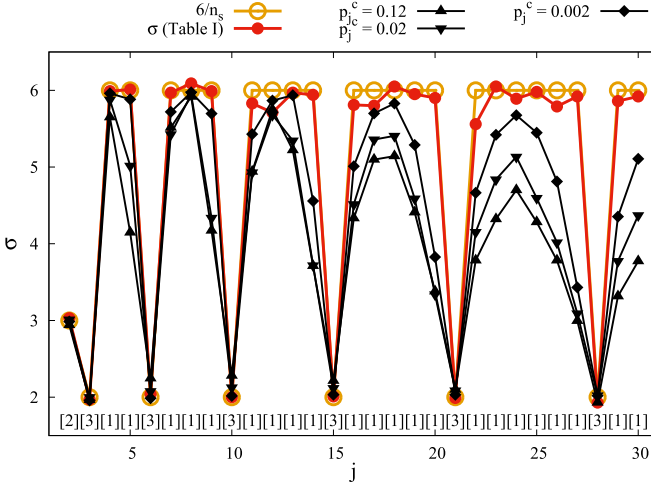


FIG. 14. Relaxation time σ calculated from the expression (13) for all wrapping triangles (Table I). Results are given for three values of threshold $p_j^c = 0.12, 0.02, 0.002$, as indicated in the legend. The full circles correspond to values of σ in Table I. Open circles correspond to values $6/n_s(j)$ [Eq. (14)] for $j = 2, \dots, 30$. Numerical values of the symmetry order $n_s(j)$ of the shape are given in the square brackets above the x axis.

adsorption process near the jamming limit θ_j . Our further analysis deals with the rapidity of the approach to the jammed state, so that we can introduce the following approximation:

$$\Phi_2(\theta) = \exp\left[-\left(\frac{\theta}{\theta^{(c)}}\right)^{\lambda_2}\right] \approx \exp\left[-\left(\frac{\theta_j}{\theta^{(c)}}\right)^{\lambda_2}\right],$$

for $\theta \lesssim \theta_j$. (11)

This approximation allows us to solve Eq. (8). Accordingly, the coverage fraction of the system θ grows exponentially in time towards the jamming state value θ_j :

$$\theta(t) = \theta_j \left[1 - \exp\left(-\frac{t}{\sigma}\right)\right], \quad \text{for } \theta \lesssim \theta_j, \quad (12)$$

where

$$\sigma = \frac{\theta_j \exp(\lambda_1 \theta_j^{\lambda_2})}{jA} = \frac{\theta_j \exp\left[\left(\frac{\theta_j}{\theta^{(c)}}\right)^{\lambda_2}\right]}{jA}. \quad (13)$$

Consequently, the function (4) that we have proposed to characterize the insertion probability p_j is compatible with the exponential approach (1) to the jamming limit θ_j .

Equation (13) is a functional relationship between the relaxation time σ and the parameters A, λ_1 , and λ_2 in the fitting function (4). Our previous findings concerning the kinetics of the deposition process clearly confirm that the relaxation time σ in Eq. (1) is inversely proportional to the order of symmetry axis n_s of the shape:

$$\sigma = \frac{6}{n_s}. \quad (14)$$

It is interesting to verify whether the Eq. (13) gives the values of the parameter σ that are in accordance with the symmetry order n_s of the shape [Eq. (14)]. Figure 14 shows the values of the relaxation time σ obtained from the expression (13) for all wrapping triangles (Table I). For each object, the values of the

parameters A, λ_1 , and λ_2 in Eq. (13) were calculated by fitting the function (4) to the insertion probability data for three values of the cutoff probability $p_j^c = 0.12, 0.02, 0.002$. It is obvious that Eqs. (13) and (14) give approximately equal relaxation times σ in the case of more symmetric shapes ($n_s = 2, 3; j = 2, 3, 6, 10, 15, 21, 28$). However, the values of parameter σ obtained by Eq. (13) in the case of asymmetric shapes ($n_s = 1$) are not well fitted by integer $6/n_s = 6$ [Eq. (14)]. These deviations are particularly high for the large objects. The reasons for these differences can be seen in Fig. 13. Comparing the insertion probabilities near the jamming state for the objects T_2 and T_{27} , one can see that approximation (11) is applicable in the narrower density range in the case of the large object T_{27} than in the case of the dimer T_2 . Accordingly, the lowering of the cutoff value p_j^c reduces the deviation of the relaxation time σ , calculated from Eq. (13), from the integer value of 6 (see Fig. 14). The presented results provide a further justification for the choice of function (4) to describe the decay of the insertion probability p_j for all extended shapes on the triangular lattice.

IV. SUMMARY

RSA kinetics of particles of various shapes on flat two-dimensional homogeneous surfaces depends generally on the shape anisotropy and on the number of degrees of freedom. However, in the case of irreversible deposition on planar lattices, the kinetics of the late stage of deposition is determined exclusively with the symmetry properties of the shapes. To demonstrate this, we have performed extensive numerical simulations of the RSA using the shapes of different number of segments and rotational symmetries on a triangular lattice. The shapes are made by self-avoiding lattice steps, whereby the size of the objects is gradually increased by wrapping the walks in several different ways.

As expected, the approach to the jamming limit was found to be exponential for all the shapes. It was shown that the coverage kinetics is severely slowed with the decrease of the order of symmetry of the shape. We have also pointed out that the relaxation time σ [Eq. (1)] is inversely proportional to the order of symmetry axis n_s of the shape, $\sigma = 6/n_s$. We found that for small objects, jamming coverages θ_j decrease very rapidly with the size of the objects, regardless of their shape. But for sufficiently large objects it turned out that changing the shape has considerably more influence on the jamming density than increasing the object size.

Special attention is paid to the behavior of probability p_j for the insertion of a new particle onto a lattice during the deposition process. The insertion probability p_j is found to decay with the coverage θ according to Eq. (4). It is shown that the characteristic density $\theta^{(c)}(j)$ [see Eq. (4)] is anticorrelated with the shape factor $\zeta(j)$ of the objects. In addition, our data confirm that, for objects of the same length, parameter $\theta^{(c)}$ decreases with the shape factor ζ . Consequently, this work provides the link between the behavior of the insertion probability p_j and the intrinsic properties of the shapes.

We have established a connection between the proposed fitting function [Eq. (4)] for the decay of the insertion probability and the exponential approach of the coverage fraction $\theta(t)$ to the jamming limit θ_j [Eq. (1)]. It was shown

that the obtained functional relationship (13) between the relaxation time σ and the fitting parameters in expression (4) gives the values of the parameter σ that are in accordance with the symmetry order n_s of the shape [Eq. (14)].

It must be stressed that the presence of desorption and diffusional relaxation of particles changes some of the important properties of the RSA. When desorption is introduced in RSA processes, slowing of the deposition dynamics occurs with increasing of symmetry order of the shapes [29]. Furthermore, the presence of diffusion only hastens the approach to the final disordered state [32]. As expected, the behavior of the insertion probability during the reversible deposition of extended objects look very different in comparison with the irreversible case. When desorption of the objects is present, insertion probability first follows the corresponding RSA

curve until it reaches a value close to the equilibrium one at which point it plateaus and evolves very weakly towards the equilibrium [46]. Consequently, function (4) is not suitable to describe the decreasing of the insertion probability toward its equilibrium value during the reversible RSA.

ACKNOWLEDGMENTS

This work was supported by the Ministry of Education, Science, and Technological Development of the Republic of Serbia under Projects ON171017 and III45016, and by the European Commission under H2020 project VI-SEEM, Grant No. 675121. Numerical simulations were run on the PARADOX supercomputing facility at the Scientific Computing Laboratory of the Institute of Physics Belgrade.

-
- [1] J. W. Evans, Random and cooperative sequential adsorption, *Rev. Mod. Phys.* **65**, 1281 (1993).
- [2] V. Privman (ed.), *Nonequilibrium Statistical Mechanics in One Dimension* (Cambridge University Press, Cambridge, UK, 1997), (a collection of review articles).
- [3] V. Privman, guest editor, *Colloids Surf. A* **165**, 1 (2000), (a collection of review articles).
- [4] A. Cadilhe, N. A. M. Araújo, and V. Privman, Random sequential adsorption: From continuum to lattice and pre-patterned substrates, *J. Phys.: Condens. Matter* **19**, 065124 (2007).
- [5] J. Feder, Random sequential adsorption, *J. Theoret. Biol.* **87**, 237 (1980).
- [6] R. H. Swendsen, Dynamics of random sequential adsorption, *Phys. Rev. A* **24**, 504 (1981).
- [7] Y. Pomeau, Some asymptotic estimates in the random parking problem, *J. Phys. A: Math. Gen.* **13**, L193 (1980).
- [8] B. Bonnier, Random sequential adsorption of binary mixtures on a line, *Phys. Rev. E* **64**, 066111 (2001).
- [9] M. C. Bartelt and V. Privman, Kinetics of irreversible multilayer adsorption: One-dimensional models, *J. Chem. Phys.* **93**, 6820 (1990).
- [10] S. S. Manna and N. M. Švrakić, Random sequential adsorption: Line segments on the square lattice, *J. Phys. A: Math. Gen.* **24**, L671 (1991).
- [11] Lj. Budinski-Petković and U. Kozmidis-Luburić, Random sequential adsorption on a triangular lattice, *Phys. Rev. E* **56**, 6904 (1997).
- [12] Lj. Budinski-Petković, S. B. Vrhovac, and I. Lončarević, Random sequential adsorption of polydisperse mixtures on discrete substrates, *Phys. Rev. E* **78**, 061603 (2008).
- [13] P. Viot, G. Tarjus, S. M. Ricci, and J. Talbot, Random sequential adsorption of anisotropic particles. I. Jamming limit and asymptotic behavior, *J. Chem. Phys.* **97**, 5212 (1992).
- [14] J. D. Sherwood, Random sequential adsorption of lines and ellipses, *J. Phys. A* **23**, 2827 (1990).
- [15] R. D. Vigil and R. M. Ziff, Random sequential adsorption of unoriented rectangles onto a plane, *J. Chem. Phys.* **91**, 2599 (1989).
- [16] R. D. Vigil and R. M. Ziff, Kinetics of random sequential adsorption of rectangles and line segments, *J. Chem. Phys.* **93**, 8270 (1990).
- [17] M. Cieřla and J. Barbasz, Random packing of regular polygons and star polygons on a flat two-dimensional surface, *Phys. Rev. E* **90**, 022402 (2014).
- [18] M. Cieřla and P. Karbowiczek, Random sequential adsorption of starlike particles, *Phys. Rev. E* **91**, 042404 (2015).
- [19] M. Cieřla, Continuum random sequential adsorption of polymer on a flat and homogeneous surface, *Phys. Rev. E* **87**, 052401 (2013).
- [20] P. B. Shelke and A. V. Limaye, Dynamics of random sequential adsorption (RSA) of linear chains consisting of n circular discs: role of aspect ratio and departure from convexity, *Surf. Sci.* **637–638**, 1 (2015).
- [21] M. Cieřla, Properties of random sequential adsorption of generalized dimers, *Phys. Rev. E* **89**, 042404 (2014).
- [22] M. Cieřla, G. Pajk, and R. M. Ziff, Shapes for maximal coverage for two-dimensional random sequential adsorption, *Phys. Chem. Chem. Phys.* **17**, 24376 (2015).
- [23] M. Cieřla, G. Pajk, and R. M. Ziff, In a search for a shape maximizing packing fraction for two-dimensional random sequential adsorption, *J. Chem. Phys.* **145**, 044708 (2016).
- [24] M. D. Khandkar, A. V. Limaye, and S. B. Ogale, Shape Effects in Random Sequential Adsorption of Zero-Area Angled Objects on a Continuum Substrate, *Phys. Rev. Lett.* **84**, 570 (2000).
- [25] G. C. Barker and M. J. Grimson, Random sequential adsorption of lattice shapes onto a square lattice, *Mol. Phys.* **63**, 145 (1988).
- [26] Lj. Budinski-Petković and U. Kozmidis-Luburić, Jamming configurations for irreversible deposition on a square lattice, *Physica A* **236**, 211 (1997).
- [27] R. S. Ghaskadvi and M. Dennin, Reversible random sequential adsorption of dimers on a triangular lattice, *Phys. Rev. E* **61**, 1232 (2000).
- [28] Lj. Budinski-Petković and U. Kozmidis-Luburić, Adsorption-desorption processes of extended objects on a square lattice, *Physica A* **301**, 174 (2001).
- [29] Lj. Budinski-Petković, M. Petković, Z. M. Jakšić, and S. B. Vrhovac, Symmetry effects in reversible random sequential adsorption on triangular lattice, *Phys. Rev. E* **72**, 046118 (2005).
- [30] V. Privman, Dynamics of nonequilibrium deposition, *Colloids Surf. A* **165**, 231 (2000).

- [31] C. Fusco, P. Gallo, A. Petri, and M. Rovere, Random sequential adsorption and diffusion of dimers and k -mers on a square lattice, *J. Chem. Phys.* **114**, 7563 (2001).
- [32] I. Lončarević, Z. M. Jakšić, S. B. Vrhovac, and Lj. Budinski-Petković, Irreversible deposition of extended objects with diffusional relaxation on discrete substrates, *Eur. Phys. J. B* **73**, 439 (2010).
- [33] G. Kondrat, Impact of composition of extended objects on percolation on a lattice, *Phys. Rev. E* **78**, 011101 (2008).
- [34] Lj. Budinski-Petković, I. Lončarević, M. Petković, Z. M. Jakšić, and S. B. Vrhovac, Percolation in random sequential adsorption of extended objects on a triangular lattice, *Phys. Rev. E* **85**, 061117 (2012).
- [35] N. I. Lebovka, Y. Yu. Tarasevich, D. O. Dubinin, V. V. Laptev, and N. V. Vygornitskii, Jamming and percolation in generalized models of random sequential adsorption of linear k -mers on a square lattice, *Phys. Rev. E* **92**, 062116 (2015).
- [36] J.-S. Wang and R. B. Pandey, Kinetics and Jamming Coverage in a Random Sequential Adsorption of Polymer Chains, *Phys. Rev. Lett.* **77**, 1773 (1996).
- [37] F. Moučka and I. Nezbeda, Detection and Characterization of Structural Changes in the Hard-Disk Fluid Under Freezing and Melting Conditions, *Phys. Rev. Lett.* **94**, 040601 (2005).
- [38] E. L. Hinrichsen, J. Feder, and T. Jssang, Geometry of random sequential adsorption, *J. Stat. Phys.* **44**, 793 (1986).
- [39] J. W. Evans, D. R. Burgess, and D. K. Hoffman, Irreversible random and cooperative processes on lattices: Spatial correlations, *J. Math. Phys.* **25**, 3051 (1984).
- [40] B. Bonnier, M. Hontebeyrie, Y. Leroyer, C. Meyers, and E. Pommiers, Adsorption of line segments on a square lattice, *Phys. Rev. E* **49**, 305 (1994).
- [41] N. I. Lebovka, N. N. Karmazina, Y. Yu. Tarasevich, and V. V. Laptev, Random sequential adsorption of partially oriented linear k -mers on a square lattice, *Phys. Rev. E* **84**, 061603 (2011).
- [42] R. Hilfer, Analytical representations for relaxation functions of glasses, *J. Non-Cryst. Solids* **305**, 122 (2002).
- [43] F. Ludewig, N. Vandewalle, and S. Dorbolo, Compaction of granular mixtures, *Granular Matter* **8**, 87 (2006).
- [44] J. C. Lagarias, J. A. Reeds, M. H. Wright, and P. E. Wright, Convergence properties of the Nelder-Mead simplex method in low dimensions, *SIAM J. Opt.* **9**, 112 (1998).
- [45] P. Richard, J. P. Troadee, L. Oger, and A. Gervois, Effect of the anisotropy of the cells on the topological properties of two- and three-dimensional froths, *Phys. Rev. E* **63**, 062401 (2001).
- [46] J. Talbot, G. Tarjus, and P. Viot, Adsorption-desorption model and its application to vibrated granular materials, *Phys. Rev. E* **61**, 5429 (2000).



Group chase and escape in the presence of obstacles

J.R. Šćepanović^a, A. Karač^b, Z.M. Jakšić^a, Lj. Budinski-Petković^c, S.B. Vrhovac^{a,*}

^a Scientific Computing Laboratory, Center for the Study of Complex Systems, Institute of Physics Belgrade, University of Belgrade, Pregrevica 118, Zemun 11080, Belgrade, Serbia

^b Polytechnic faculty, University of Zenica, Bosnia and Herzegovina

^c Faculty of Engineering, Trg D. Obradovića 6, Novi Sad 21000, Serbia

HIGHLIGHTS

- Hunting in the presence of obstacles is studied.
- Dynamics of smart chasing and escape between two species is studied by MC simulations.
- Stretched exponential behavior excellently describes the capture dynamics.
- Characteristic time τ decreases with the initial density of targets as a power law.
- Characteristic timescale τ increases with the density of obstacles.

ARTICLE INFO

Article history:

Received 13 November 2018

Received in revised form 20 February 2019

Available online 14 March 2019

Keywords:

Group chase and escape

Square lattice

Obstacles

Stretched-exponential function

ABSTRACT

We study a stochastic lattice model describing the dynamics of a group chasing and escaping between two species in an environment that contains obstacles. The Monte Carlo simulations are carried out on a two-dimensional square lattice. Obstacles are represented by non-overlapping lattice shapes that are randomly placed on the lattice. The model includes smart pursuit (chasers to targets) and evasion (targets from chasers). Both species can affect their movement by visual perception within their finite sighting range σ .

We concentrate here on the role that density and shape of the obstacles plays in the time evolution of the number of targets, $N_T(t)$. Temporal evolution of the number of targets $N_T(t)$ is found to be stretched-exponential, of the form $N_T(t) = N_T(0) - \delta N_T(\infty) (1 - \exp[-(t/\tau)^\beta])$, regardless of whether the obstacles are present or not. The characteristic timescale τ is found to decrease with the initial density of targets ρ_0^T according to a power-law, i.e., $\tau \propto (\rho_0^T)^{-\gamma}$. Furthermore, temporal dependences of the number of targets $N_T(t)$ are compared for various combinations of chasers and targets with different sighting ranges, $\sigma = 1, 2$, in order to analyze the relationship between the ability of species and the capture dynamics in the presence of obstacles.

© 2019 Elsevier B.V. All rights reserved.

1. Introduction

The collective motion of interacting organisms such as bacteria colonies [1–3], amoeba [4–6], cells [7–9], insects [10,11], fish [12,13], birds [14,15], and humans [16–20] has drawn great attention of researchers from diverse fields in

* Corresponding author.

E-mail address: vrhovac@ipb.ac.rs (S.B. Vrhovac).

URL: <http://www.ipb.ac.rs/~vrhovac/> (S.B. Vrhovac).

the past two decades [21]. Pursuit and evasion problems have a long and interesting history [22]. It is well known that collective motion of individuals with escape and pursuit behavior serve as a protection mechanisms against chasers. The goal for chaser (predator) and target (for example, prey) is to choose an efficient motion strategy that optimizes their respective chances of successful pursuit or evasion. At first, developing computational systems and techniques enabled one to deal with a two-particle system consisting of one chaser and one target, where there existed a challenging mathematical problem for obtaining analytical expressions [22]. Also, a class of pursuit-and-evasion problems involving a single evading prey that is being hunted by $N > 1$ predators has been modeled and analyzed [23–25]. In addition to these modeling efforts, extensive research has been devoted to developing multi-agent models that consider the role of multiple predators and/or preys [26–35].

Kamimura and Ohira [26] have introduced a lattice model to analyze the group spatial chase and escape phenomena. The model assumes that chasers and targets are initially placed randomly on the square lattice as pointlike particles. Both species perform independent nearest-neighbor random walks on a lattice following simple dynamical rules, increasing or decreasing the distance from the nearest particle of the opposite group. Chasers start a direct chase whenever a target appears within their sighting range. Targets try to evade capture by making a distance of one lattice spacing in a direction away from the nearest chaser. Target is caught upon the first encounter with a chaser. In their model, although each chaser independently moves in order to catch one of the nearest targets, some groups of chasers are simultaneously formed. In the simulation, the chasers form flocks and seem to cooperate to catch the flocks of targets [24,26,33,34,36]. In the basic version of the model, chasers can sense the positions of the targets at an arbitrary distance. The authors have considered several extensions to this simplest version of the model, including the search range of chasers and targets, and introduction of a term designed to account for random fluctuations that are usually present in real systems. Despite its simplicity, the model is able to reproduce a lot of interesting behaviors [27].

Based on a concept proposed by Kamimura and Ohira [26] we built up a bio-inspired realistic agent-based approach to model collective chasing and escaping in a discrete space and time with periodic boundary conditions for the case when the lattice is initially covered with obstacles at various concentrations. The depositing objects (obstacles) are formed by a small number of lattice steps on the square lattice. Spatial distribution of the obstacles on the lattice is created using the random sequential adsorption (RSA) method [37,38]. The dominant effect in RSA is the blocking of the available surface area. When the surface is saturated by the adsorbed objects so that no further objects can be placed, the system reaches the jamming limit ρ_j . Thus, an element of stochasticity of environment, which is present in any natural system, is incorporated into the model. It must be emphasized that birth and death processes [39,40] are not considered here, so the results obtained apply only on the time scales short compared to the typical lifetime of single organisms. The role of multiple predators and preys has also been studied by using an off-lattice models [41,42], based on the modeling of the self-propelled organisms by Vicsek et al. and including the chase-escape mechanisms through simple intergroup pairwise interactions [43]. In such models, an analysis of the impact of geometrically complex boundary conditions, such as obstacles, would require taking into account a hard core repulsion term in the interaction. However, the lattice-based models allow easier handling of objects (obstacles) of various shapes and sizes.

For the real life systems, simulation resembles to two animal species fighting for the survival. Obstacles may be trees, rocks, or anything that is big enough for the evader and pursuer to become “invisible” for the other. The chasers and evaders can also be human beings, but with different roles, like police officers and robbers, where buildings, grocery stores and similar objects can be viewed as obstacles.

We study the survival of N_0^T targets (for example, prey) that is captured by N_0^C chasers (predators) in the presence of static obstacles. We have kept the rules governing the dynamics of the processes at the individual level as simple as possible to focus entirely on the effects of obstacles. Each species has its specific sighting range σ in which it can see the other species. In [26], for each target, the distance to each chaser is calculated as the Euclidean distance. Unlike the Kamimura and Ohira model [26], distances as well as sighting ranges in the present study are measured by a L^1 (“Manhattan”) metric. Manhattan distance between sites P_1 and P_2 on a square lattice is equal to the length of all paths connecting P_1 and P_2 along horizontal and vertical segments, without ever going back. Therefore, Manhattan metric more correctly than Euclidean’s determines the length of the path between two sites in the lattice-based models. In our model, there are two types of chasers and targets and each of them has its own sighting range σ , which describes their skills at chasing and escaping, respectively. In reality, chasers search for targets in their vicinities. Similarly, targets can recognize the existence of nearby chasers. Therefore, analysis of the capture dynamics in the present study is limited to species with two different sighting ranges, i.e., $\sigma = 1, 2$. If the value of σ equals zero, the movement is equivalent to the random walkers [26,28,40,44]. It has been confirmed that the idea of animals using blind search strategies does not seem to be usable since it neglects the role of animals’ smartness and experience in guiding them [45]. We investigate the role that the density of obstacles plays in the time evolution of the number of targets, $N_T(t)$. A detailed analysis of the contribution to the capture dynamics coming from the size and the shape of obstacles is carried out. Furthermore, temporal dependences of the number of targets $N_T(t)$ in the presence of obstacles are compared for various combinations of chasers and targets with different chasing and avoidance skills in order to analyze the relationship between the ability of species and the capture dynamics. In particular, we try to find a universal functional type that describes the decrease in the number of targets $N_T(t)$ in the best way.

We organized the paper as follows. Section 2 describes the details of the model and simulations. In Section 3 results of numerical simulation are presented and discussed. Finally, Section 4 contains some additional comments and final remarks.

2. Definition of the model and the simulation method

The environment where two interacting species coexist is represented by the two-dimensional square lattice of linear size L with periodic boundary conditions. In our model the lattice is initially occupied by obstacles of various shapes and sizes at the effective density ρ_0 . This density is defined as a fraction of sites of the lattice that are occupied by the obstacles. Linear obstacles are k -mers of length $\ell = k - 1 = 0, 1, \dots, 6$, shown in Table 1 as objects (A_1) – (A_7) . Extended shapes that we have used as obstacles are the crosses of two different sizes, shown in Table 2 as objects (C_1) and (C_2) .

Obstacles cannot overlap and their spatial distribution at density ρ_0 is generated using the random sequential adsorption (RSA) method [37,38]. In the case of mixtures of obstacles, at each deposition attempt, one of the objects that makes the mixture is selected at random and deposition of the selected object is tried in a randomly chosen lattice site. In this way we are able to prepare the environment in disordered initial state with a statistically reproducible density ρ_0 of obstacles. To initialize the model, N_0^C chasers and N_0^T targets are randomly distributed as monomers in the lattice. Each site can be either empty or occupied by one particle: by a chaser or escapee (target) or by a particle that belongs to an obstacle.

After placing the chasers and the targets up to the chosen densities $\rho_0^C = N_0^C/L^2$ and $\rho_0^T = N_0^T/L^2$, we switch the species deposition events off and initiate a random diffusive dynamics in the system. At this stage, apart from the hard core interaction between the species, and between the species and the obstacles, there are simple rules governing the dynamic processes at the individual level. Movement within the lattice and the population dynamics are modeled as discrete time processes. At each Monte Carlo step a lattice site is selected at random. If the selected site is unoccupied or occupied by an obstacle, the configuration remains unchanged and a new site is selected at random. If the selected site is occupied by a chaser or an escapee, each species follow the hopping rules described below.

Chaser has a certain pursuit region within which it can locate targets; simultaneously, target has an escape zone inside which it can detect chasers. In other words, each species has its specific sighting range σ in which it can see the other species. By definition, the metric is L^1 , so e.g. the site (x, y) is at distance $|x| + |y|$ from the origin, with lattice spacing equal to unity. Two types of chasers and targets are used in our model depending on the sighting range σ : Chasers-I and Targets-I have sighting range $\sigma = 1$, while for Chasers-II and Targets-II, $\sigma = 2$.

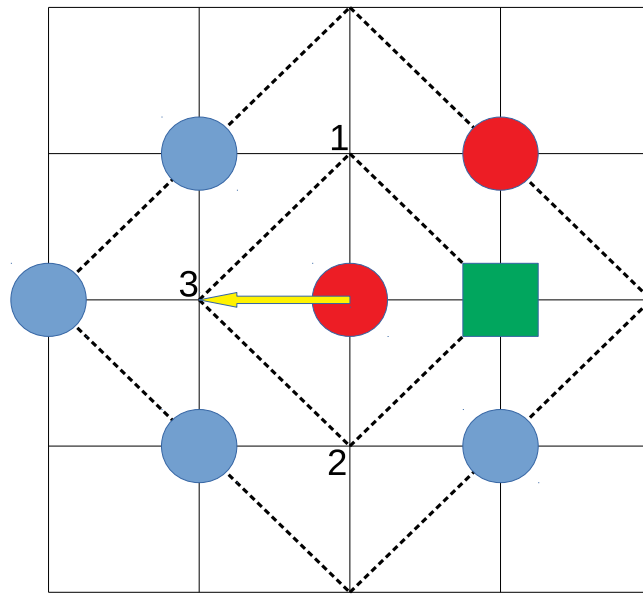
Suppose that Chaser-I is placed in a randomly selected site of the lattice. If the first neighbors of the selected site are entirely occupied with obstacles and chasers, the chosen chaser stays at its original position. Then, the time t is updated, $t \rightarrow t + 1/L^2$ and the process continues by choosing a new lattice site at random. Suppose that some of the first neighbors of the selected site are occupied with targets. Then we randomly select a target among them, remove the selected target from the grid, and move the chosen chaser to this empty place. However, if the first neighbors of the chosen chaser are not occupied with targets, the chaser executes a jump as long as there is at least one empty nearest neighbor site. In this case, the chaser is moved to the randomly selected empty adjacent site.

Now, suppose that Target-I is placed in a randomly selected site of the lattice. If there are no empty nearest neighbors of the selected site, the chosen target does not change its position, and the time increases by $1/L^2$. If the selected site has empty adjacent sites, the chosen target moves into one of them randomly.

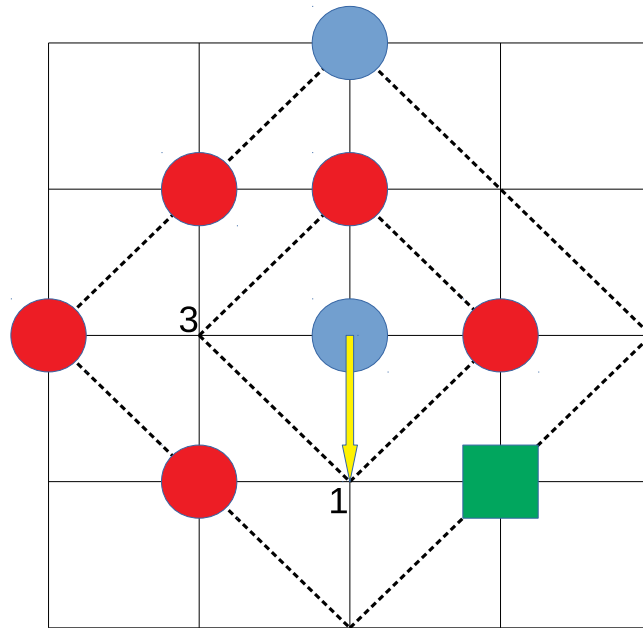
In our model we introduce chasers and targets with different chasing and avoidance skills, respectively, depending on the sighting range σ . Accordingly, decision for every step both of the Chaser-II and Target-II depends on the species that are found at the places of second neighbors. Algorithms for movement of species I and II are different only in the method of selection of the empty neighboring sites for a jump. Species I randomly chooses an empty nearest neighbor site for a jump. However, Chaser-II moves to the empty adjacent site that is surrounded by the highest number of targets, $n_T^{(\max)}$, as its first neighbors (see, Fig. 1(a)). On the contrary, Target-II jumps to the empty nearest neighbor site that is surrounded by the lowest number of chasers, $n_C^{(\min)}$, as its first neighbors (see, Fig. 1(b)). If two or more empty nearest neighbor sites correspond to the same highest/lowest number of targets $n_T^{(\max)}$ /chasers $n_C^{(\min)}$, one of them is selected at random. It must be emphasized that Target-II moves to the selected site only if $n_C^{(\min)}$ is less than or equal to the number of chasers surrounding it in its original position. In both cases when the sighting range σ is one or two, pursuer and evader can move only to a neighboring site. Neither chasers nor evaders can see through the obstacles and they make their decision about the movement without the knowledge of the situation behind the obstacle.

The time t is counted by the number of attempts to select a lattice site and scaled by the total number of lattice sites $N = L^2$. Since in one Monte Carlo time step each lattice site is randomly checked once on the average, it can be considered that all chasers and targets are active at all times and that none of the species have a priority in the number of attempts to make a move. The simulation data are averaged over 100 independent runs for each coverage of obstacles and each initial chasers and targets concentrations.

The simulations have been performed for a wide range of obstacle densities, $\rho_0 < 0.45$, below the corresponding percolation thresholds [46,47]. Considering the underlying percolation problem on the lattice, a geometric transition occurs at the percolation threshold p_c^* , above which the void space falls completely apart into finite clusters. As density of obstacles is increased above a certain critical value p_c^* , the initial large cluster of empty lattice space breaks into tiny non-communicating components and connectivity between both sides of the lattice disappears. In this case, spatially separated groups of chasers and targets can be formed on the lattice during the initialization process. Such artificial situations will not be considered in this paper.



(a)



(b)

Fig. 1. Hopping rules for (a) chasers and (b) targets. Diamonds represent their respective sighting ranges, $\sigma = 1, 2$. The green squares show the obstacles. Chasers (red circles) look for the nearest target and move to one of the nearest sites in order to catch the target. Targets (blue circles) try to escape from the nearest chaser. When a target is in a site nearest to a chaser, the chaser catches the target by hopping to the site, and then the target is removed from the system. Panel (a): Yellow arrow from the chaser to the adjacent site indicates that the Chaser-II hops to the empty site that is surrounded by the highest number of targets ($n_t^{(\max)} = 3$). Chaser-I has three choices. Panel (b): Yellow arrow from the target to the adjacent site indicates that Target-II hops to the empty site that is surrounded by the lowest number of chasers ($n_c^{(\min)} = 1$). Target-I has two choices. Values of the number of the nearest targets and chasers are given for the empty adjacent sites.

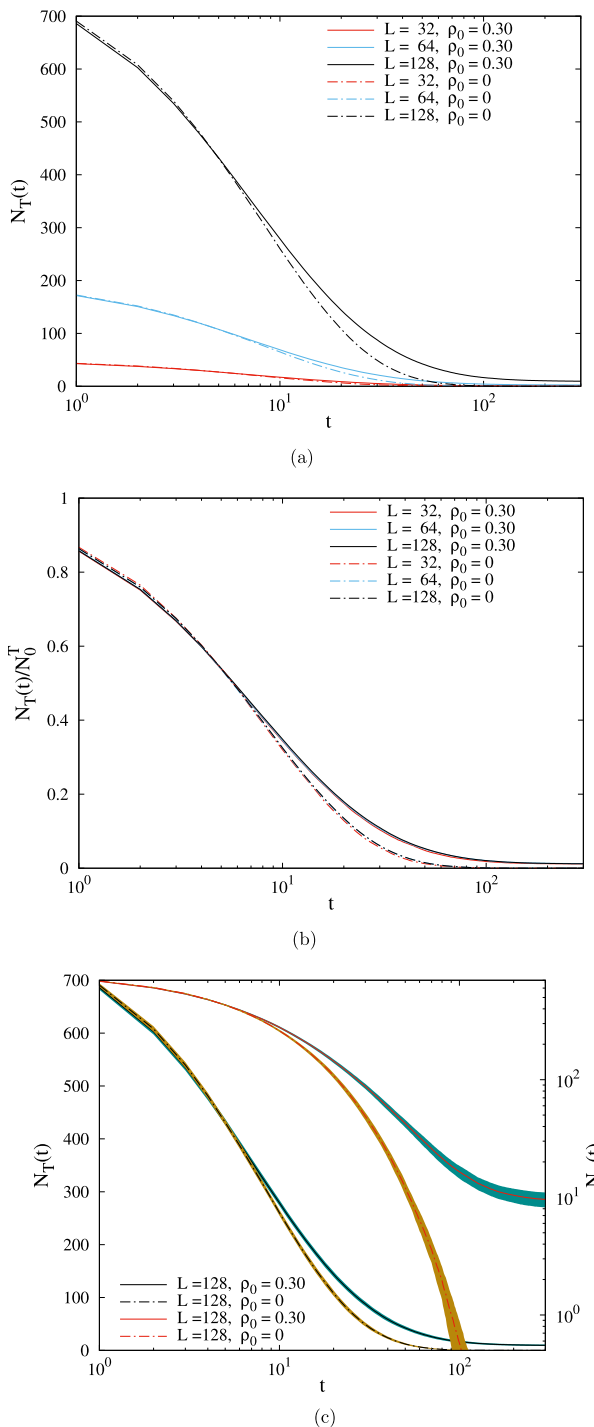


Fig. 2. Time dependences of the number of targets $N_T(t)$ (panel (a)) and of the normalized number of targets $N_T(t)/N_0^T$ (panel (b)) on the lattices of size $L = 32, 64$, and 128 , as indicated in legend. The full curves represent the results obtained when obstacles are the binary mixtures of trimers (A_3) and crosses (C_1) of density $\rho_0 = 0.30$ (see, Tables 1 and 2). The dashed curves represent the results obtained in the absence of obstacles. Panel (c): Shown here are the temporal dependences of the number of targets $N_T(t)$ on the lattice of size $L = 128$, obtained for the same conditions as in panel (a) (see legend). The black (red) lines are plotted against the left-hand (right-hand) axis. The shaded region represents the standard deviation. Results shown in panels (a), (b), and (c) are obtained for the same initial densities $\rho_0^C = 0.0439$ and $\rho_0^T = 0.0488$, for all lattices. Initial values for the number of chasers/targets are $N_0^C/N_0^T = 45/50, 180/200, 720/800$ for $L = 32, 64, 128$, respectively.

3. Results and discussion

While the number of chasers, $N_C(t)$, remains constant N_0^C , the number of targets, $N_T(t)$, monotonically decreases along with the catches. Here we focus on the model that includes species with sighting range $\sigma = 2$ (Chasers-II + Target-II), and study the effects of obstacles on the time evolution of the number of targets, $N_T(t)$. In addition, we will compare the results for all four combinations of previously defined species I and II, as shown in Table 3.

In our model, lattice size L is an arbitrary parameter. In Fig. 2(a) we show the temporal dependence of the number of targets $N_T(t)$ on the lattices of size $L = 32, 64,$ and 128 , when obstacles are the binary mixtures of trimers (A_3) and crosses (C_1) of density $\rho_0 = 0.30$ (see, Tables 1 and 2). For comparison, we also plot the temporal dependences of the number of targets $N_T(t)$ in the absence of obstacles for these three lattices. It is important to note that the initial densities of chasers ρ_0^C and targets ρ_0^T have not changed with the lattice size L . Numerical results for $N_T(t)$ in Fig. 2(a) are given for the initial densities $\rho_0^C = 0.0439$ and $\rho_0^T = 0.0488$, with the same ratio $\rho_0^C/\rho_0^T = N_0^C/N_0^T = 0.9$ for all the lattices. In Fig. 2(b), the values of the normalized number of targets $N_T(t)/N_0^T$ versus the time t are presented for the simulation results shown in Fig. 2(a). It is evident that for the given density of the obstacles ρ_0 , the time evolution of the normalized number of targets $N_T(t)/N_0^T$ does not depend on the lattice size L . However, for the lattice of fixed size L , time evolution of $N_T(t)/N_0^T$ depends on the initial number of chasers N_0^C and targets N_0^T . We shall return to this point later on in connection with the relationship between the densities of species and dynamics of the model.

In Fig. 2(c) we show the temporal dependence of the number of targets $N_T(t)$ on the lattice of size $L = 128$ obtained for the same conditions as in Fig. 2(a). The shaded strips in Fig. 2(c) indicate an interval of one standard deviation above and below the estimated mean value. In addition, the double logarithmic plots of the same results are also shown in the same panel. In this way, a better insight into the values of the standard deviation during the entire process is enabled. Standard deviations from the average value of $N_T(t)$ are of the order $\pm 1\%$ throughout the whole process of interest. In very late times, when the number of targets disappears, the standard deviation is less than 10%. As it can be seen, the statistical error bars slightly exceed the line thickness.

It must be stressed that all simulations have been performed in the conditions of sufficiently low densities of agents. In this way, we have tried to avoid the effects of the self volume [34,48,49]. In reality, chasers and targets are impenetrable bodies. For example, in an abundant population of prey, the prey species may obstruct each other while trying to escape. Moreover, at sufficiently large densities of targets, target can be temporarily trapped in “cages” formed by their neighbors of the same species. Then the motion of target is restricted by a shell of nearest neighbors, and its movement is influenced by the effect of trapping. However, in our model, agents can be temporarily caged by a dense network of obstacles. In order to make the analysis of the results simpler, it is necessary that these two effects are not present in simulations at the same time. Consequently, all simulations are carried out in the conditions of sufficiently low densities of agents.

In the absence of obstacles, simulations are carried out until all targets have been caught by chasers, i.e. $N_T(t) = 0$. However, in the presence of obstacles, there may be targets that cannot be eliminated by the chasers. Such targets are located within clusters of empty sites (“cages”) in which chasers have not been deposited during the initialization process. The number of inaccessible targets increases with the density of obstacles ρ_0 . Fig. 3 shows two typical snapshot configurations obtained in the case of the binary mixture of obstacles (trimers (A_3) and crosses (C_1)) of density $\rho_0 = 0.30$. The snapshots are taken at the beginning of the process ($t = 1$), and after a long enough time ($t = 300$) when only a few targets ($N_T(300) = 6$) are left in the “cages” formed by obstacles.

Now, we present and discuss the numerical results regarding the time evolution of the number of targets $N_T(t)$ in the absence of obstacles, for several initial densities of chasers ρ_0^C and targets ρ_0^T on the lattice of the fixed size $L = 128$. The initial numbers of species (N_0^C, N_0^T) were chosen as (20, 25), (40, 50), (80, 100), (160, 200), (320, 400), and (640, 800), so that we have the same ratio $N_0^C/N_0^T = 0.8$ in all simulation runs. Temporal evolution of the normalized number of targets $N_T(t)/N_0^T$ for various initial densities $\rho_0^C = N_0^C/L^2$ and $\rho_0^T = N_0^T/L^2$ (provided that $\rho_0^C/\rho_0^T = 0.8$) are presented in Fig. 4. We observe that the decrease of $N_T(t)/N_0^T$ with time gets drastically slower when the initial densities ρ_0^C and ρ_0^T decrease. Analyzing the curves in Fig. 4 we find that the decrease of $N_T(t)/N_0^T$ is slower than exponential in time. In addition, the curves for different values of the initial density of species are very similar in form. In order to provide the best analytical approximation for the temporal behavior of the number of targets $N_T(t)$, we have probed a wide set of phenomenological fitting functions for relaxation processes in many complex disordered systems [50]. The best agreement with our simulation data was obtained by the Kohlrausch–Williams–Watts (KWW) or stretched exponential function. The fitting function we have used is of the form:

$$\frac{N_T(t)}{N_0^T} = 1 + \left(\frac{N_T(\infty)}{N_0^T} - 1 \right) \left(1 - \exp \left[- \left(\frac{t}{\tau} \right)^\beta \right] \right), \quad (1)$$

where β is the parameter measuring the deviation from the single exponential form ($0 < \beta \leq 1$) and τ is the characteristic time. Fits of this stretched exponential form to the simulation data are shown as dashed lines in Fig. 4. Since the asymptotic number of targets $N_T(t) \rightarrow N_T(\infty)$, $t \gg \tau$, in the absence of the obstacles is equal to zero for all initial densities of species, the characteristic time τ can be defined as the time it takes for the simulation curves of $N_T(t)/N_0^T$ to fall to the level of $1/e$, i.e., $N_T(\tau)/N_0^T = 1/e$. In the absence of obstacles, the fitting parameter τ is given in Fig. 5 as a function of the initial density of targets ρ_0^T , for two values of the ratio $N_0^C/N_0^T = 0.8, 1.0$. In numerical simulations with the ratio $N_0^C/N_0^T = 1.0$, the

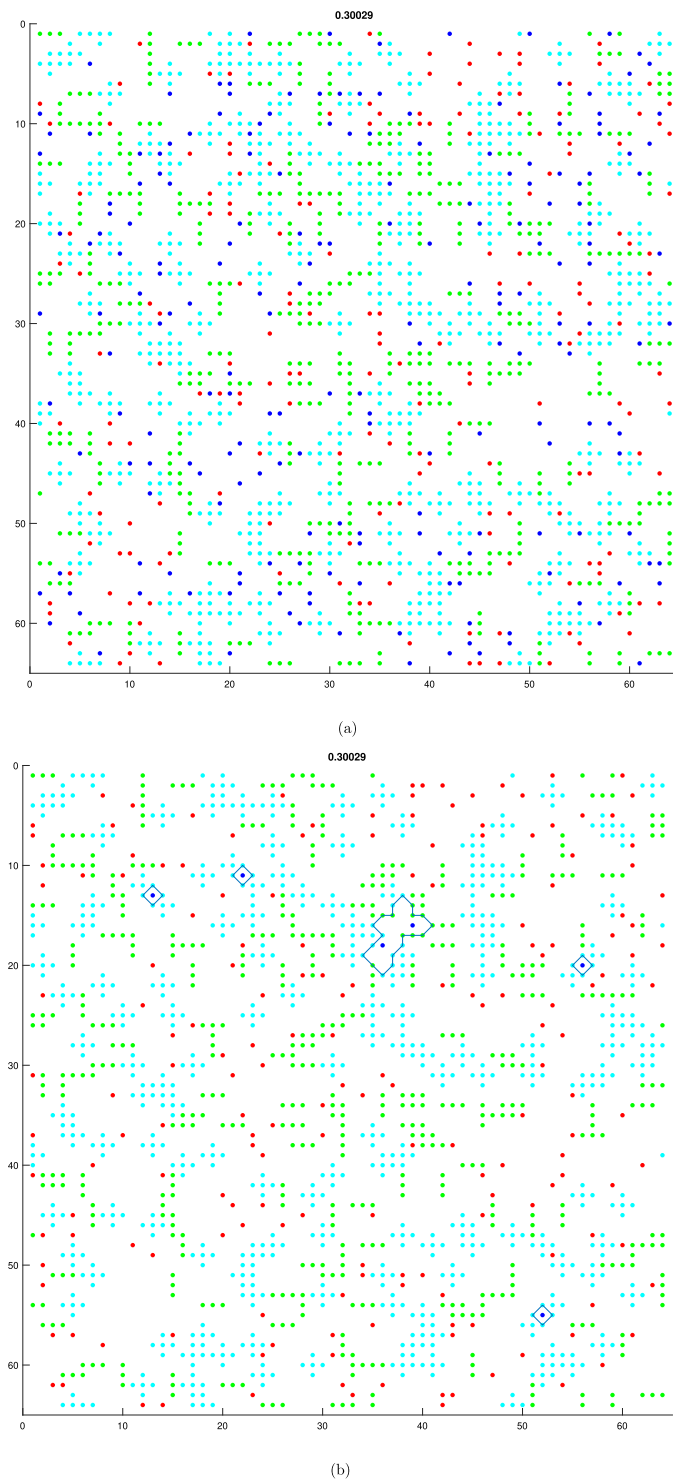


Fig. 3. Typical configurations of chasers (red dots) and targets (blue dots) at lattice of size $L = 64$ in the case of the binary mixture of obstacles (trimers (A_3) and crosses (C_1)) of density $\rho_0 = 0.30$. The snapshots are taken at the beginning of the process ($t = 1$, panel (a)), and after long enough times ($t = 300$, panel (b)) when only six targets are left on the lattice. Five cages with the remaining targets are marked on the panel (b) with thin blue lines. Initial number of chasers/targets is $N_0^C/N_0^T = 180/200$.

initial numbers of species were chosen to be $N_0^C = N_0^T = 25, 50, 100, 200, 400$, and 800 . It is obvious that the parameter τ seems to be a simple power law of the initial density of targets ρ_0^T :

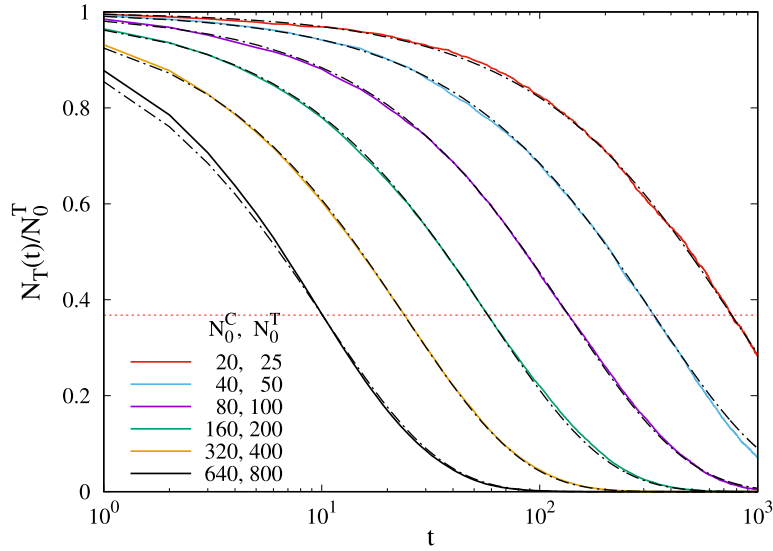


Fig. 4. Temporal evolution of the normalized number of targets $N_T(t)/N_0^T$ obtained in the absence of obstacles on the lattice of the size $L = 128$, and for various initial numbers of species (N_0^C, N_0^T), as indicated in the legend. The dashed curves are the stretched exponential fits of Eq. (1), with the parameter τ given in Fig. 5 and $\beta = 0.802$. Here, the ratio $N_0^C/N_0^T = \rho_0^C/\rho_0^T = 0.8$ is the same in all simulation runs. The horizontal dashed line indicates the $1/e$ value.

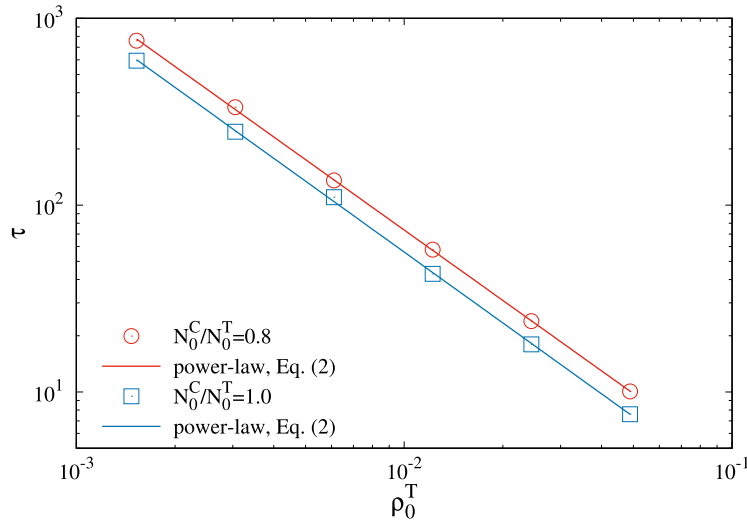


Fig. 5. Fitting parameter τ of the fit (1), as a function of the initial density of targets ρ_0^T in the case of the absence of obstacles, for two values of the initial ratio of chasers to targets $N_0^C/N_0^T = 0.8, 1.0$. The straight lines are the fits using Eq. (2). Dependence of τ on ρ_0^T seems to be well described by the simple power law (2). The values of fitting parameters are $A = 0.230, \gamma = 1.252, \beta = 0.802$ for $N_0^C/N_0^T = 0.8$; for $N_0^C/N_0^T = 1.0$, the fitting parameters are $A = 0.169, \gamma = 1.261, \beta = 0.805$.

$$\tau = A (\rho_0^T)^{-\gamma}. \tag{2}$$

Exponent γ is approximately equal to $\gamma = 1.256 \pm 0.006$ for all examined ratios N_0^C/N_0^T . On the other hand, the stretching exponent β has the values below one, which confirms the nonexponential functional dependence of $N_T(t)/N_0^T$. Furthermore, for the fixed value of ratio N_0^C/N_0^T the exponent β is rather weakly dependent on the initial density of targets ρ_0^T . This provides the collapse of $N_T(t)/N_0^T$ vs. t curves onto a single curve when the time is scaled as t/τ . Fig. 6 shows the time-density superposition of the $N_T(t)/N_0^T$ curves in the case of the ratio $N_0^C/N_0^T = 0.8$, for all initial densities of species investigated. This figure clearly demonstrates the existence of a single universal master function.

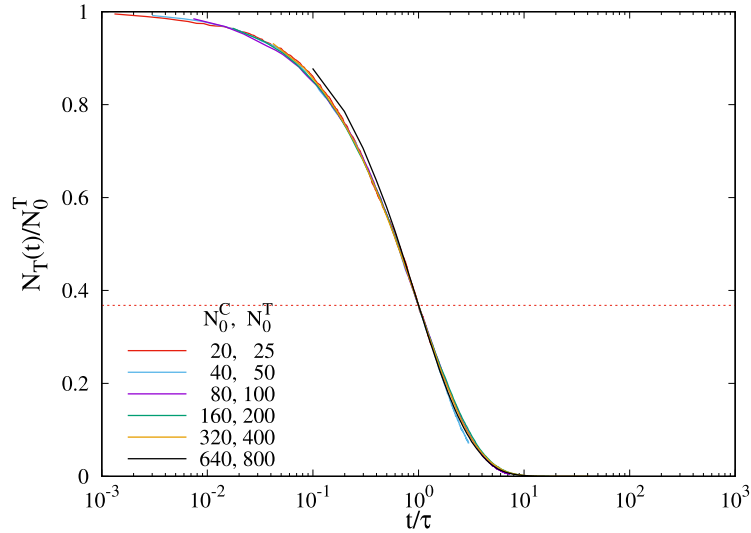


Fig. 6. Normalized number of targets $N_T(t)/N_0^T$ obtained in the absence of obstacles and rescaled to t/τ , for various initial numbers of species (N_0^C, N_0^T), as indicated in the legend. Here, the ratio $N_0^C/N_0^T = \rho_0^C/\rho_0^T = 0.8$ is the same in all simulation runs. The horizontal dashed line indicates the $1/e$ value.

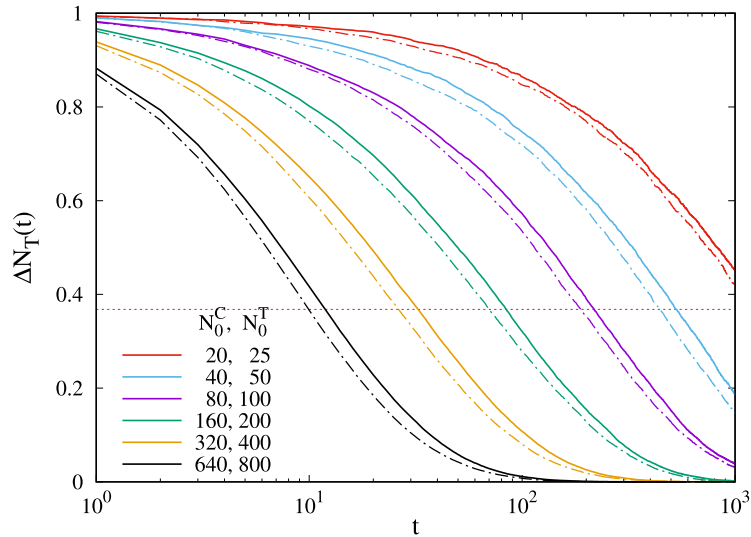


Fig. 7. Temporal evolution of the normalized deviation $\Delta N_T(t)$ (Eq. (3)) of the number of targets $N_T(t)$ obtained in the presence of obstacles (A_1) (solid lines) and (C_1) (dashed lines) on the lattice of size $L = 128$, and for various initial numbers of species (N_0^C, N_0^T), as indicated in the legend. Here, the ratio $N_0^C/N_0^T = \rho_0^C/\rho_0^T = 0.8$ is the same in all simulation runs. The horizontal dashed line indicates the $1/e$ value.

In the following, we analyze the time evolution of the number of targets $N_T(t)$ in the presence of obstacles, for various initial densities of chasers ρ_0^C and targets ρ_0^T on the lattice of the fixed size, $L = 128$. In order to gain a better insight into the effect of obstacles on the capture dynamics, simulations are performed both for point-like obstacles (A_1) and for obstacles of cruciform shape (C_1) covering five lattice sites (see, Tables 1 and 2). Furthermore, the results are obtained for the various values of density of the obstacles, $\rho_0 = 0.15, 0.20, 0.25$, and 0.30 . Let us first focus our attention on the representative results given in Fig. 7 for the case of density $\rho_0 = 0.25$. Fig. 7 shows the time evolution of the normalized deviation $\Delta N_T(t)$ of the number of targets $N_T(t)$ from the asymptotic value $N_T(\infty)$ for various initial densities ρ_0^C and ρ_0^T , provided that $N_0^C/N_0^T = \rho_0^C/\rho_0^T = 0.8$. The quantity $\Delta N_T(t)$ is defined as

$$\Delta N_T(t) = \frac{N_T(t) - N_T(\infty)}{N_0^T - N_T(\infty)}. \quad (3)$$

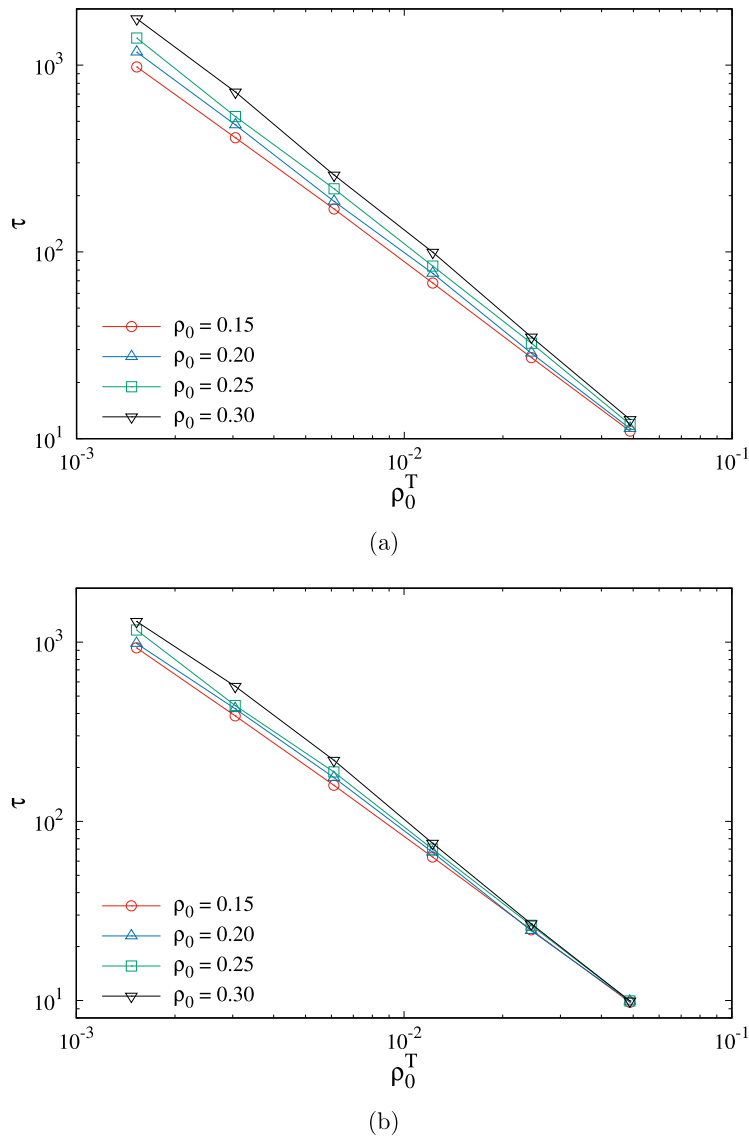


Fig. 8. Fitting parameter τ of the fit (1), as a function of the initial density of targets ρ_0^T in the case of the presence of (a) obstacles (A_1), and (b) obstacles (C_1). The curves in each graph correspond to various values of the density of obstacles $\rho_0 = 0.15, 0.20, 0.25, 0.30$, as indicated in the legend. All the results are for $N_0^C/N_0^T = 0.8$.

As in the case of the absence of obstacles, we observe that the decrease of $N_T(t)/N_0^T$ with time gets slower with the decrease in the initial densities ρ_0^C and ρ_0^T . Comparing the results from Fig. 7 for different obstacles at the same density $\rho_0 = 0.25$, one can see that the number of targets $N_T(t)$ in the case of point-like obstacles (A_1) decreases more slowly in time than for the case of obstacles of cruciform shape (C_1). This change in the capture dynamics is the result of a different structure of empty space that is formed after the deposition of obstacles of different size up to the chosen coverage fraction ρ_0 . Actually, the mesh structure of the open spaces look very different for the adsorbing point-like obstacles (A_1) in comparison with the extended obstacles (C_1) [38,51]. Deposition of the extended obstacles (C_1) is characterized by domains of large islands of unoccupied sites. On the other hand, small obstacles such as monomers (A_1) cover the surface more uniformly, so that the empty space on the lattice is broken into small areas. Such a different free space view is the cause of the enhanced mobility of species in the case of cruciform shapes (C_1) as compared to those in the case of point-like shapes (A_1), resulting in a faster decrease of the number of targets $N_T(t)$ in the former case.

It must be stressed that the stretched-exponential fit (Eq. (1)) also accurately describes the temporal dependence of the number of targets $N_T(t)$ in the presence of obstacles (not shown here). Dependences of the nonlinear fitting parameter τ on the initial density of targets ρ_0^T are shown in Fig. 8 on a double logarithmic scale for various densities of obstacles (A_1) and (C_1), $\rho_0 = 0.15 - 0.30$. For all examined densities and obstacle shapes these plots are nearly straight lines, indicating

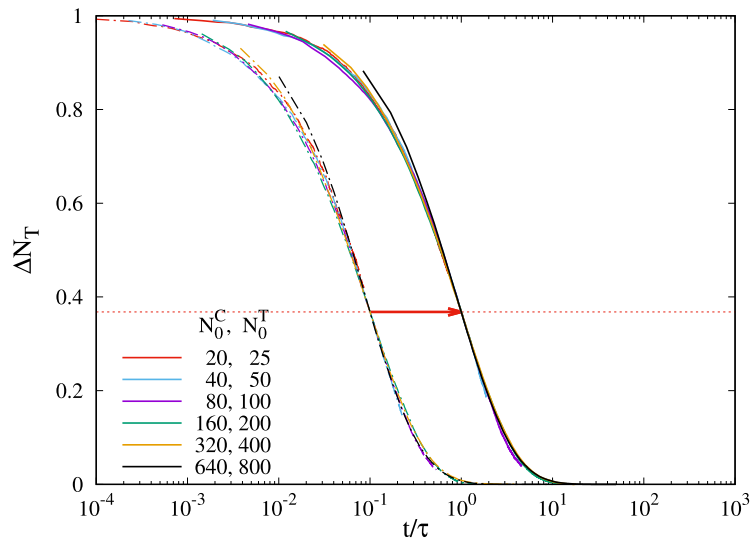


Fig. 9. Normalized deviation $\Delta N_T(t)$ (Eq. (3)) of the number of targets $N_T(t)$ obtained in the presence of obstacles (A_1) (solid lines) and (C_1) (dashed lines) and rescaled to t/τ , for various initial numbers of species (N_0^C, N_0^T), as indicated in the legend. For clarity, the data for obstacle (C_1) are shifted to the left ($t \rightarrow t/10$). Here, the lattice size is $L = 128$, density $\rho_0 = 0.25$, and the initial ratio of chasers to targets $N_0^C/N_0^T = \rho_0^C/\rho_0^T = 0.8$ are the same in all simulation runs. The horizontal dashed line indicates the $1/e$ value.

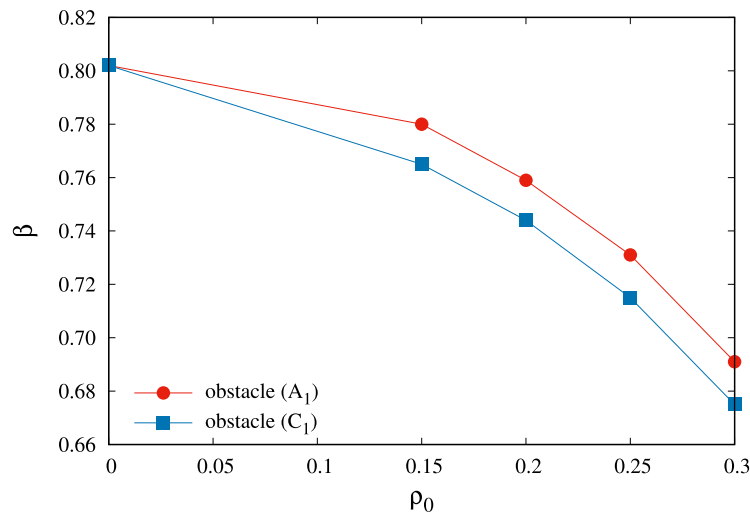


Fig. 10. Parameter β of the fit (1) vs. the density ρ_0 of the obstacles. Circles and squares correspond to obstacles (A_1) and (C_1) in Tables 1 and 2, respectively. Other parameters: $L = 128$, $N_0^C/N_0^T = \rho_0^C/\rho_0^T = 0.8$.

that the fitting parameter τ is a simple power-law of the initial density of targets ρ_0^T (see Eq. (2)). As in the case of the absence of obstacles, we observe that the dynamical behavior of our model is severely slowed down with the decrease of the initial densities ρ_0^C and ρ_0^T . In addition, the characteristic time τ is found to increase with the density of obstacles ρ_0 . As one can see from Figs. 8(a) and 8(b), the increase of τ with ρ_0 is more pronounced for the lower initial densities of targets. Indeed, the efficiency of chasing becomes very high at larger densities of targets and weakly dependent on the presence of obstacles, due to the smaller mean distance between chasers and targets. Then the chasers quickly and efficiently find the neighboring targets, regardless of whether there are obstacles or not. However, for the lower initial concentration of targets the presence of obstacles noticeably slows down the dynamics of the system. We notice, the lower is the concentration of the targets, the longer is the mean distance that a chaser crosses to find a target and catch it. Along the longer path, chaser will interact with a larger number of obstacles. Therefore, obstacles more effectively suppress the chasing for lower densities of targets. Also, at sufficiently low densities of targets, obstruction of chasing is more pronounced at the higher densities of the obstacles.

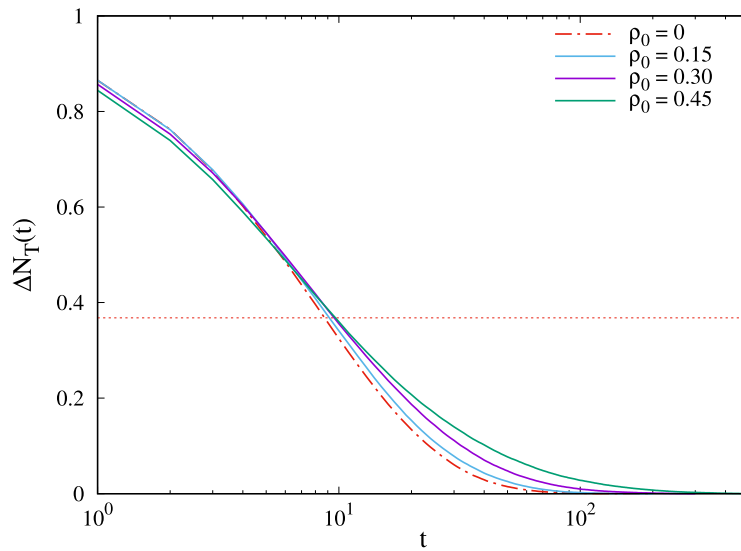


Fig. 11. Temporal evolution of the normalized deviation $\Delta N_T(t)$ (Eq. (3)) of the number of targets $N_T(t)$ obtained in the presence of obstacles (A_3) (solid lines) for various densities ρ_0 , as indicated in the legend. The dashed line represents the temporal behavior of $\Delta N_T(t)$ in the absence of obstacles. Other parameters: $L = 128$, $N_0^C/N_0^T = 720/800 = 0.9$.

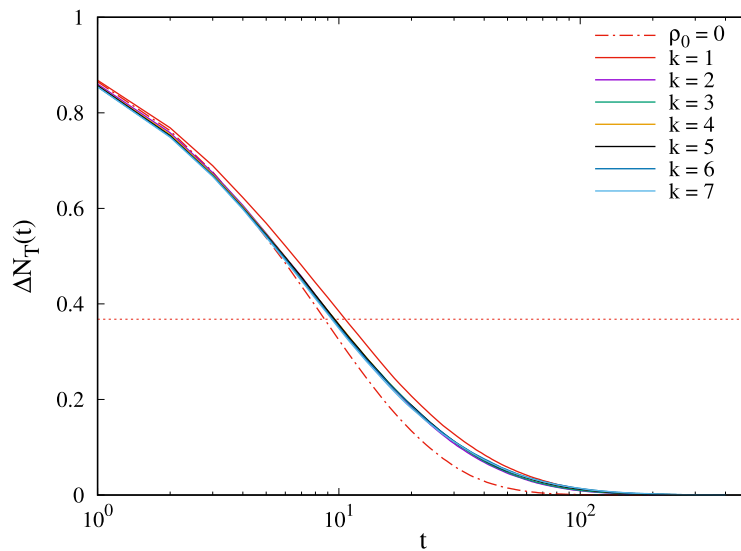


Fig. 12. Temporal evolution of the normalized deviation $\Delta N_T(t)$ (Eq. (3)) of the number of targets $N_T(t)$ obtained in the presence of obstacles (A_1, A_2, \dots, A_7) of density $\rho_0 = 0.30$ (solid lines). The dashed line represents the temporal behavior of $\Delta N_T(t)$ in the absence of obstacles. Other parameters: $L = 128$, $N_0^C/N_0^T = 720/800 = 0.9$.

Fig. 9 illustrates that when the normalized deviations $\Delta N_T(t)$ (see, Eq. (3)) presented in Fig. 7 are plotted as a function of t/τ , the data for the all initial numbers of targets, $N_0^T = 25, 50, 100, 200, 400$ and 800 , collapse onto a single curve. We note that different choices of obstacles give qualitatively similar results. This superposition of ΔN_T vs. t/τ curves is a consequence of the fact that for the fixed values of ratio N_0^C/N_0^T and density of obstacles ρ_0 , the fitting parameter β is rather weakly dependent on the initial density of targets ρ_0^T . However, the stretching exponent β depends on the density ρ_0 of the obstacles. Fig. 10 shows dependence of parameter β on density ρ_0 for the two types of obstacles (A_1) and (C_1). Parameter β measures the rate of the chasing process on the time scale determined by the parameter τ . Consequently, in the late stage of the chasing process the decay rate of the number of targets $N_T(t)$ for the point-like obstacles (A_1) is higher than for the extended obstacles (C_1).

Now we consider in more details the influence of the length ℓ and density ρ_0 of the linear segments that make the obstacles on the temporal behavior of the number of targets $N_T(t)$. The simulations have been performed for linear segments (k -mers) of lengths $\ell = k - 1$, $k = 1, 2, \dots, 7$ (see, Table 1), and for a wide range of obstacle densities,

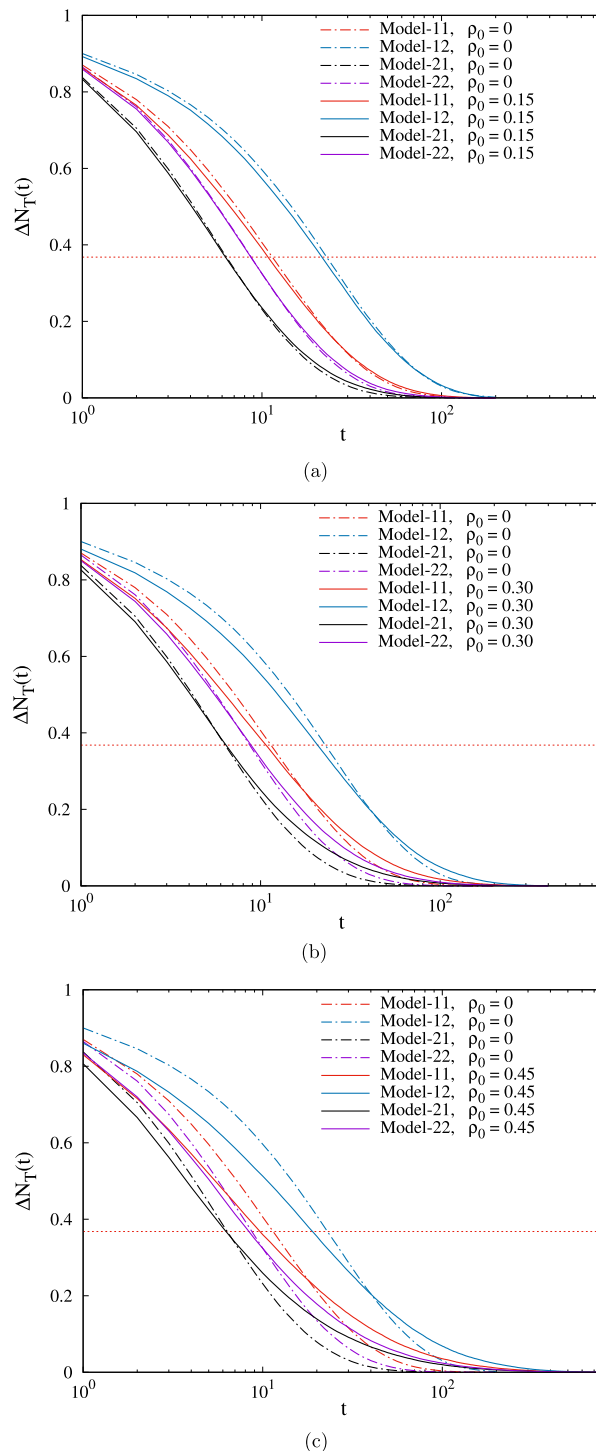


Fig. 13. Temporal behavior of the normalized deviation $\Delta N_T(t)$ (Eq. (3)) for the four models (Model- ij , $i, j = 1, 2$) created by combining the two types of chasers and targets, as shown in Table 3. The solid lines represent the results obtained in the presence of obstacles C_2 (see, Table 2) at densities $\rho_0 = 0.15$ (a), 0.30 (b), 0.45 (c). The dashed lines represent the temporal behavior of $\Delta N_T(t)$ in the absence of obstacles. Other parameters: $L = 128$, $N_0^C/N_0^T = 720/800 = 0.9$.

$\rho_0 = 0 - 0.45$. At first, we present the results of simulations for one representative linear segment, i.e., for the trimer (A_3) at densities $\rho_0 = 0.15, 0.30, 0.45$. The corresponding time dependences of the normalized deviation $\Delta N_T(t)$ (see,

Table 1

Jamming coverages $\rho_j^{(x)}$ for various k -mers (x) of length $\ell^{(x)}$ on a square lattice. The estimated statistical errors are on the last given digits.

(x)	k -mer	$\ell^{(x)}$	$\rho_j^{(x)}$
(A_1)	•	0	1.0
(A_2)	—	1	0.9067
(A_3)	— —	2	0.8465
(A_4)	— — —	3	0.8102
(A_5)	— — — —	4	0.7867
(A_6)	— — — — —	5	0.7699
(A_7)	— — — — — —	6	0.7578

Table 2

Jamming coverages $\rho_j^{(x)}$ for extended shapes (x) of size $s^{(x)}$ on a square lattice. The estimated statistical errors are on the last given digits.


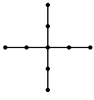
(x)	Shape	$s^{(x)}$	$\rho_j^{(x)}$
(C_1)		2	0.6988
(C_2)		4	0.5691

Table 3

Four models created by combining the two types of chasers and targets. Depending on the sighting range σ , chasers and targets with different chasing and avoidance skills, respectively, can be distinguished.

Model	Chaser	Target
Model-11	Chaser-I ($\sigma = 1$)	Target-I ($\sigma = 1$)
Model-12	Chaser-I ($\sigma = 1$)	Target-II ($\sigma = 2$)
Model-21	Chaser-II ($\sigma = 2$)	Target-I ($\sigma = 1$)
Model-22	Chaser-II ($\sigma = 2$)	Target-II ($\sigma = 2$)

Eq. (3)) for the aforementioned densities ρ_0 are given in Fig. 11 together with the result obtained in the absence of the obstacles. It can be seen that the capture dynamics gets slower, and the evolution of the number of targets $N_T(t)$ toward the asymptotic value $N_T(\infty)$ takes place on much wider time scale when the density of trimers ρ_0 increases. We note that different choices of the linear segments give qualitatively similar results.

In Fig. 12 we compare the temporal evolution of the normalized deviation $\Delta N_T(t)$ (see, Eq. (3)) for the linear segments (k -mers) covering $k = 1, 2, \dots, 7$ lattice sites. Time dependences of $\Delta N_T(t)$ are displayed both for the density $\rho_0 = 0.30$ of obstacles, and for the case of lattice without obstacles. In the presence of k -mers, reduction in the number of targets $N_T(t)$ takes place on the approximately equal time scale for all k -mers. As expected, the decrease of the number of targets $N_T(t)$ with time is significantly faster in the absence of obstacles. It is interesting that $\Delta N_T(t)$ vs. t curves have similar shapes for all finite-size k -mers ($k > 1$). As can be seen, for the point-like obstacles ($k = 1$) the capture dynamics gets slower, especially in the intermediate time regime. There is an important difference between the deposition of point-like and elongated obstacles on a square lattice. Deposition of elongated objects is characterized with domains of parallel objects and large areas of unoccupied sites. Blocking of the lattice area is enhanced with the growth of the obstacle length, making the surface more porous (unoccupied sites can form open and large pores). On the other hand, the point-like objects (monomers) cover the surface more uniformly and efficiently. Lower porosity of the surface is responsible for the reduced mobility of species, and therefore for slower dynamics in the case of the point-like obstacles.

In Section 2 we have introduced the chasers and the targets with different chasing and avoidance skills, respectively. Depending on the sighting range σ , less ($\sigma = 1$) and more ($\sigma = 2$) capable chasers or targets can be distinguished (see, Table 3). It is now useful to explore the relationship between the ability of species and the capture dynamics. In Fig. 13 we compare the temporal evolution of the normalized deviation $\Delta N_T(t)$ (see, Eq. (3)) for all four combinations of previously defined species, as shown in Table 3. The results are given for the obstacle C_2 (see, Table 2) at densities $\rho_0 = 0.15, 0.30, 0.45$, as well as for the lattice without obstacles. By comparing the results for the Model-12 with those for the Model-22 and Model-11, it can be observed that the less capable chasers or the more capable targets cause a significantly slower decrease in the number of targets $N_T(t)$ to the asymptotic value $N_T(\infty)$. On the contrary, by comparing results for the Model-21 with those for the Model-22 and Model-11, it is obvious that the less capable targets or the more capable chasers hasten the dynamics of the chasing process.

As can be seen from Fig. 13 the decrease in the number of targets in the presence of obstacles at sufficiently small times is faster than in the absence of obstacles, and this effect is more pronounced for the larger densities of obstacles.

At the beginning of the process, the density of targets is high, so that the mean distance between them is small. As a consequence, a chaser quickly and efficiently find targets in its own vicinity. At the same time, the obstacles make it difficult for the targets to escape from the nearest chaser. Therefore, the presence of obstacles increases the efficiency of chasers in the initial phase of the evolution of the number of targets.

However, in the late chasing stage inversion occurs, i.e., the presence of obstacles slows down the dynamics of the system (see, Fig. 13). Indeed, the lower is the concentration of the targets, the longer is the time necessary for the chaser to find a target and catch it. Thus, the mean distance that a chaser crosses between two consecutive catches increases over time. Along the longer path, chaser will interact with a larger number of obstacles. Therefore, obstacles more effectively hinder the chasers when the density of the targets becomes small enough.

In models with more capable chasers (Model-22 and Model-21), the presence of obstacles induces larger changes in the dynamics of the system in the late chasing stage than in the initial phase of the process. At the beginning of the process, more capable chasers quickly and efficiently find the neighboring targets, regardless of whether there are obstacles or not. However, less capable chasers interact with a larger number of obstacles between two consecutive catches. Consequently, in the cases of less capable chasers (Model-11 and Model-12), the differences in the dynamics of the system with and without obstacles are pronounced even in the initial phase of the evolution of the number of targets.

4. Summary

We have numerically studied a stochastic lattice model describing a group chase and escape with sight-limited chasers and targets. We take into account the spatial structure of the environment where the species coexist in an explicit way. The environment heterogeneities are built by randomly selecting a fraction of the sites of the square lattice that are considered forbidden for the species. Specifically, the obstacles are represented by non-overlapping lattice shapes that are randomly placed and fixed on the lattice. Our focus in this paper was to investigate the role that density and shape of obstacles plays in the time evolution of the number of targets, $N_T(t)$. Basic mechanisms responsible for the studied phenomenon were investigated and for this reason we ignored the birth/death processes. Such processes will be considered in the future work.

It was shown that the stretched exponential behavior (Eq. (1)) excellently describes the temporal dependence of the number of targets $N_T(t)$ regardless of whether the obstacles are present or not. The characteristic timescale τ was found to decrease with the initial density of targets ρ_0^T according to a power-law (2), $\tau \propto (\rho_0^T)^{-\gamma}$. Furthermore, it was obtained that the characteristic time τ increases with the density of obstacles ρ_0 . This effect was much more pronounced at the lower densities ρ_0 investigated.

We have considered the behavior of the stretched exponent β (Eq. (1)) as a function of the initial density of targets ρ_0^T and the density of obstacles ρ_0 . At the given density of obstacles ρ_0 , the exponent β is weakly dependent on the initial density of targets ρ_0^T , provided the initial ratio of chasers to targets $N_0^C/N_0^T = \rho_0^C/\rho_0^T$ is constant. However, the stretching exponent β , which measures the rate of the chasing process, decreases with the density of the obstacles ρ_0 . At the fixed density ρ_0 , parameter β depends on the shape and size of the obstacles.

The simulations have shown that the time dependences of $\Delta N_T(t)$ (Eq. (3)), at the fixed density ρ_0 , are very similar for all finite-size k -mers ($k > 1$). However, slowing down in the capture dynamics was observed in the case of the point-like obstacles ($k = 1$). Indeed, randomly deposited monomers cover the lattice more uniformly and therefore efficiently reduce the mobility of species.

We have discussed the significance of the sighting range σ of species for governing the capture dynamics in the presence of obstacles. It was shown that the less capable chasers/targets ($\sigma = 1$) or the more capable targets/chasers ($\sigma = 2$) slow-down/hasten the dynamics of the chasing process. It was observed that the decrease in the number of targets in the presence of obstacles at sufficiently small/large times is faster/slower than in the absence of obstacles, and this effect is more pronounced for larger densities of obstacles. In the case of more capable chasers ($\sigma = 2$), the presence of obstacles induces larger changes in the dynamics of the system in the late chasing stage than in the initial phase of the process. In the case of the less capable chasers ($\sigma = 1$), differences in the dynamics of the system with and without obstacles are pronounced in the initial phase of the evolution of the number of targets.

This model can easily be generalized using obstacles of various shapes, describing the system of interest. Features of the chasers and escapees as well as their capabilities can also be modified according to the system of interest. Our simulation can describe in a simple manner some real life systems or tools that are still in development, and becoming more important. Application can be seen even in robotics, especially in unmanned vehicles, designed to avoid obstacles (something that could be developed in new versions of our simulation) and win certain targets that are fixed or in motion, depending on its goal. For instance, one can observe a security robot trying to capture and eliminate malicious evader that is trying to escape. Robot can be instructed not to capture but to follow and monitor the evader (something that could also be developed in other versions of the simulation) and report its behavior. Just visual monitoring can be greatly useful in the home caring situations, for example following elderly people and report if there is an emergency.

Acknowledgments

This work was supported by the Ministry of Education, Science, and Technological Development of the Republic of Serbia under projects ON171017, III45016, and by the European Commission under H2020 project VI-SEEM, Grant No. 675121. Numerical simulations were run on the PARADOX supercomputing facility at the Scientific Computing Laboratory of the Institute of Physics Belgrade.

References

- [1] A. Czirók, E. Ben-Jacob, I. Cohen, T. Vicsek, Formation of complex bacterial colonies via self-generated vortices, *Phys. Rev. E* 54 (1996) 1791–1801.
- [2] A. Czirók, M. Matsushita, T. Vicsek, Theory of periodic swarming of bacteria: Application to proteus mirabilis, *Phys. Rev. E* 63 (2001) 031915.
- [3] A. Sokolov, I.S. Aranson, J.O. Kessler, R.E. Goldstein, Concentration dependence of the collective dynamics of swimming bacteria, *Phys. Rev. Lett.* 98 (2007) 158102.
- [4] D.A. Kessler, H. Levine, Pattern formation in dictyostelium via the dynamics of cooperative biological entities, *Phys. Rev. E* 48 (1993) 4801–4804.
- [5] S. Nagano, Diffusion-assisted aggregation and synchronization in dictyostelium discoideum, *Phys. Rev. Lett.* 80 (1998) 4826–4829.
- [6] W.-J. Rappel, A. Nicol, A. Sarkissian, H. Levine, W.F. Loomis, Self-organized vortex state in two-dimensional dictyostelium dynamics, *Phys. Rev. Lett.* 83 (1999) 1247–1250.
- [7] B. Szabó, G.J. Szöllösi, B. Gönci, Z. Jurányi, D. Selmeczi, T. Vicsek, Phase transition in the collective migration of tissue cells: Experiment and model, *Phys. Rev. E* 74 (2006) 061908.
- [8] P. Friedl, D. Gilmour, Collective cell migration in morphogenesis, regeneration and cancer, *Nat. Rev. Mol. Cell Biol.* 10 (2009) 445457.
- [9] J.M. Belmonte, G.L. Thomas, L.G. Brunnet, R.M.C. de Almeida, H. Chaté, Selfpropelled particle model for cell-sorting phenomena, *Phys. Rev. Lett.* 100 (2008) 248702.
- [10] J. Buhl, D.J.T. Sumpter, I.D. Couzin, J.J. Hale, E. Despland, E.R. Miller, S.J. Simpson, From disorder to order in marching locusts, *Science* 312 (2006) 1402–1406.
- [11] B. Collignon, J.L. Deneubourg, C. Detrain, Leader-based and self-organized communication: Modelling group-mass recruitment in ants, *J. Theoret. Biol.* 313 (2012) 79–86.
- [12] C. Becco, N. Vandewalle, J. Delcourt, P. Poncin, Experimental evidences of a structural and dynamical transition in fish school, *Physica A* 367 (2006) 487–493.
- [13] M. Zheng, Y. Kashimori, O. Hoshino, K. Fujita, T. Kambara, Behavior pattern (innate action) of individuals in fish schools generating efficient collective evasion from predation, *J. Theoret. Biol.* 235 (2005) 153–167.
- [14] I.L. Bajec, F.H. Heppner, Organized flight in birds, *Anim. Behav.* 78 (2009) 777–789.
- [15] C.K. Hemelrijk, H. Hildenbrandt, Some causes of the variable shape of flocks of birds, *PLoS One* 6 (2011) e22479.
- [16] D. Helbing, F. Schweitzer, J. Keltsch, P. Molnár, Active walker model for the formation of human and animal trail systems, *Phys. Rev. E* 56 (1997) 2527–2539.
- [17] D. Helbing, I. Farkas, T. Vicsek, Simulating dynamical features of escape panic, *Nature* 407 (2000) 487–490.
- [18] M. Moussaïd, D. Helbing, G. Theraulaz, How simple rules determine pedestrian behavior and crowd disasters, *Proc. Natl. Acad. Sci.* 108 (2011) 6884–6888.
- [19] J. Kwak, H.-H. Jo, T. Luttinen, I. Kosonen, Collective dynamics of pedestrians interacting with attractions, *Phys. Rev. E* 88 (2013) 062810.
- [20] M. Gutiérrez-Roig, O. Sagarra, A. Oltra, J.R.B. Palmer, F. Bartumeus, A. Díaz-Guilera, J. Perelló, Active and reactive behaviour in human mobility: The influence of attraction points on pedestrians, *Open Sci.* 3 (2016).
- [21] T. Vicsek, A. Zafeiris, Collective motion, *Phys. Rep.* 517 (2012) 71–140.
- [22] P.J. Nahin, *Chases and Escapes: The Mathematics of Pursuit and Evasion*, Princeton University Press, Princeton, NJ, 2007.
- [23] P.L. Krapivsky, S. Redner, Kinetics of a diffusive capture process: Lamb besieged by a pride of lions, *J. Phys. A: Math. Gen.* 29 (1996) 5347.
- [24] G. Oshanin, O. Vasilyev, P.L. Krapivsky, J. Klafter, Survival of an evasive prey, *Proc. Natl. Acad. Sci.* 106 (2009) 13696–13701.
- [25] R. Escobedo, C. Muro, L. Spector, R.P. Coppinger, Group size, individual role differentiation and effectiveness of cooperation in a homogeneous group of hunters, *J. R. Soc. Interface* 11 (2014) <http://dx.doi.org/10.1098/rsif.2014.0204>.
- [26] A. Kamimura, T. Ohira, Group chase and escape, *New J. Phys.* 12 (2010) 053013.
- [27] T. Vicsek, *Nature* 466 (2010) 43.
- [28] R. Nishi, A. Kamimura, K. Nishinari, T. Ohira, Group chase and escape with conversion from targets to chasers, *Physica A* 391 (2012) 337–342.
- [29] P. Romanczuk, I.D. Couzin, L. Schimansky-Geier, Collective motion due to individual escape and pursuit response, *Phys. Rev. Lett.* 102 (2009) 010602.
- [30] V. Zhdankin, J.C. Sprott, Simple predator-prey swarming model, *Phys. Rev. E* 82 (2010) 056209.
- [31] X.-P. Han, T. Zhou, B.-H. Wang, Scaling mobility patterns and collective movements: Deterministic walks in lattices, *Phys. Rev. E* 83 (2011) 056108.
- [32] T.H. Chung, G.A. Hollinger, V. Isler, Search and pursuit-evasion in mobile robotics, *Auton. Robots* 31 (2011) 299.
- [33] T. Iwama, M. Sato, Group chase and escape with some fast chasers, *Phys. Rev. E* 86 (2012) 067102.
- [34] S. Yang, S. Jiang, L. Jiang, G. Li, Z. Han, Aggregation increases prey survival time in group chase and escape, *New J. Phys.* 16 (2014) 083006.
- [35] Y. Chen, T. Kolokolnikov, A minimal model of predators-warm interactions, *J. R. Soc. Interface* 11 (2014) <http://dx.doi.org/10.1098/rsif.2013.1208>.
- [36] A. Kamimura, S. Matsumoto, T. Nogawa, N. Ito, T. Ohira, Stochastic resonance with group chase and escape, in: 2011 21st International Conference on Noise and Fluctuations, 2011, pp. 200–203.
- [37] J.W. Evans, Random and cooperative sequential adsorption, *Rev. Modern Phys.* 65 (1993) 1281–1329.
- [38] Lj Budinski-Petković, I. Lončarević, D. Dujak, A. Karač, J.R. Šćepanović, Z.M. Jakšić, S.B. Vrhovac, Particle morphology effects in random sequential adsorption, *Phys. Rev. E* 95 (2017) 022114.
- [39] N. Boccara, O. Roblin, M. Roger, Automata network predator-prey model with pursuit and evasion, *Phys. Rev. E* 50 (1994) 4531–4541.
- [40] A.F. Rozenfeld, E.V. Albano, Critical and oscillatory behavior of a system of smart preys and predators, *Phys. Rev. E* 63 (2001) 061907.
- [41] H. Chaté, F. Ginelli, G. Grégoire, F. Raynaud, Collective motion of self-propelled particles interacting without cohesion, *Phys. Rev. E* 77 (2008) 046113.
- [42] L. Angelani, Collective predation and escape strategies, *Phys. Rev. Lett.* 109 (2012) 118104.
- [43] T. Vicsek, A. Czirók, E. Ben-Jacob, I. Cohen, O. Shochet, Novel type of phase transition in a system of self-driven particles, *Phys. Rev. Lett.* 75 (1995) 1226–1229.
- [44] H. Wang, W. Han, J. Yang, Group chase and escape with sight-limited chasers, *Physica A* 465 (2017) 34–39.
- [45] J. Travis, Do wandering albatrosses care about math? *Science* 318 (2007) 742–743.
- [46] N. Vandewalle, S. Galam, M. Kramer, A new universality for random sequential deposition of needles, *Eur. Phys. J. B* 14 (2000) 407–410.
- [47] V. Cornette, A.J. Ramirez-Pastor, F. Nieto, Percolation of polyatomic species on a square lattice, *Eur. Phys. J. B* 36 (2003) 391–399.
- [48] M. Bruna, S.J. Chapman, Diffusion of multiple species with excluded-volume effects, *J. Chem. Phys.* 137 (2012) 204116.
- [49] M. Schwarzl, A. Godec, G. Oshanin, R. Metzler, A single predator charging a herd of prey: Effects of self volume and predator-prey decision-making, *J. Phys. A* 49 (2016) 225601.
- [50] R. Hilfer, Analytical representations for relaxation functions of glasses, *J. Non-Cryst. Solids* 305 (2002) 122–126.
- [51] Lj. Budinski-Petković, I. Lončarević, Z.M. Jakšić, S.B. Vrhovac, N.M. Švrakić, Simulation study of anisotropic random sequential adsorption of extended objects on a triangular lattice, *Phys. Rev. E* 84 (2011) 051601.



УНИВЕРЗИТЕТ У БЕОГРАДУ - ФИЗИЧКИ ФАКУЛТЕТ
UNIVERSITY OF BELGRADE, FACULTY OF PHYSICS

Студентски трг 12, 11000 Београд, Факс 44, Тел: 011-7158-151, Факс: 011-3282-619
Studentski trg 12, 11000 Belgrade, Serbia, POB 44, Tel: +381-11-7158-151, Fax: +381-11-3282-619
www.ff.bg.ac.rs e-mail: dekanat@ff.bg.ac.rs

УНИВЕРЗИТЕТ У БЕОГРАДУ
ФИЗИЧКИ ФАКУЛТЕТ
Бр. 370/11
23. 6. 2014. г.
БЕОГРАД, СТУДЕНТСКИ ТРГ 12-18
П. Б. Х. 44

На основу члана 161 Закона о општем управном поступку («Службени Лист СРЈ» број 33/97 и 31/01), и члана 120 Статута Универзитета у Београду - Физичког факултета, по захтеву ЈУЛИЈЕ ШЋЕПАНОВИЋ, дипломираног астрофизичара, издаје се следеће

У В Е Р Е Њ Е

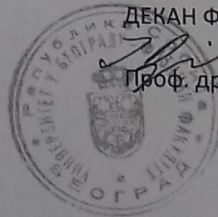
ЈУЛИЈА ШЋЕПАНОВИЋ, дипломирани астрофизичар, дана 23. јуна 2014. године, одбранила је докторску дисертацију под називом

„РЕЛАКСАЦИОНА СВОЈСТВА МОДЕЛА СУБДИФУЗИВНОГ ГАСА НА ТРОУГАОНОЈ РЕШЕТКИ“

пред Комисијом Универзитета у Београду - Физичког факултета, и тиме испунила све услове за промоцију у ДОКТОРА НАУКА – ФИЗИЧКЕ НАУКЕ.

Уверење се издаје на лични захтев, а служи ради регулисања права из радног односа и важи до промоције, односно добијања докторске дипломе.

Уверење је ослобођено плаћања таксе.



ДЕКАН ФИЗИЧКОГ ФАКУЛТЕТА

Проф. др Јаблан Дојчиловић

Република Србија
МИНИСТАРСТВО ПРОСВЕТЕ,
НАУКЕ И ТЕХНОЛОШКОГ РАЗВОЈА
Комисија за стицање научних звања

Број:660-01-00042/545
25.03.2015. године
Београд

17-04-2015	
Пр	рилог
Рад	495/17

На основу члана 22. става 2. члана 70. став 5. Закона о научноистраживачкој делатности ("Службени гласник Републике Србије", број 110/05 и 50/06 – исправка и 18/10), члана 2. става 1. и 2. тачке 1 – 4.(прилози) и члана 38. Правилника о поступку и начину вредновања и квантитативном исказивању научноистраживачких резултата истраживача ("Службени гласник Републике Србије", број 38/08) и захтева који је поднео

Инстџиџуџ за физику у Беоџраду

Комисија за стицање научних звања на седници одржаној 25.03.2015. године, донела је

**ОДЛУКУ
О СТИЦАЊУ НАУЧНОГ ЗВАЊА**

Др Јулија Шћеџановић

стиче научно звање
Научни сарадник

у области природно-математичких наука - физика

О Б Р А З Л О Ж Е Њ Е

Инстџиџуџ за физику у Беоџраду

утврдио је предлог број 1435/1 од 28.10.2014. године на седници научног већа Института и поднео захтев Комисији за стицање научних звања број 1455/1 од 12.11.2014. године за доношење одлуке о испуњености услова за стицање научног звања **Научни сарадник**.

Комисија за стицање научних звања је по претходно прибављеном позитивном мишљењу Матичног научног одбора за физику на седници одржаној 25.03.2015. године разматрала захтев и утврдила да именована испуњава услове из члана 70. став 5. Закона о научноистраживачкој делатности ("Службени гласник Републике Србије", број 110/05 и 50/06 – исправка и 18/10), члана 2. става 1. и 2. тачке 1 – 4.(прилози) и члана 38. Правилника о поступку и начину вредновања и квантитативном исказивању научноистраживачких резултата истраживача ("Службени гласник Републике Србије", број 38/08) за стицање научног звања **Научни сарадник**, па је одлучила као у изреци ове одлуке.

Доношењем ове одлуке именована стиче сва права која јој на основу ње по закону припадају.

Одлуку доставити подносиоцу захтева, именованој и архиви Министарства просвете, науке и технолошког развоја у Београду.

ПРЕДСЕДНИК КОМИСИЈЕ

Др Станислава Стошић-Грујичић,
научни саветник

С. Стошић-Грујичић

ДРЖАВНИ СЕКРЕТАР

Др Александар Белић

Александар Белић